

1 LEVERAGING MULTI-MESSENGER ASTROPHYSICS FOR DARK MATTER SEARCHES

By

Daniel Nicholas Salazar-Gallegos

A DISSERTATION

Submitted to
Michigan State University
in partial fulfillment of the requirements
for the degree of

Physics—Doctor of Philosophy
Computational Mathematics in Science and Engineering—Dual Major

Today

ABSTRACT

3 I did Dark Matter with HAWC and IceCube. I also used Graph Neural Networks

⁴ Copyright by

⁵ DANIEL NICHOLAS SALAZAR-GALLEGOS

⁶ Today

ACKNOWLEDGMENTS

8 I love my friends. Thanks to everyone that helped me figure this out. Amazing thanks to the people
9 at LANL who supported me. Eames, etc Dinner Parties Jenny and her child Kaydince Kirsten, Pat,
10 Andrea Family. You're so far but so critical to my formation. Unconditional love. Roommate

TABLE OF CONTENTS

12	LIST OF TABLES	vii
13	LIST OF FIGURES	viii
14	LIST OF ABBREVIATIONS	xiv
15	CHAPTER 1 INTRODUCTION	1
16	CHAPTER 2 DARK MATTER IN THE COSMOS	2
17	2.1 Introduction	2
18	2.2 Dark Matter Basics	3
19	2.3 Evidence for Dark Matter	4
20	2.4 Searching for Dark Matter: Particle DM	11
21	2.5 Sources for Indirect Dark Matter Searches	16
22	2.6 Multi-Messenger Dark Matter	18
23	CHAPTER 3 MULTIMESSENGER ASTROPHYSICS: DETECTING HIGH EN-	
24	ERGY NEUTRAL MESSENGERS	21
25	3.1 Introduction	21
26	3.2 Charged Particles in a Medium	21
27	3.3 Photons (γ)	22
28	3.4 Neutrinos (ν)	22
29	3.5 Opportunities to Combine for Dark Matter	22
30	CHAPTER 4 HIGH ALTITUDE WATER CHERENKOV (HAWC) OBSERVATORY .	24
31	4.1 The Detector	24
32	4.2 Events Reconstruction and Data Acquisition	24
33	4.3 Remote Monitoring	24
34	CHAPTER 5 ICECUBE NEUTRINO OBSERVATORY	25
35	5.1 The Detector	25
36	5.2 Events Reconstruction and Data Acquisition	25
37	5.3 Northern Test Site	25
38	CHAPTER 6 COMPUTATIONAL TECHNIQUES IN PARTICLE ASTROPHYSICS .	26
39	6.1 Neural Networks for Gamma/Hadron Separation	26
40	6.2 Parallel Computing for Dark Matter Analyses	26
41	CHAPTER 7 GLORY DUCK: MULTI-WAVELENGTH SEARCH FOR DARK MATT-	
42	TER ANNIHILATION TOWARDS DWARF SPHEROIDAL GALAX-	
43	IES	27
44	7.1 Introduction	27
45	7.2 Dataset and Background	29
46	7.3 Analysis	30

47	7.4	Likelihood Methods	35
48	7.5	HAWC Results	41
49	7.6	Glory Duck Combined Results	44
50	7.7	HAWC Systematics	49
51	7.8	<i>J</i> -factor distributions	50
52	7.9	Discussion and Conclusions	56
53	CHAPTER 8	MULTITHREADING HAWC ANALYSES FOR DARK MATTER SEARCHES	60
55	8.1	Introduction	60
56	8.2	Dataset and Background	60
57	8.3	Analysis	61
58	CHAPTER 9	HEAVY DARK MATTER ANNIHILATION SEARCH WITH ICE- CUBE'S NORTH SKY TRACK DATA	67
60	CHAPTER 10	NU DUCK	68
61	APPENDIX A	MULTI-EXPERIMENT SUPPLEMENTARY FIGURES	69
62	APPENDIX B	MULTITHREADING SUPPLEMENTARY FIGURES	70
63	BIBLIOGRAPHY		71

LIST OF TABLES

<p>65 Table 7.1 Summary of the relevant properties of the dSphs used in the present work. 66 Column 1 lists the dSphs. Columns 2 and 3 present their heliocentric distance 67 and galactic coordinates, respectively. Columns 4 and 5 report the J-factors of 68 each source given from the \mathcal{GS} and \mathcal{B} independent studies and their estimated 69 $\pm 1\sigma$ uncertainties. The values $\log_{10} J$ (\mathcal{GS} set) [45] correspond to the mean 70 J-factor values for a source extension truncated at the outermost observed star. 71 The values $\log_{10} J$ (\mathcal{B} set) [47] are provided for a source extension at the tidal 72 radius of each dSph. Bolded sources are within HAWC's field of view and 73 provided to the Glory Duck analysis.</p>	<p style="margin-top: 100px;">35</p>
<p>74 Table 7.2 Summary of dSph observations by each experiment used in this work. A 75 ‘-’ indicates the experiment did not observe the dSph for this study. For 76 Fermi-LAT, the exposure at 1 GeV is given. For HAWC, $\Delta\theta$ is the absolute 77 difference between the source declination and HAWC latitude. HAWC is more 78 sensitive to sources with smaller $\Delta\theta$. For IACTs, we show the zenith angle 79 range, the total exposure, the energy range, the angular radius θ of the signal or 80 ON region, the ratio of exposures between the background-control (OFF) and 81 signal (ON) regions (τ), and the significance of gamma-ray excess in standard 82 deviations, σ.</p>	<p style="margin-top: 100px;">36</p>
<p>83 Table 8.1 Summary of the relevant properties of the dSphs used in the present work. 84 Column 1 lists the dSphs. Columns 2 and 3 present their heliocentric distance 85 and galactic coordinates, respectively. Columns 4 and 5 report the J-factors of 86 each source given from the \mathcal{GS} and \mathcal{B} independent studies and their estimated 87 $\pm 1\sigma$ uncertainties. The values $\log_{10} J$ (\mathcal{GS} set) [45] correspond to the mean 88 J-factor values for a source extension truncated at the outermost observed star. 89 The values $\log_{10} J$ (\mathcal{B} set) [47] are provided for a source extension at the tidal 90 radius of each dSph.</p>	<p style="margin-top: 100px;">64</p>
<p>91 Proof I know how to include</p>	

LIST OF FIGURES

93	Figure 2.1	Rotation curve fit to NGC 6503 from [7]. Dashed line is the contribution 94 from visible matter. Dotted curves are from gas. Dash-dot curves are from 95 dark matter (DM). Solid line is the composite contribution from all matter 96 and DM sources. Data are indicated with bold dots with error bars. Data 97 agree strongly with a matter + DM composite prediction.	5
98	Figure 2.2	Light from distant galaxy is bent in unique ways depending on the distribution 99 of mass between the galaxy and Earth. Yellow dashed lines indicate where 100 the light would have gone if the matter were not present [8].	7
101	Figure 2.3	(left) Optical image of galactic cluster 1E0657-558. (right) X-ray image of the 102 cluster with redder meaning hotter and higher baryon density. (both) Green 103 contours are reconstruction of gravity contours from weak lensing. White 104 rings are the best fit mass maxima at 68.3%, 95.5%, and 99.7% confidence. 105 The matter maxima of the clusters are clearly separated from x-ray maxima. [9]	8
106	Figure 2.4	Plank CMB sky. Sky map features small variations in temperature in primor- 107 dial light. These anisotropies are used to make inferences about the universe's 108 energy budget and developmental history. [10]	9
109	Figure 2.5	Observed Cosmic Microwave Background power spectrum as a function of 110 multipole moment from Plank [10]. Blue line is best fit model from Λ CDM. 111 Red points and lines are data and error, respectively.	10
112	Figure 2.6	Predicted power spectra of CMB for different $\Omega_m h^2$ values for fixed baryon 113 density from [11]. (left) Low $\Omega_m h^2$ increases the prominence of first and 114 second peaks. (middle) $\Omega_m h^2$ is most similar to the observed power spectrum. 115 The second and third peaks are similar in height. (right) $\Omega_m h^2$ is large which 116 suppresses the first peak and raises the prominence of the third peak.	10
117	Figure 2.7	The Standard Model (SM) of particle physics. Figure taken from http://www.quantumdiaries.org/2014/03/14/the-standard-model-a-beautiful-but-flawed-theory/	12
120	Figure 2.8	Simplified Feynman diagram demonstrating with different ways DM can 121 interact with SM particles. The 'X's refer to the DM particles whereas the 122 SM refer to fundamental particles in the SM. The large circle in the center 123 indicates the vertex of interaction and is purposely left vague. The colored 124 arrows refer to different directions of time as well as their respective labels. 125 The arrows indicate the initial and final state of the DM -SM interaction in time.	13

126	Figure 2.9 A single jet event in ATLAS detector from 2017 [16]. Jet momentum was 127 observed to be 1.9 TeV. Missing transverse momentum was observed to be 128 1.9 TeV compared to the initial transverse momentum of the event was 0. 129 Implied MET is traced by a red dashed line in event display.	14
130	Figure 2.10 More detailed pseudo-Feynman diagram of particle cascade from dark matter 131 annihilation into 2 quarks. The quarks hadronize and down to stable particles 132 like γ or the anti-proton (p^-). Diagram pulled from ICRC 2021 presentation 133 on DM annihilation search [17].	15
134	Figure 2.11 Dark Matter (DM) decay spectrum for $b\bar{b}$ initial state and γ final state. Redder 135 spectra are for larger DM masses. Bluer spectra are light DM masses. x is a 136 unitless factor defined as the ratio of the mass of DM, m_χ , and the final state 137 particle energy E_γ . Figure from [19].	17
138	Figure 2.12 Different dark matter density profiles compared. Some models produce ex- 139 ceptionally large densities at small r [20].	18
140	Figure 2.13 The Milky Way Galaxy in photons (γ) and neutrinos (ν) [22]. The Galactic 141 center is at $l=0^\circ$ and is the brightest region in all panels. (top) An Optical 142 color image of the Milky Way galaxy seen from Earth. Clouds of gas and dust 143 obscure some light from stars. (2nd down) Integrated flux of γ -rays observed 144 by the Fermi-LAT telescope [23]. (middle) Expected neutrino emission 145 that corresponds with Fermi-LAT observations. (2nd up) Expected neutrino 146 emission profile after considering detector systematics of IceCube. (bottom) 147 Observed neutrino emission from region of the galactic plane. Substantial 148 neutrino emission was detected.	19
149	Figure 2.14 Dark Matter annihilation spectra for different final state particle and standard 150 model annihilation channels [24]. Photons (red), e^\pm (green), \bar{p} (blue), ν (black).	20
151	Figure 3.1 TODO: Show a nuclear reactor with cherenkov radiation[NEEDS A SOURCE][FACT 152 CHECK THIS]	22
153	Figure 3.2 TODO: absorption spectrum of liquid and solid water[NEEDS A SOURCE][FACT 154 CHECK THIS]	23

155	Figure 7.1 Sensitivities of five gamma-ray experiments compared to percentages of the 156 Crab nebula's emission and dark matter annihilation. Solid lines present 157 estimated sensitivities to power law spectra [FACT CHECK THIS]for each 158 experiment. Green lines are Fermi-LAT sensitivities where lighter green is 159 the sensitivity to the galactic center and dark green is its sensitivity to higher 160 declinations. Orange, red, and purple solid lines represent the MAGIC, HESS, 161 and VERITAS 50 hour sensitivities respectively. The maroon and brown lines 162 are the HAWC 1 year and 5 year sensitivities. Across four decades of gamma- 163 ray energy, these experiments have similar sensitivities on the order 10^{-12} 164 erg cm $^{-2}$ s $^{-1}$. The dotted lines are estimated dark matter fluxes assuming 165 $m_\chi = 5$ TeV DM annihilating to bottom quarks (red), tau leptons (blue), 166 and W bosons (green). Faded gray lines outline percentage flux of the Crab 167 nebula. Figure is an augmented version of [25]	28
168	Figure 7.2 Effect of Electroweak (EW) corrections on expected DM annihilation spec- 169 trum for $\chi\chi \rightarrow W^-W^+$. Solid lines are spectral models that consider EW 170 corrections. Dash-dot lines are spectral models without EW corrections. Red 171 lines are models for $M_\chi = 1$ TeV. Blue lines represent models for $M_\chi = 100$ 172 TeV. All models are sourced from the PPPC4DMID [44].	32
173	Figure 7.3 $\frac{dJ}{d\Omega}$ maps for Segue1 (top) and Coma Berenices (bottom). Origin is centered 174 on the specific dwarf spheroidal galaxies (dSph). X and Y axes are the 175 angular separation from the center of the dwarf. Plots of the remaining 11 176 dSph HAWC studied are linked in Fig. A.1.	34
177	Figure 7.4 Illustration of the combination technique showing a comparison between 178 $-2 \ln \lambda$ provided by four instruments (colored lines) from the observation 179 of the same dSph without any J nuisance and their sum, <i>i.e.</i> the resulting 180 combined likelihood (thin black line). According to the test statistics of 181 Equation (7.6), the intersection of the likelihood profiles with the line $-2 \ln \lambda$ 182 = 2.71 indicates the 95% C.L. upper limit on $\langle \sigma v \rangle$. The combined likelihood 183 (thin black line) shows a smaller value of upper limit on $\langle \sigma v \rangle$ than those 184 derived by individual instruments. We also show how the uncertainties on 185 the J factor effects the combined likelihood and degrade the upper limit on 186 $\langle \sigma v \rangle$ (thick black line). All likelihood profiles are normalized so that the global 187 minimum $\widehat{\langle \sigma v \rangle}$ is 0. We note that each profile depends on the observational 188 conditions in which a target object was observed. The sensitivity of a given 189 instrument can be degraded and the upper limits less constraining if the 190 observations are performed in non-optimal conditions such as a high zenith 191 angle or a short exposure time.	39
192	Figure 7.5 HAWC upper limits at 95% confidence level on $\langle \sigma v \rangle$ versus DM mass for 193 seven annihilation channels, using the set of J -factors from Ref. [53] The 194 solid line represents the observed combined limit. Dashed lines represent 195 limits from individual dSphs.	42

196	Figure 7.6 HAWC TS values for best fit $\langle\sigma v\rangle$ versus m_χ for seven SM annihilation channels with J factors from \mathcal{GS} . The solid black line shows the combined best fit TS values. The colored, dashed lines are the TS values for each of the 13 sources HAWC studied.	43
200	Figure 7.7 HAWC Brazil bands at 95% confidence level on $\langle\sigma v\rangle$ versus DM mass for seven annihilation channels with J -factors from \mathcal{GS} [53]. The solid line represents the combined limit from 13 dSphs. The dashed line is the expected limit. The green band is the 68% containment. The yellow band is the 95% containment.	44
205	Figure 7.8 Upper limits at 95% confidence level on $\langle\sigma v\rangle$ in function of the DM mass for eight annihilation channels, using the set of J factors from Ref. [53] (\mathcal{GS} set in Table 7.1). The black solid line represents the observed combined limit, the black dashed line is the median of the null hypothesis corresponding to the expected limit, while the green and yellow bands show the 68% and 95% containment bands. Combined upper limits for each individual detector are also indicated as solid, colored lines. The value of the thermal relic cross-section in function of the DM mass is given as the red dotted-dashed line [54].	45
214	Figure 7.9 Same as Fig. 7.8, using the set of J factors from Ref. [47, 55] (\mathcal{B} set in Table 7.1).	46
215	Figure 7.10 Comparisons of the combined limits at 95% confidence level for each of the eight annihilation channels when using the J factors from Ref. [53] (\mathcal{GS} set in Table 7.1), plain lines, and the J factor from Ref. [47, 55] (\mathcal{B} set in Table 7.1), dashed lines. The cross-section given by the thermal relic is also indicated [54].	48
219	Figure 7.11 Comparisons of the combined limits at 95% confidence level for a point source analysis and extended source using [53] \mathcal{GS} J-factor distributions and PPPC [44] annihilation spectra. Shown are the limits for Segue1 which will have the most significant impact on the combined limit. 6 of the 7 DM annihilation channels are shown. Solid lines are extended source studies. Dashed lines are point source studies. Overall, the extended source analysis improves the limit by a factor of 2.	50
226	Figure 7.12 Same as Fig. 7.11 on Coma Berenices. This dSph also contributes significantly to the limit. The limits are identical in this case.	51
228	Figure 7.13 Comparison of combined limits when correcting for HAWC's pointing systematic. All DM annihilation channels are shown. The solid black line is the ratio between published limit to the declination corrected limit. The blue solid line or "Combined_og" represented the limits computed for Glory Duck. The solid orange line or "Combined_ad" represented the limits computed after correcting for the pointing systematic.	52

234	Figure 7.14 Differential map of dJ/Ω from model built in Section 7.8.1 and profiles provided directly from authors. (Top) Differential from Segue1. (bottom) Differential from Coma Berenices. Note that their scales are not the same. Segue1 shows the deepest discrepancies which is congruent with its large uncertainties. Both models show anuli where unique models become apparent.	53
239	Figure 7.15 HAWC limits for Coma Berenices (top) and Segue1 (bottom) for two different map sets. Blue lines are limits calculated on maps with poor model representation. Orange lines are limits calculated on spatial profiles provided by the authors of [45]. Black line is the ratio of the poor spatial model limits to the corrected spatial models. The left y-axis measures $\langle\sigma v\rangle$ for the blue and orange lines. The right y-axis measures the ratio and is unitless.	54
245	Figure 7.16 Comparisons between the J -factors versus the angular radius for the computation of J factors from Ref. [53] (\mathcal{GS} set in Table 7.1) in blue and for the computation from Ref. [47, 55] (\mathcal{B} set in Tab. 7.1) in orange. The solid lines represent the central value of the J -factors while the shaded regions correspond to the 1σ standard deviation.	57
250	Figure 7.17 Comparisons between the J -factors versus the angular radius for the computation of J factors from Ref. [53] (\mathcal{GS} set in Tab. 7.1) in blue and for the computation from Ref. [47, 55] (\mathcal{B} set in Tab. 7.1) in orange. The solid lines represent the central value of the J -factors while the shaded regions correspond to the 1σ standard deviation.	58
255	Figure 8.1 Difference between spectral hypotheses from PPPC [44] and HDM [64]. Shown is the expected DM annihilation spectrum for $\chi\chi \rightarrow W^-W^+$. Solid lines are spectral models with EW corrections from the PPPC. Dash-dot lines are spectral models from HDM. Red lines are models for $M_\chi = 1$ TeV. Blue lines represent models for $M_\chi = 100$ TeV.	63
260	Figure 8.2 Photon spectra for $\chi\chi \rightarrow \gamma\gamma$ (left) and $\chi\chi \rightarrow ZZ$ (right) after gaussian convolution of line features. Both spectra have δ -features at photon energies equal to the DM mass. Bluer lines are annihilation spectra with lower DM mass. Redder lines are spectra from larger DM mass. All Spectral models are sourced from the Heavy Dark Matter models [64].	64
265	Figure 8.3 $\frac{dJ}{d\Omega}$ maps for Coma Berenices, Draco, Segue1, and Sextans. Columns are divided for the $\pm 1\sigma$ uncertainties in $dJ/d\Omega$ around the median value from \mathcal{LS} [65]. Origin is centered on the specific dwarf spheroidal galaxies (dSph). θ and ϕ axes are the angular separation from the center of the dwarf. Axes are drawn roughly according to the energy sensitivity of HAWC.	65
270	Figure A.1 Sister figure to Figure 7.3. Sources in the first row from left to right: Bootes I, Canes Venatici I, II. In second row: Draco, Hercules, Leo I. In the first row: Leo II, Leo IV, Sextans. In the final row: Ursa Major I, Ursa Major II.	69

LIST OF ABBREVIATIONS

- 278 **MSU** Michigan State University
279 **LANL** Los Alamos National Laboratory
280 **DM** Dark Matter
281 **SM** Standard Model
282 **HAWC** High Altitude Water Cherenkov Observatory

283

CHAPTER 1

INTRODUCTION

284 Is the text not rendering right? Ah ok it knows im basically drafting the doc still

CHAPTER 2

285

DARK MATTER IN THE COSMOS

286 **2.1 Introduction**

287 The dark matter problem can be summarized in part by the following thought experiment.

288 Let us say you are the teacher for an elementary school classroom. You take them on a field
289 trip to your local science museum and among the exhibits is one for mass and weight. The exhibit
290 has a gigantic scale, and you come up with a fun problem for your class.

291 You ask your class, "What is the total weight of the classroom? Give your best estimation to
292 me in 30 minutes, and then we'll check your guess on the scale. If your guess is within 10% of the
293 right answer, we will stop for ice cream on the way back."

294 The students are ecstatic to hear this, and they get to work. The solution is some variation of
295 the following strategy. The students should give each other their weight or best guess if they do
296 not know. Then, all they must do is add each student's weight and get a grand total for the class.
297 The measurement on the giant scale should show the true weight of the class. When comparing
298 the measured weight to your estimation, multiply the measurement by 1.0 ± 0.1 to get the $\pm 10\%$
299 tolerances for your estimation.

300 Two of your students, Sandra and Mario, return to you with a solution.

301 They say, "We weren't sure of everyone's weight. We used 65 lbs. for the people we didn't
302 know and added everyone who does know. There are 30 of us, and we got 2,000 lbs.! That's a ton!"

303 You estimated 1,900 lbs. assuming the average weight of a student in your class was 60 lbs.
304 So, you are pleased with Sandra's and Mario's answer. You instruct your students to all gather on
305 the giant scale and read off the weight together. To all your surprise, the scale reads *10,000 lbs.*!
306 10,000 is significantly more than a 10% error from 2,000. In fact, it is approximately 5 times more
307 massive than either your or your students' estimates. You think to yourself and conclude there
308 must be something wrong with the scale. You ask an employee to check the scale and verify it is
309 well calibrated. They confirm that the scale is in working order. You weigh a couple of students
310 individually to assess that the scale is well calibrated. Sandra weighs 59 lbs., and Mario weighs

311 62 lbs., typical weights for their age. You then weigh each student individually and see that their
312 weights individually do not deviate greatly from 60 lbs. So, where does all the extra weight come
313 from?

314 This thought experiment serves as an analogy to the Dark Matter problem. The important
315 substitution to make however is to replace the students with stars and the classroom with a galaxy,
316 say the Milky Way. Individually the mass of stars is well measured and defined with the Sun as our
317 nearest test case. However, when we set out to measure the mass of a collection of stars as large as
318 galaxies, our well-motivated estimation is wildly incorrect. There simply is no way to account for
319 this discrepancy except without some unseen, or dark, contribution to mass and matter in galaxies.
320 I set out in my thesis to narrow the possibilities of what this Dark Matter could be.

321 This chapter is organized like the following... **TODO: Text should look like ... Chapter x has**
322 **blah blah blah.**

323 2.2 Dark Matter Basics

324 Presently, a more compelling theory of cosmology that includes Dark Matter (DM) in order
325 to explain a variety of observations is Λ Cold Dark Matter, or Λ CDM. I present the evidence
326 supporting Λ CDM in Section 2.3 yet discuss the conclusions of the Λ CDM model here. According
327 to Λ CDM fit to observations on the Cosmic Microwave Background (CMB), DM is 26.8% of the
328 universe's current energy budget. Baryonic matter, stuff like atoms, gas, and stars, contributes to
329 4.9% of the universe's current energy budget [1, 2, 3].

330 DM is dark; it does not interact readily with light at any wavelength. DM also does not interact
331 noticeably with the other standard model forces (Strong and Weak) at a rate that is readily observed
332 [3]. DM is cold, which is to say that the average velocity of DM is below relativistic speeds [1].
333 'Hot' DM would not likely manifest the dense structures we observe like galaxies, and instead
334 would produce much more diffuse galaxies than what is observed [3, 1]. DM is old; it played a
335 critical role in the formation of the universe and the structures within it [1, 2].

336 Observations of DM have so far been only gravitational. The parameter space available to what
337 DM could be therefore is extremely broad. The broad DM parameter space is iteratively tested in

338 DM searches by supposing a hypothesis that has not yet been ruled out and performing observations
339 to test them. When the observations yield a null result, the parameter space is constrained further.
340 I present some approaches for DM searches in Section 2.4.

341 **2.3 Evidence for Dark Matter**

342 Dark Matter (DM) has been a looming problem in physics for almost 100 years. Anomalies
343 have been observed by astrophysicists in galactic dynamics as early as 1933 when Fritz Zwicky
344 noticed unusually large velocity dispersion in the Coma cluster. Zwicky's measurement was the
345 first recorded to use the Virial theorem to measure the mass fraction of visible and invisible matter
346 in celestial bodies [4]. From Zwicky in [5], "*If this would be confirmed, we would get the surprising*
347 *result that dark matter is present in much greater amount than luminous matter.*" Zwicky's and
348 others' observation did not instigate a crisis in astrophysics because the measurements did not
349 entirely conflict with their understanding of galaxies [4]. In 1978, Rubin, Ford, and Norbert
350 measured rotation curves for ten spiral galaxies [6]. Rubin et al.'s 1978 publication presented a
351 major challenge to the conventional understanding of galaxies that could no longer be dismissed by
352 measurement uncertainties. Evidence has been mounting ever since for this exotic form of matter.
353 The following subsections provide three compelling pieces of evidence in support of the existence
354 of DM.

355 **2.3.1 First Clues: Stellar Velocities**

356 Zwicky, and later Rubin, measured the stellar velocities of various galaxies to estimate their
357 virial mass. The Virial Theorem upon which these observations are interpreted is written as

$$2T + V = 0. \quad (2.1)$$

358 Where T is the kinetic energy and V is the potential energy in a self-gravitating system. The
359 classical Newton's law of gravity from stars and gas was used for gravitational potential modeled in
360 the observed galaxies:

$$V = -\frac{1}{2} \sum_i \sum_{j \neq i} \frac{m_i m_j}{r_{ij}}. \quad (2.2)$$

361 Zwicky et al. measured just the velocities of stars apparent in optical wavelengths [5]. Rubin et al.
 362 added by measuring the velocity of the hydrogen gas via the 21 cm emission line of Hydrogen [6].
 363 The velocities of the stars and gas are used to infer the total mass of galaxies and galaxy clusters
 364 via Equation (2.1). An inferred mass is obtained from the luminosity of the selected sources. The
 365 two inferences are compared to each other as a luminosity to mass ratio which typically yielded [1]

$$\frac{M}{L} \sim 400 \frac{M_{\odot}}{L_{\odot}} \quad (2.3)$$

366 M_{\odot} and L_{\odot} referring to stellar mass and stellar luminosity, respectively. These ratios clearly indicate
 367 a discrepancy in apparent light and mass from stars and gas and their velocities.

368 Rubin et al. [6] demonstrated that the discrepancy was unlikely to be an underestimation of
 369 the mass of the stars and gas. The inferred "dark" mass was up to 5 times more than the luminous
 370 mass. This dark mass also needed to extend well beyond the extent of the luminous matter.

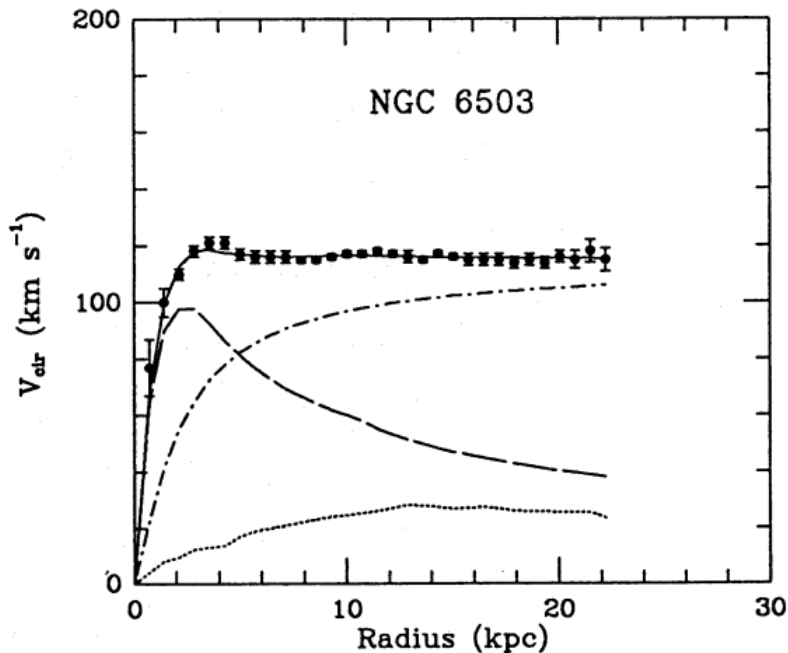


Figure 2.1 Rotation curve fit to NGC 6503 from [7]. Dashed line is the contribution from visible matter. Dotted curves are from gas. Dash-dot curves are from dark matter (DM). Solid line is the composite contribution from all matter and DM sources. Data are indicated with bold dots with error bars. Data agree strongly with a matter + DM composite prediction.

371 Figure 2.1 features one of many rotation curves plotted from the stellar velocities within galaxies.

372 The measured rotation curves mostly feature a flattening of velocities at higher radius which is not
373 expected if the gravity was only coming from gas and luminous matter. The extension of the
374 flat velocity region also indicates that the DM is distributed far from the center of the galaxy.
375 Modern velocity measurements include significantly larger objects, galactic clusters, and smaller
376 objects, dwarf galaxies. Yet, measurements along this regime are leveraging the Virial theorem
377 with Newtonian potential energies. We know Newtonian gravity is not a comprehensive description
378 of gravity. New observational techniques have been developed since 1978, and those are discussed
379 in the following sections.

380 **2.3.2 Evidence for Dark Matter: Gravitational Lensing**

381 Modern evidence for dark matter comes from new avenues beyond stellar velocities. Grav-
382 itational lensing from DM is a new channel from general relativity. General relativity predicts
383 aberrations in light caused by massive objects. In recent decades we have been able to measure the
384 lensing effects from compact objects and DM halos. Figure 2.2 shows how different massive ob-
385 jects change the final image of a faraway galaxy resulting from gravitational lensing. Gravitational
386 lensing developed our understanding of dark matter in two important ways.

387 Gravitational lensing provides additional compelling evidence for DM. The observation of two
388 merging galactic clusters in 2006, shown in Figure 2.3, provided a compelling argument for DM
389 outside the Standard Model. These clusters merged recently in astrophysical time scales. Galaxies
390 and star cluster have mostly passed by each other as the likelihood of their collision is low. Therefore,
391 these massive objects will mostly track the highest mass, dark and/or baryonic, density. Yet, the
392 intergalactic gas is responsible for the majority of the baryonic mass in the systems [4]. These gas
393 bodies will not phase through and will heat up as they collide together. The hot gas is located via
394 x-ray emission from the cluster. Two observations of the clusters were performed independently of
395 each other.

396 The first was the lensing of light around the galaxies due to their gravitational influences.
397 When celestial bodies are large enough, the gravity they exert bends space and time itself. The
398 warped space-time lenses light and will deflect in an analogous way to how glass lenses will bend

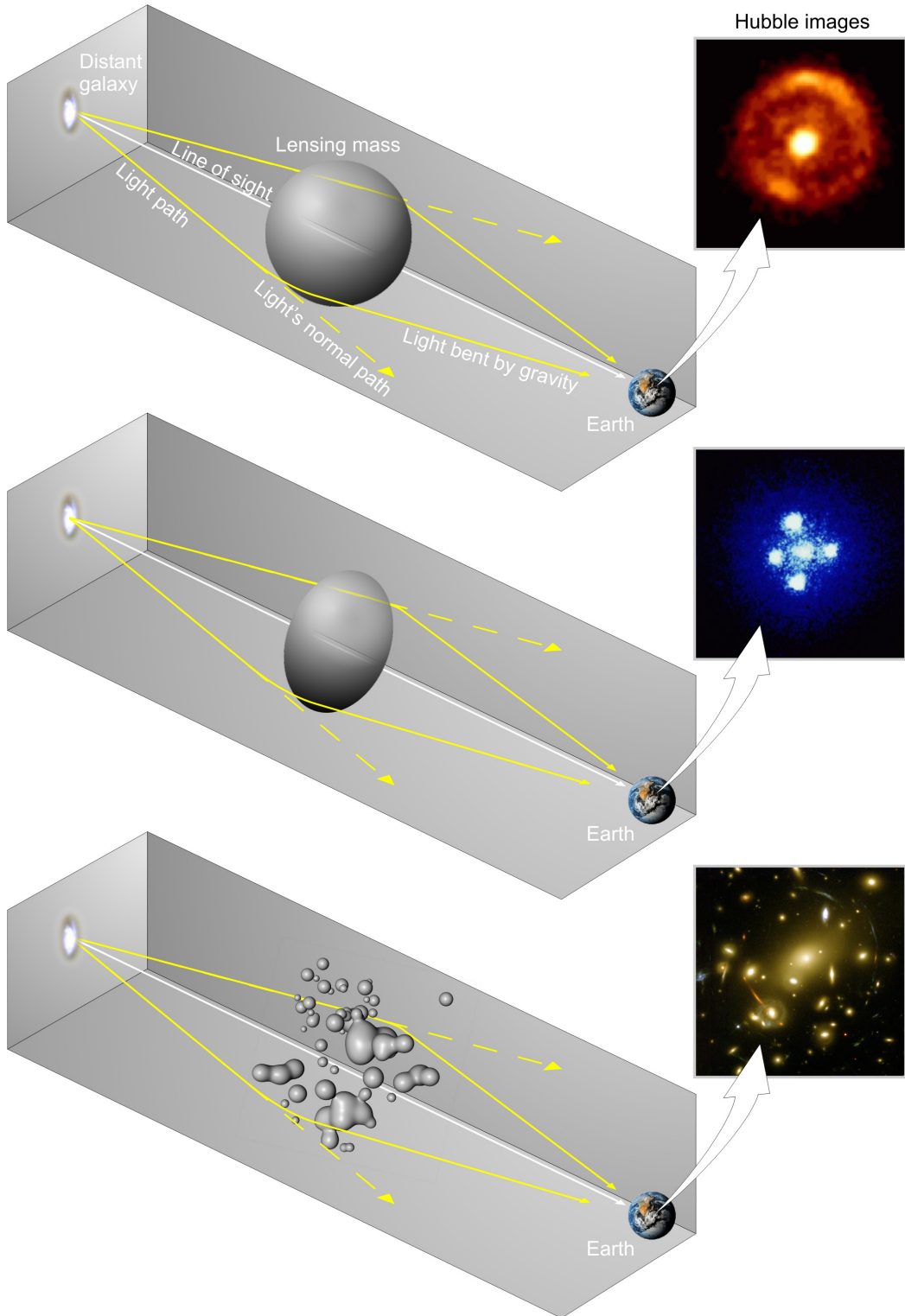


Figure 2.2 Light from distant galaxy is bent in unique ways depending on the distribution of mass between the galaxy and Earth. Yellow dashed lines indicate where the light would have gone if the matter were not present [8].

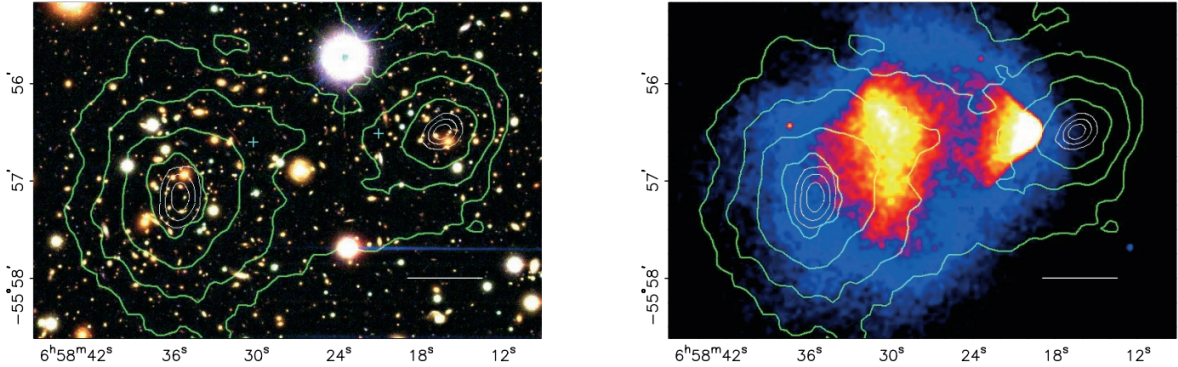


Figure 2.3 (left) Optical image of galactic cluster 1E0657-558. (right) X-ray image of the cluster with redder meaning hotter and higher baryon density. (both) Green contours are reconstruction of gravity contours from weak lensing. White rings are the best fit mass maxima at 68.3%, 95.5%, and 99.7% confidence. The matter maxima of the clusters are clearly separated from x-ray maxima. [9]

399 light, see Figure 2.2. With a sufficient understanding of light sources behind a massive object, we
 400 can reconstruct the contours of the gravitational lenses. The gradient of the contours shown in
 401 Figure 2.3 then indicates how dense the matter is and where it is.

402 The x-ray emission can then be observed from the clusters. Since these galaxies are mostly gas
 403 and are merging, then the gas should be getting hotter. If they are merging, the x-ray emissions
 404 should be the strongest where the gas is mostly moving through each other. Hence, X-ray emission
 405 maps out where the gas is in the merging galaxy cluster.

406 The lensing and x-ray observations were done on the Bullet cluster featured on Figure 2.3.
 407 The x-ray emissions do not align with the gravitational contours from lensing. The incongruence
 408 in mass density and baryon density suggests that there is a lot of matter somewhere that does
 409 not interact with light. Moreover, this dark matter cannot be baryonic [9]. The Bullet Cluster
 410 measurement did not really tell us what DM is exactly, but it did give the clue that DM also does
 411 not interact with itself very strongly. If DM did interact strongly with itself, then it would have been
 412 more aligned with the x-ray emission [9]. There have been follow-up studies of galaxy clusters with
 413 similar results. The Bullet Cluster and others like it provide a persuasive case against something
 414 possibly amiss in our gravitational theories.

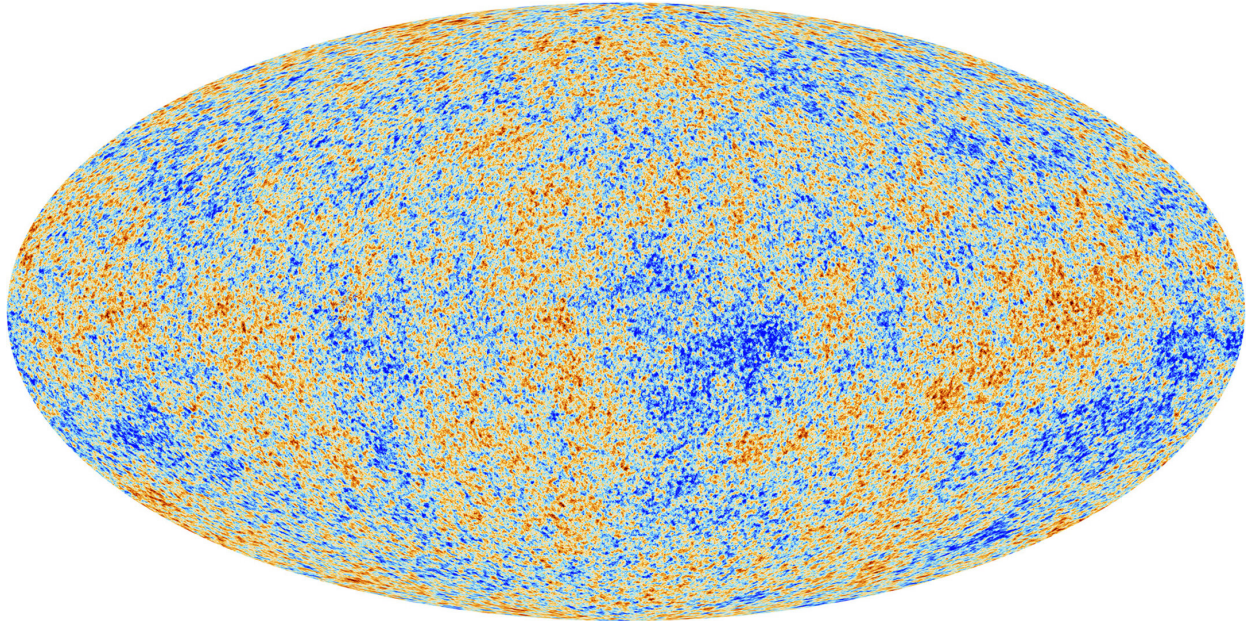


Figure 2.4 Plank CMB sky. Sky map features small variations in temperature in primordial light. These anisotropies are used to make inferences about the universe’s energy budget and developmental history. [10]

415 **2.3.3 Evidence for Dark Matter: Cosmic Microwave Background**

416 The Cosmic Microwave Background (CMB) is the primordial light from the early universe
417 when Hydrogen atoms formed from the free electron and proton soup in the early universe. The
418 CMB is the earliest light we can observe; released when the universe was about 380,000 years old.
419 Then we look at how the simulated universes look like compared to what we see. Figure 2.4 is the
420 most recent CMB image from the Plank satellite after subtracting the average value and masking the
421 galactic plane [10]. Redder regions indicate a slightly hotter region in the CMB, and blue indicates
422 colder. The intensity variations are on the order of 1 in 1000 with respect to the average value.

423 The Cosmic Microwave Background shows that the universe had DM in it from an incredibly
424 early stage. To measure the DM, Dark Energy, and matter fractions of the universe from the CMB,
425 the image is analyzed into a power spectrum, which shows the amplitude of the fluctuations as
426 a function of spherical multipole moments. Λ CDM provides the best fit to the power spectra of
427 the CMB as shown in Figure 2.5. The CMB power spectrum is quite sensitive to the fraction
428 of each energy contribution in the early universe. Low l modes are dominated by variations
429 in gravitational potential. Intermediate l emerge from oscillations in photon-baryon fluid from

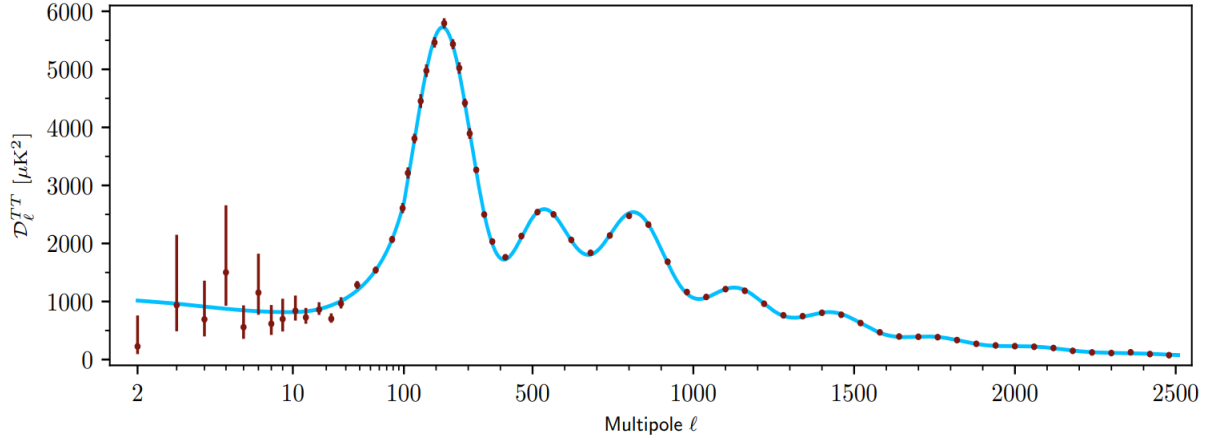


Figure 2.5 Observed Cosmic Microwave Background power spectrum as a function of multipole moment from Plank [10]. Blue line is best fit model from Λ CDM. Red points and lines are data and error, respectively.

430 competing baryon pressures and gravity. High l is a damped region from the diffusion of photons
 431 during electron-proton recombination. [1]

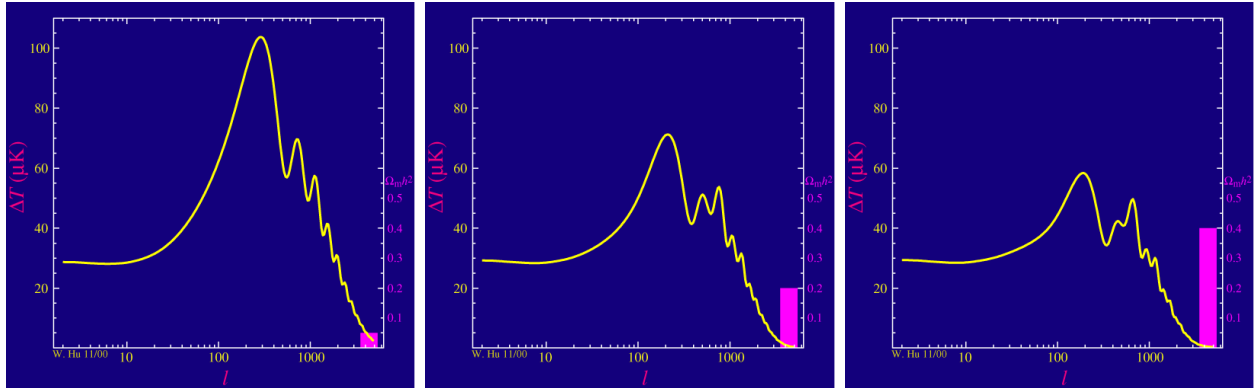


Figure 2.6 Predicted power spectra of CMB for different $\Omega_m h^2$ values for fixed baryon density from [11]. (left) Low $\Omega_m h^2$ increases the prominence of first and second peaks. (middle) $\Omega_m h^2$ is most similar to the observed power spectrum. The second and third peaks are similar in height. (right) $\Omega_m h^2$ is large which suppresses the first peak and raises the prominence of the third peak.

432 The harmonics would look quite different for a universe with less DM. Figure 2.6 demonstrates
 433 the effect $\Omega_m h^2$ has on the expected power spectrum for fixed baryon matter density. [11] Sweeping
 434 $\Omega_m h^2$ in this way clearly shows the effect dark matter has on the CMB power spectrum. The
 435 observations fit well with the Λ CDM model, and the derived fractions are as follows. The matter
 436 fraction: $\Omega_m = 0.3153$; and the baryon fraction: $\Omega_b = 0.04936$ [10]. Plank's observations also
 437 provide a measure of the Hubble constant, H_0 . H_0 especially has seen a growing tension in the

438 past decade that continues to deepened with observations from instruments like the James Webb
439 Telescope [12, 13]. As Hubble tensions deepen, we may find that perhaps Λ **CDM**, despite its
440 successes, is missing some critical physics.

441 Overall, the Newtonian motion of stars in galaxies, weak lensing from galactic clusters, and
442 power spectra from primordial light form a compelling body of research in favor of dark matter.
443 It takes another leap of theory and experimentation to make observations of DM that are non-
444 gravitational in nature. In Section 2.3, the evidence for DM implies strongly that the DM is matter
445 and not a lost parameter in the gravitational fields between massive objects. Finally, if we take one
446 axiom: that this matter has quantum behavior, such as being described by some Bohr wavelength
447 and abiding by some fermion or boson statistics; then we arrive at particle dark matter. One particle
448 DM hypothesis is the Weakly Interacting Massive Particle (WIMP). This DM candidate theory is
449 discussed further in the next section and is the focus of this thesis.

450 **2.4 Searching for Dark Matter: Particle DM**

451 Section 2.4 shows the Standard Model of particle physics and is currently the most accurate
452 model for the dynamics of fundamental particles like electrons and photons. The current status
453 of the SM does not have a viable DM candidate. When looking at the standard model, we can
454 immediately exclude any charged particle because charged particles interact strongly with light.
455 Specifically, this will rule out the following charged, fundamental particles: $e, \mu, \tau, W, u, d, s, c, t, b$
456 and their corresponding antiparticles. Recalling from Section 2.2 that DM must be long-lived and
457 stable over the age of the universe which excludes all SM particles with decay half-lives at or shorter
458 than the age of the universe. The lifetime constraint additionally eliminates the Z and H bosons.
459 Finally, the candidate DM needs to be somewhat massive. Recall from Section 2.2 that DM is cold
460 or not relativistic through the universe. This eliminates the remaining SM particles: $\nu_{e,\mu,\tau}, g, \gamma$ as
461 DM candidates. Because there are no DM candidates within the SM, the DM problem strongly
462 hints to physics beyond the SM (BSM).

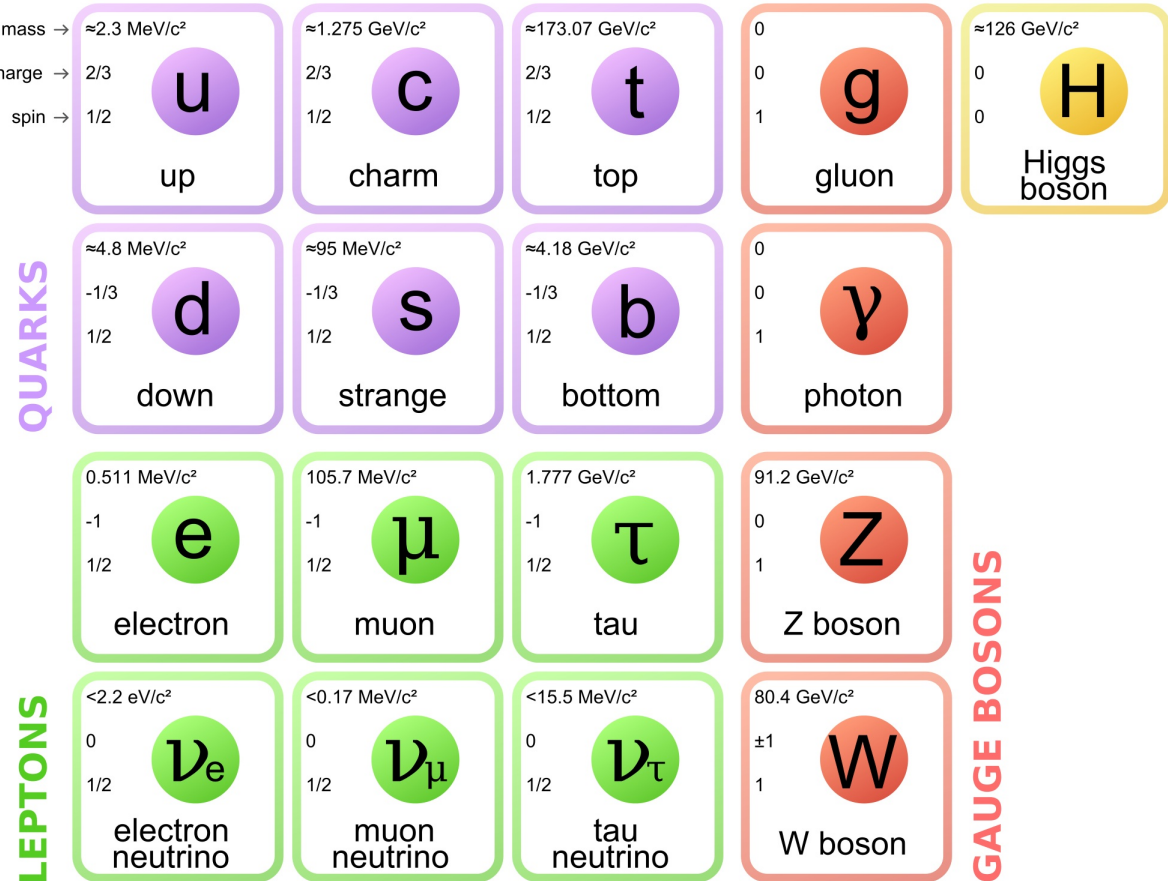


Figure 2.7 The Standard Model (SM) of particle physics. Figure taken from <http://www.quantumdiaries.org/2014/03/14/the-standard-model-a-beautiful-but-flawed-theory/>

463 2.4.1 Shake it, Break it, Make it

464 When considering DM that couples in some way with the SM, the interactions are roughly
 465 demonstrated by interaction demonstrated in Figure 2.8. The figure is a simplified Feynman
 466 diagram where the arrow of time represents the interaction modes of: **Shake it, Break it, Make it**.
 467 **Shake it** refers to the direct detection of dark matter. Direct detection interactions start with
 468 a free DM particle and an SM particle. The DM and SM interact via elastic or inelastic collision
 469 and recoil away from each other. The DM remains in the dark sector and imparts some momentum
 470 onto the SM particle. The hope is that the momentum imparted onto the SM particle is sufficiently
 471 high enough to pick up with extremely sensitive instruments. Because we cannot create the DM in
 472 the lab, a direct detection experiment must wait until DM is incident on the detector. Most direct
 473 detection experiments are therefore placed in low-background environments with inert detection

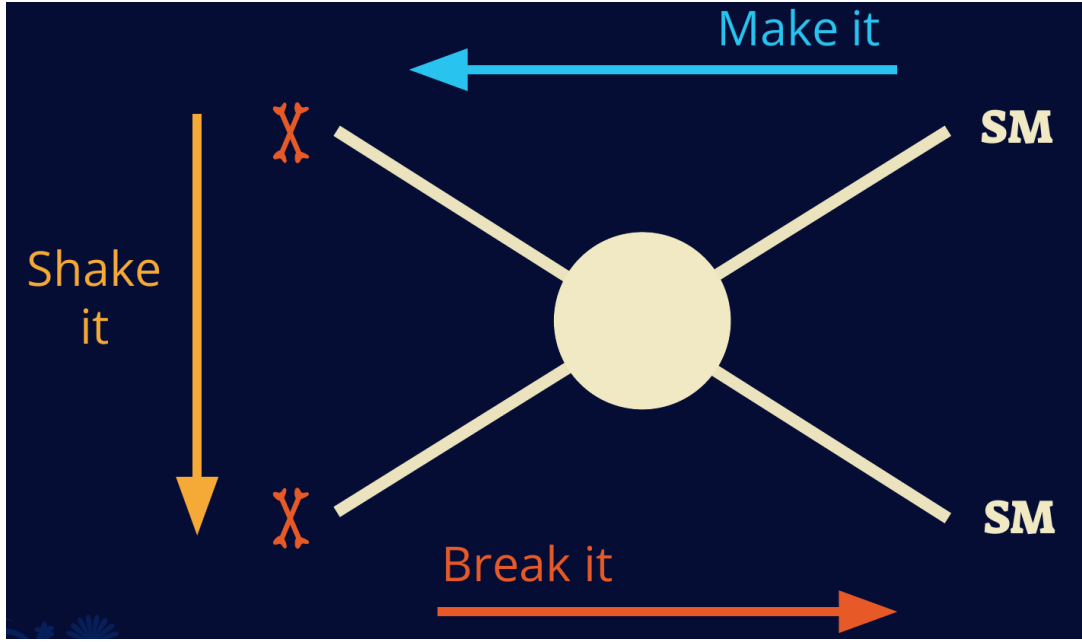


Figure 2.8 Simplified Feynman diagram demonstrating different ways DM can interact with SM particles. The 'X's refer to the DM particles whereas the SM refer to fundamental particles in the SM. The large circle in the center indicates the vertex of interaction and is purposely left vague. The colored arrows refer to different directions of time as well as their respective labels. The arrows indicate the initial and final state of the DM -SM interaction in time.

⁴⁷⁴ media like the noble gas Xenon. [14]

⁴⁷⁵ **Make it** refers to the production of DM from SM initial states. The experiment starts with
⁴⁷⁶ particles in the SM. These SM particles are accelerated to incredibly high energies and then collide
⁴⁷⁷ with each other. In the confluence of energy, DM hopefully emerges as a byproduct of the SM
⁴⁷⁸ annihilation. Often it is the collider experiments that are energetic enough to hypothetically produce
⁴⁷⁹ DM. These experiments include the world-wide collaborations ATLAS and CMS at CERN where
⁴⁸⁰ proton collide together at extreme energies. The DM searches, however, are complex. DM likely
⁴⁸¹ does not interact with the detectors and lives long enough to escape the detection apparatus of
⁴⁸² CERN's colliders. This means any DM production experiment searches for an excess of events
⁴⁸³ with missing momentum or energy in the events. An example event with missing transverse
⁴⁸⁴ momentum is shown in Figure 2.9. The missing momentum with no particle tracks implies a
⁴⁸⁵ neutral particle carried the energy out of the detector. However, there are other neutral particles
⁴⁸⁶ in the SM, like neutrons or neutrinos, so any analysis has to account for SM signatures of missing

487 momentum. [15]

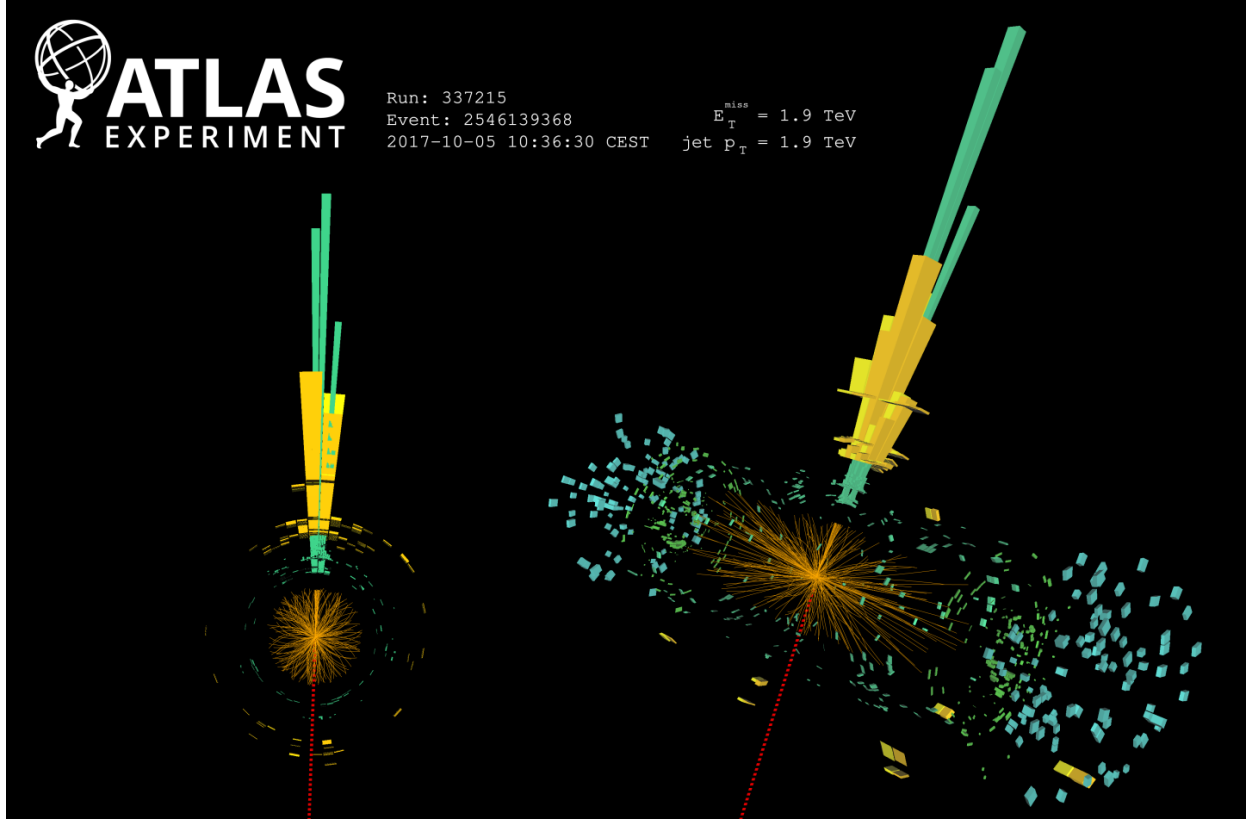


Figure 2.9 A single jet event in ATLAS detector from 2017 [16]. Jet momentum was observed to be 1.9 TeV. Missing transverse momentum was observed to be 1.9 TeV compared to the initial transverse momentum of the event was 0. Implied MET is traced by a red dashed line in event display.

488 2.4.2 Break it: Standard Model Signatures of Dark Matter through Indirect Searches

489 **Break it** refers to the creation of SM particles from the dark sector, and it is the primary focus
490 of this thesis. The interaction begins with DM or in the dark sector. The hypothesis is that this
491 DM will either annihilate with itself or decay and produce an SM byproduct. This method is
492 often referred to as the Indirect Detection of DM because we have no lab to directly control or
493 manipulate the DM. Therefore, most indirect DM searches are performed using observations of
494 known DM densities among the astrophysical sources. The strength is that we have the whole of the
495 universe and its 13.6-billion-year lifespan to use as a detector and particle accelerator. Additionally,
496 locations of dark matter are well cataloged since it was astrophysical observations that presented

497 the problem of DM in the first place.

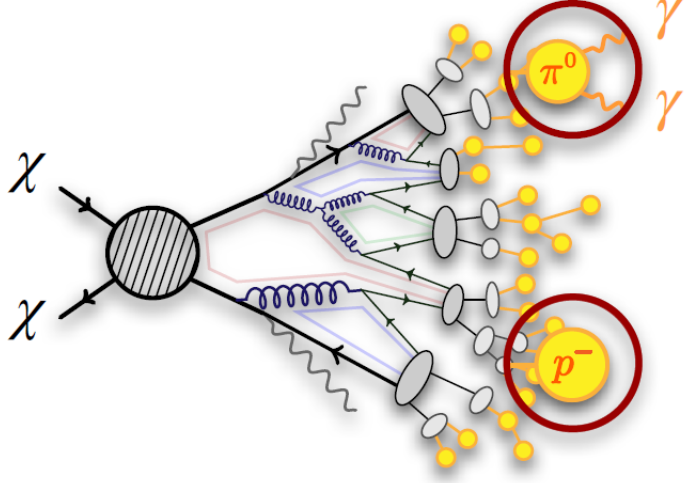


Figure 2.10 More detailed pseudo-Feynman diagram of particle cascade from dark matter annihilation into 2 quarks. The quarks hadronize and down to stable particles like γ or the anti-proton (p^-). Diagram pulled from ICRC 2021 presentation on DM annihilation search [17].

498 However, anything can happen in the universe. There are many difficult to deconvolve back-
499 grounds when searching for DM. One prominent example is the galactic center. We know the
500 galactic center has a large DM content because of stellar kinematics in our Milky Way and DM halo
501 simulations. Yet, any signal from the galactic center is challenging to parse apart from the extreme
502 environment of our supermassive black hole, unresolved sources, and diffuse emission from the
503 interstellar medium [18]. Despite the challenges, any DM model that yields evidence in the other
504 two observation methods, **Shake it or Make it** must be corroborated with indirect observations of
505 the known DM sources. Without corroborating evidence, DM observation in the lab is hard-pressed
506 to demonstrate that it is the model contributing to the DM seen at the universal scale.

507 In the case of WIMP DM, signals are described in terms of primary SM particles produced
508 from DM decay or annihilation. The SM initial state particles are then simulated down to stable
509 final states such as the γ , ν , p , or e which can traverse galactic lengths to reach Earth.

510 Figure 2.10 shows the quagmire of SM particles that emerges from SM initial states that are not
511 stable [17]. There are many SM particles with varying energies that can be produced in such an

512 interaction. For any arbitrary DM source and stable SM particle, the SM flux from DM annihilating
 513 to a neutral particle in the SM, ϕ , from a region in the sky is described by the following.

$$\frac{d\Phi_\phi}{dE_\phi} = \frac{\langle\sigma v\rangle}{8\pi m_\chi^2} \frac{dN_\phi}{dE_\phi} \times \int_{\text{source}} d\Omega \int_{l.o.s} \rho_\chi^2 dl(r, \theta') \quad (2.4)$$

514 In Equation (7.1), $\langle\sigma v\rangle$ is the velocity-weighted annihilation cross-section of DM to the SM. m_χ
 515 refers to the mass of DM, noted with Greek letter χ . $\frac{dN_\phi}{dE_\phi}$ is the N particle flux weighted by the
 516 particle energy. An example is provided in Figure 2.11 for the γ final state. The integrated terms
 517 are performed over the solid angle, $d\Omega$, and line of sight, l.o.s. ρ is the density of DM for a
 518 location (r, θ') in the sky. The terms left of the ' \times ' are often referred to as the particle physics
 519 component. The terms on the right are referred to as the astrophysical component. For decaying
 520 DM, the equation changes to...

$$\frac{d\Phi_\phi}{dE_\phi} = \frac{1}{4\pi\tau m_\chi} \frac{dN_\phi}{dE_\phi} \times \int_{\text{source}} d\Omega \int_{l.o.s} \rho_\chi dl(r, \theta') \quad (2.5)$$

521 In Equation (8.1), τ is the decay lifetime of the DM. Just as in Equation (7.1), the left and right
 522 terms are the particle physics and the astrophysical components respectively. The integrated
 523 astrophysical component of Equation (7.1) is often called the J-Factor. Whereas the integrated
 524 astrophysical component of Equation (8.1) is often called the D-Factor.

525 Exact DM $\text{DM} \rightarrow \text{SM SM}$ branching ratios are not known, so it is usually assumed to go 100%
 526 into an SM particle/anti-particle. Additionally, when a DM annihilation or decay produces one of
 527 the neutral, long-lived SM particles (ν or γ), the particle is traced back to a DM source. For DM
 528 above GeV energies, there are very few SM processes that can produce particles with such a high
 529 energy. Seeing such a signal would almost certainly be an indication of the presence of dark matter.
 530 Fortunately, the universe provides us with the largest volume and lifetime ever for a particle physics
 531 experiment.

532 2.5 Sources for Indirect Dark Matter Searches

533 The first detection of DM relied on optical observations. Since then, we have developed new
 534 techniques to find DM dense regions. As described in Section 2.3.1, many DM dense regions were
 535 through observing galactic rotation curves. Our Milky Way galaxy is among DM dense regions

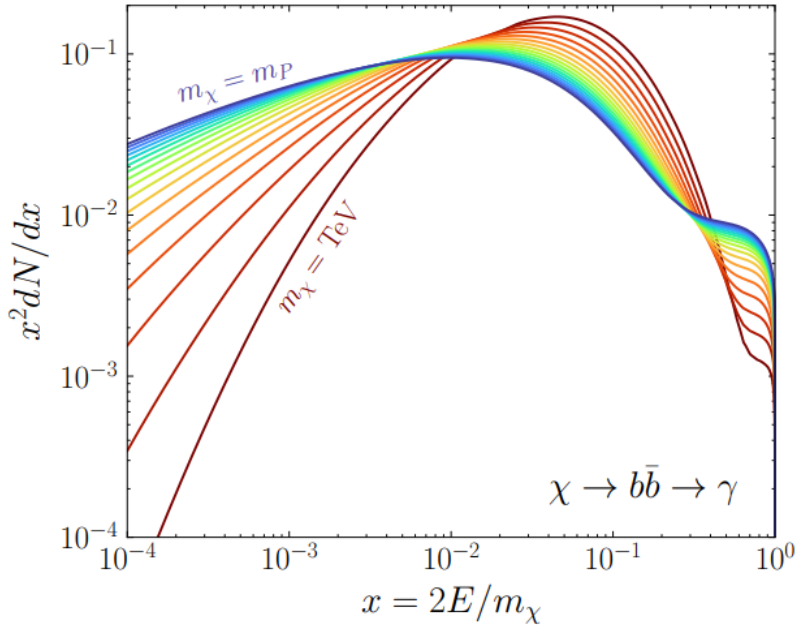


Figure 2.11 Dark Matter (DM) decay spectrum for $b\bar{b}$ initial state and γ final state. Redder spectra are for larger DM masses. Bluer spectra are light DM masses. x is a unitless factor defined as the ratio of the mass of DM, m_χ , and the final state particle energy E_γ . Figure from [19].

discovered, and it is the largest nearby DM dense region to look at. Additionally, the DM halo surrounding the Milky Way is clumpy [18]. There are regions in the DM halo of the Milky Way that have more DM than others that have captured gas over time. These sub-halos were dense enough collapse gas and form stars. These apparent sub galaxies are known as dwarf spheroidal galaxies and are the main sources studied in this thesis. Each source type comes with different trade-offs. Galactic Center studies will be very sensitive to the assumed distribution of DM. The central DM density can vary substantially as demonstrated in Figure 2.12. At distances close to the center of the galaxy, or small r , the differences in DM densities can be 3-4 orders of magnitude. Searches toward the galactic center will therefore be quite sensitive to the assumed DM distribution.

Searches toward Dwarf Spheroidal Galaxies (dSph's) suffer from uncertainties in the DM density less than the galactic center studies. This is mostly from their diminutive size being smaller than the angular resolution of most γ -ray observatories [18]. The DM content dSph's are typically determined with the Virial theorem, Equation (2.1), and are usually majority DM [18] in mass. DSph's tend to be ideal sources to look at for DM searches. Their environments are quiet with little

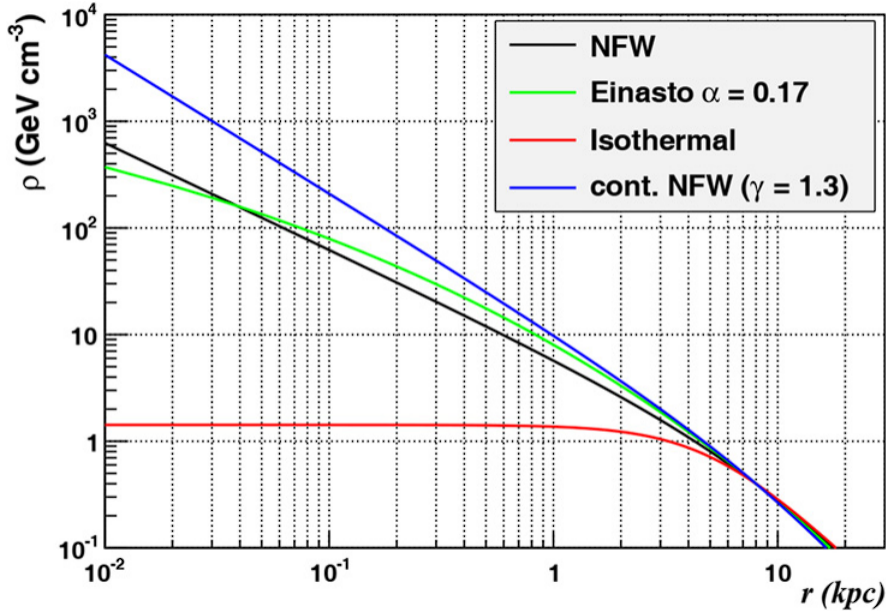


Figure 2.12 Different dark matter density profiles compared. Some models produce exceptionally large densities at small r [20].

550 astrophysical background. Unlike the galactic center, the most active components of dSph's are the
 551 stars within them versus a violent accretion disc around a black hole. All this together means that
 552 dSph's are among the best sources to look at for indirect DM searches. dSph's are the targets of
 553 focus for this thesis.

554 2.6 Multi-Messenger Dark Matter

555 Astrophysics entered a new phase in the past few decades that leverages our increasing sensitivity
 556 to SM channels and general relativity (GR). Up until the 21st century, astrophysical observations
 557 were performed with photons (γ) only. Astrophysics with this 'messenger' is fairly mature now.
 558 Novel observations of the universe have since only adjusted the sensitivity of the wavelength of
 559 light that is observed except at MeV energies. Gems like the CMB [10], and more have ultimately
 560 been observations of different wavelengths of light. Multi-messenger astrophysics proposes using
 561 other SM particles such the p^{+-} , or ν or gravitation waves predicted by general relativity.

562 The experiment LIGO had a revolutionary discovery in 2016 with the first detection of a binary
 563 black hole merger [21]. This opened the collective imagination to observing the universe through
 564 gravitational waves. There has also been a surge of interest in the neutrino (ν) sector. IceCube

565 demonstrated that we are sensitive to neutrinos in regions that correlate with significant photon
 566 emission like the galactic plane [22]. Neutrinos, like gravitational waves and light, travel mostly
 567 unimpeded from their source to our observatories. This makes pointing to the originating source
 568 of these messengers much easier than it is for cosmic rays which are deflected from their source by
 569 magnetic fields.

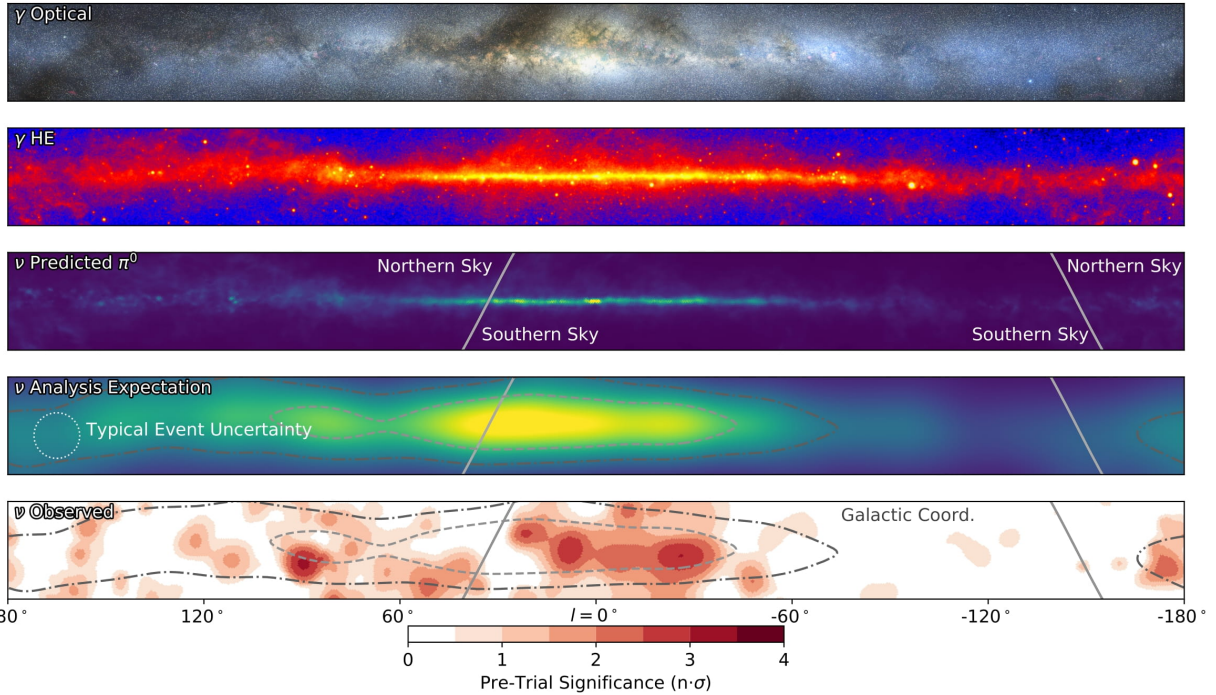


Figure 2.13 The Milky Way Galaxy in photons (γ) and neutrinos (ν) [22]. The Galactic center is at $l=0^\circ$ and is the brightest region in all panels. (top) An Optical color image of the Milky Way galaxy seen from Earth. Clouds of gas and dust obscure some light from stars. (2nd down) Integrated flux of γ -rays observed by the Fermi-LAT telescope [23]. (middle) Expected neutrino emission that corresponds with Fermi-LAT observations. (2nd up) Expected neutrino emission profile after considering detector systematics of IceCube. (bottom) Observed neutrino emission from region of the galactic plane. Substantial neutrino emission was detected.

570 The IceCube collaboration recently published a groundbreaking result of the Milky Way in
 571 neutrinos. The recent result from IceCube, shown in Figure 2.13, proves that we can make
 572 observations under different messenger regimes. The top two panels show the appearance of the
 573 galactic plane to different wavelengths of light. Some sources are more apparent in some panels,
 574 while others are not. This new channel is powerful because neutrinos are readily able to penetrate
 575 through gas and dust in the Milky Way. This new image also refines our understanding of how high

576 energy particles are produced. For example, the fit to IceCube data prefers neutrino production
 577 from the decay of π^0 [22].

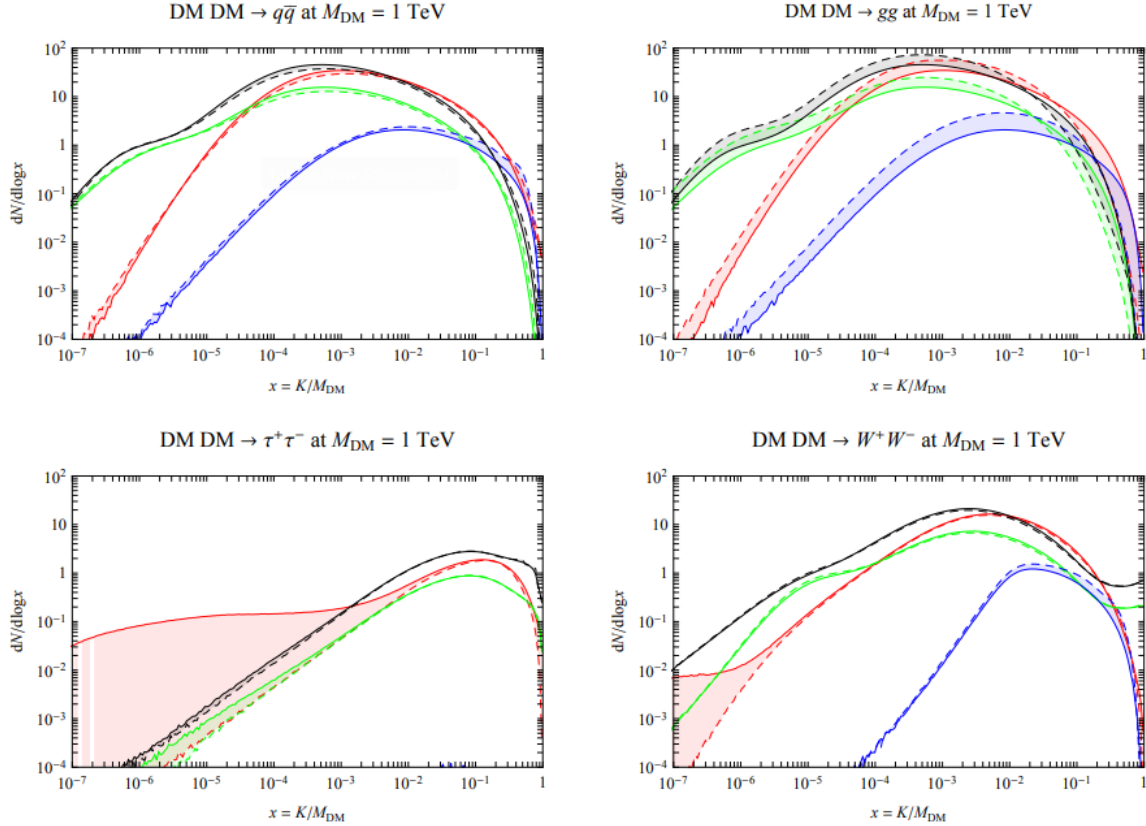


Figure 2.14 Dark Matter annihilation spectra for different final state particle and standard model annihilation channels [24]. Photons (red), e^\pm (green), \bar{p} (blue), ν (black).

578 Exposing our observations to more cosmic messengers greatly increases our sensitivity to
 579 rare processes. In the case of DM, Figure 2.14, there are many SM particles produced in DM
 580 annihilation. Among the final state fluxes are gammas and neutrinos. Charged particles are also
 581 produced however they would not likely make it to Earth since they will be deflected by magnetic
 582 fields between the source and Earth. This means observatories that can see the neutral messengers
 583 are especially good for DM searches and for combining data for a multi-messenger DM search.

CHAPTER 3

584 MULTIMESSENGER ASTROPHYSICS: DETECTING HIGH ENERGY NEUTRAL 585 MESSENGERS

586 3.1 Introduction

587 Before the 20th century, all asttrophysics observations were optical in nature. We litterly only
588 saw things with highly magnified optical observations. Then we discovered cosmic rays. cosmic
589 rays are charged particles, typically naked protons or H+. This was seen by Victor Hess in 19??.
590 Around the same time we discovered neutrinos from beta decay. Sometime around 1950 we started
591 to build neutrino detectors which were mostly sensitive to neutrinos from the sun. Finally, it was
592 theorized that compact objects like black holes and neutron stars would create waves in space-time
593 when they experience mergers or collisions.

594 In the 21st century, we have developed new observation techniques and detectors that are no only
595 sensitive to these four messengers - photons (TODO: photon), neutrinos (TODO: nu), Cosmic
596 Rays (CR), and Gravitational Wave (WV) - we're collect high energy versions of these events.
597 For the standad model particles, we're now sensitive to all messengers above the MeV eneryg
598 range. Additionally, the GW's were sensitive to are in the stellar mass black hole region and above
599 within our galactic neighborhood. This means were becoming sensitive to the fundamental physics
600 occuring within the universe and we can rely on the universe as a TeV+ particle accelerator. We
601 also have the abaility to correlate high energy events across messengers and gain new insights on
602 the processes that occur in our universe.

603 This thesis focuses on very high energy (VHE) gamma rays and neutrinos. These can both be
604 observed through the water cherenkov detection technique altho not exclusively. Methods on how
605 to detect and observe these neutral messengers are discussed Section 3.3 and Section 3.4

606 3.2 Charged Particles in a Medium

607 For high enery gamma-rays and neutrinos, we can exploit the same effect that charged particles
608 have with water. This effect is known as Cherenkov radiation. Cherenkov Radiation occurs when a
609 charged particle, usually electrons (e) or muons (μ), traverse a medium, like water, faster than the

610 speed of light in that medium. This is similar to sonic boom where an object moves through air
611 faster than the speed of sound in air. Cherenkov radiation can therefore be thought of as an 'optic
612 boom'. Many astro-particle physics experiments will use water as the medium as because water
613 has a unique set of properties ideal for charged particle tracking.



Figure 3.1 TODO: Show a nuclear reactor with cherenkov radiation[NEEDS A SOURCE][FACT CHECK THIS]

614 The frequency of light emitted due to cherenkov radiation follows the equation:

$$INSERT\ Cherenkov\ wavelength\ calc\ HERE. \quad (3.1)$$

615 The absorption spectra is shown in the following figure:

616 **3.3 Photons (γ)**

617 **3.4 Neutrinos (ν)**

618 **3.5 Opportunities to Combine for Dark Matter**



Figure 3.2 TODO: absorption spectrum of liquid and solid water[NEEDS A SOURCE][FACT CHECK THIS]

CHAPTER 4

619 HIGH ALTITUDE WATER CHERENKOV (HAWC) OBSERVATORY

620 4.1 The Detector

621 4.2 Events Reconstruction and Data Acquisition

622 4.2.1 G/H Discrimination

623 4.2.2 Angle

624 4.2.3 Energy

625 4.3 Remote Monitoring

626 4.3.1 ATHENA Database

627 4.3.2 HOMER

CHAPTER 5

ICECUBE NEUTRINO OBSERVATORY

629 **5.1 The Detector**

630 **5.2 Events Reconstruction and Data Acquisition**

631 **5.2.1 Angle**

632 **5.2.2 Energy**

633 **5.3 Northern Test Site**

634 **5.3.1 PIgeon remote dark rate testing**

635 **5.3.2 Bulkhead Construction**

CHAPTER 6

COMPUTATIONAL TECHNIQUES IN PARTICLE ASTROPHYSICS

637 **6.1 Neural Networks for Gamma/Hadron Separation**

638 **6.2 Parallel Computing for Dark Matter Analyses**

CHAPTER 7

639 **GLORY DUCK: MULTI-WAVELENGTH SEARCH FOR DARK MATTTER** 640 **ANNIHILATION TOWARDS DWARF SPHEROIDAL GALAXIES**

641 **7.1 Introduction**

642 The field of astrophysics now has several instruments and observatories sensitive to high
643 energy gamma-rays. The energy sensitivity for the modern gamma-ray program spans many orders
644 of magnitude. Figure 7.1 demonstrates these similar sensitivities across energies for the five
645 experiments: Fermi-LAT, HAWC, HESS, MAGIC, and VERITAS.

646 Each of the five experiments featured in Figure 7.1 have independently searched for DM
647 annihilation from dwarf spheroidal galaxies (dSph) and set limits. Intriguingly, there are regions of
648 substantial overlap in their energy sensitivities. This clearly motivates an analysis that combines data
649 from these five. Each experiment has unique gamma-ray detection methods and their weaknesses
650 and strengths can be leveraged with each other. The HAWC gamma-ray observatory is extensively
651 introduced in chapter 4, so it is not introduced here. A brief description of the remaining experiments
652 are in the following paragraphs.

653 The Large Area Telescope (LAT) is a pair conversion telescope mounted on the NASA Fermi
654 satellite in orbit \sim 550 km above the Earth [26]. LAT's field of view covers about 20% of the
655 whole sky, and it sweeps the whole sky approximately every 3 hours. LAT's gamma-ray energy
656 sensitivity ranges from 20 MeV up to 1 TeV. Previous DM searches towards dSphs using Fermi-LAT
657 are published in [27] and [28]

658 The High Energy Spectroscopic System (HESS), Major Atmospheric Gamma Imaging
659 Cherenkov (MAGIC), and Very Energetic Radiation Imaging Telescope Array System (VERI-
660 TAS) are arrays of Imaging Atmospheric Cherenkov Telescopes (IACT). These telescopes observe
661 the Cherenkov light emitted from gamma-ray showers in the Earth's atmosphere. The field of
662 view for these telescopes is no larger than 5° with energy sensitivities ranging from 30 GeV up
663 to 100 TeV [29, 30, 31]. IACTs are able to make precise observations in selected regions of the
664 sky, however can only be operated in ideal dark conditions. HESS's observations of the dwarves

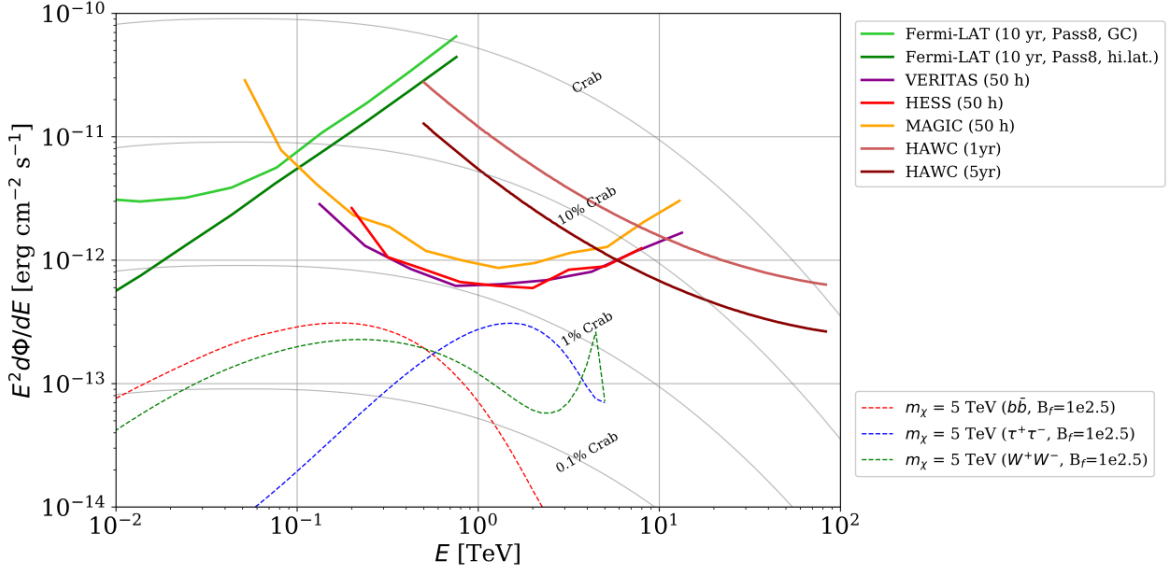


Figure 7.1 Sensitivities of five gamma-ray experiments compared to percentages of the Crab nebula’s emission and dark matter annihilation. Solid lines present estimated sensitivities to power law spectra [FACT CHECK THIS] for each experiment. Green lines are Fermi-LAT sensitivities where lighter green is the sensitivity to the galactic center and dark green is its sensitivity to higher declinations. Orange, red, and purple solid lines represent the MAGIC, HESS, and VERITAS 50 hour sensitivities respectively. The maroon and brown lines are the HAWC 1 year and 5 year sensitivities. Across four decades of gamma-ray energy, these experiments have similar sensitivities on the order 10^{-12} erg $\text{cm}^{-2}\text{s}^{-1}$. The dotted lines are estimated dark matter fluxes assuming $m_\chi = 5$ TeV DM annihilating to bottom quarks (red), tau leptons (blue), and W bosons (green). Faded gray lines outline percentage flux of the Crab nebula. Figure is an augmented version of [25]

665 Sculptor and Carina were between January 2008 and December 2009. HESS’s observations of
 666 Coma Berenices were from 2010 to 2013, and Fornax was observed in 2010 [32, 33, 34]. MAGIC
 667 provided deep observations of Segue1 between 2011 and 2013 [35]. MAGIC also provides data
 668 for three dwarves: Coma Berenices, Draco, and Ursa Major II where observations were made
 669 in: January - June 2019 [36], March - September 2018 [36], and 2014 - 2016 [37] respectively.
 670 VERITAS provided data for Boötes I, Draco, Segue 1, and Ursa Minor from 2009 to 2016 [38].

671 This chapter presents the Glory Duck analysis, the name given for the search for dark matter
 672 annihilation from dSph by combining data from the five gamma-ray observatories: Fermi-LAT,
 673 HAWC, HESS, MAGIC, and VERITAS. Specifically, the methods in analysis and modeling are
 674 presented for the HAWC gamma-ray observatory. This work was published to the Journal of
 675 Cosmology and Astroparticle Physics and presented at the International Cosmic Ray Conference

676 in 2019, 2021, and 2023 [39, 40, 41] and others.

677 **7.2 Dataset and Background**

678 This section enumerates the data and background methods used for HAWC’s study of dSphs.
679 Section 7.2.1 and Section 7.2.2 are most useful for fellow HAWC collaborators looking to replicate
680 the Glory Duck analysis.

681 **7.2.1 Itemized HAWC files**

- 682 • Detector Resolution: `response_aerie_svn_27754_systematics_best_mc_test_no`
683 `broadpulse_10pctlogchargesmearing_0.63qe_25kHzNoise_run5481_curvatu`
684 `re0_index3.root`
- 685 • Data Map: `maps-20180119/liff/maptree_1024.root`
- 686 • Spectral Dictionary: `DM_CirrelliSpectrum_dict_gammas.npy`
- 687 • Analysis wiki: https://private.hawc-observatory.org/wiki/index.php/Glory_Duck_Multi-Experiment_Dark_Matter_Search

689 **7.2.2 Software Tools and Development**

690 This analysis was performed using HAL and 3ML [42, 43] in Python version 2. I built software
691 to implement the *A Poor Particle Physicist Cookbook for Dark Matter Indirect Detection* (PPPC)
692 [44] DM spectral model and dSphs spatial model from [45] for HAWC analysis. A NumPy version
693 of this dictionary was made for both Py2 and Py3. The code base for creating this dictionary is
694 linked on my GitLab sandbox:

- 695 • Py2: [Dictionary Generator \(Deprecated\)](#)
- 696 • Py3: [PPPC2Dict](#)

697 The analysis was performed using the f_{hit} framework performed in the HAWC Crab paper
698 [42]. The Python2 NumPy dictionary file for gamma-ray final states is `dmCirSpecDict.npy`. The
699 corresponding Python3 file is `DM_CirrelliSpectrum_dict_gammas.npy`. These files can also

700 be used for decay channels and the PPPC describes how [44]. All other software used for data
701 analysis, DM profile generation, and job submission to SLURM are also kept in my sandbox for
702 [the Glory Duck](#) project.

703 **7.2.3 Data Set and Background Description**

704 The HAWC data maps used for this analysis contain 1017 days of data between runs 2104
705 (2014-11-26) and 7476 (2017-12-20). They were generated from pass 4.0 reconstruction. The
706 analysis is performed using the f_{hit} energy binning scheme with bins (1-9) similar to what was done
707 for the Crab and previous HAWC dSph analysis [42, 46]. Bin 0 was excluded as it has substantial
708 hadronic contamination and poor angular resolution.

709 This analysis was done on dSphs because of their large DM mass content relative to baryonic
710 mass. We consider the following to estimate the background to this study.

- 711 • The dSphs are small in HAWC’s field of view, so the analysis is not sensitive to large or small
712 scale anisotropies.
- 713 • The dSphs used in this analysis are off the galactic plane.
- 714 • The dSphs are baryonically faint relative to their expected dark matter content and are not
715 expected to contain high energy gamma-ray sources.

716 Therefor we make no additional assumptions on the background from our sources and use
717 HAWC’s standard direct integration method for background estimation [42]. It is possible for
718 gamma rays from DM annihilation to scatter in transit to HAWC via Inverse Compton Scattering
719 (ICS). This was investigated and its impact on the flux is basically zero. Supporting information
720 on this is in Section 7.7.1

721 **7.3 Analysis**

722 The expected differential photon flux from DM-DM annihilation to standard model particles,
723 $d\Phi_\gamma/dE_\gamma$, over solid angle, Ω is described by the familiar equation.

$$\frac{d\Phi_\gamma}{dE_\gamma} = \frac{\langle\sigma v\rangle}{8\pi m_\chi^2} \frac{dN_\gamma}{dE_\gamma} \times \int_{\text{source}} d\Omega \int_{l.o.s} \rho_\chi^2 dl(r, \theta') \quad (7.1)$$

724 Where $\langle \sigma v \rangle$ is the velocity weighted annihilation cross-section. $\frac{dN}{dE}$ is the expected differential
 725 number of photons produced at each energy per annihilation. m_χ is the rest mass of the supposed
 726 DM particle. ρ_χ is the DM density. J is the astrophysical J-factor and is defined as

$$J = \int d\Omega \int_{l.o.s} dl \rho_\chi^2(r, \theta') \quad (7.2)$$

727 l is the distance to the source from Earth. r is the radial distance from the center of the source. θ' is
 728 the half angle defining a cone containing the DM source. How each component is synthesized and
 729 considered for HAWC's analysis is presented in the following sections. Section 7.3.1 presents the
 730 particle physics model for DM annihilation. Section 7.3.2 presents the spatial distributions built
 731 for each dSph.

732 7.3.1 $\frac{dN_\gamma}{dE_\gamma}$ - Particle Physics Component

733 For these spectra, we import the PPPC with Electroweak (EW) corrections [44]. The spectrum
 734 is implemented as a model script in astromodels for 3ML. The EW corrections were previously not
 735 considered for HAWC and are significant for DM annihilating to EW coupled SM particles such
 736 as all leptons, and the γ , Z , and W bosons [46]. Figure 7.2 demonstrates the significance of EW
 737 corrections for W boson annihilation. Across EW SM channels, the gamma-ray spectra become
 738 harder than spectra without EW corrections. Tables from the PPPC were reformatted into Python
 739 NumPy dictionaries for collaboration-wide use. A class in astromodels was developed to include
 740 the EW correction from the PPPC and is aptly named `PPPCSpectra` within `DM_models.py`.

741 7.3.2 J - Astrophysical Component

742 The J-factor profiles for each source are imported from Geringer-Sameth (referred to with \mathcal{GS})
 743 [45]. These were pulled from the publication as $J(\theta)$, where θ is the angular separation from the
 744 center of the source. HAWC requires maps in terms of $\frac{dJ}{d\Omega}$, so the conversion from the maps was
 745 done in the following way...

746 First, convert the angular distances to solid angles

$$\Omega = 2 \cdot \pi(1 - \cos(\theta)) \quad (7.3)$$

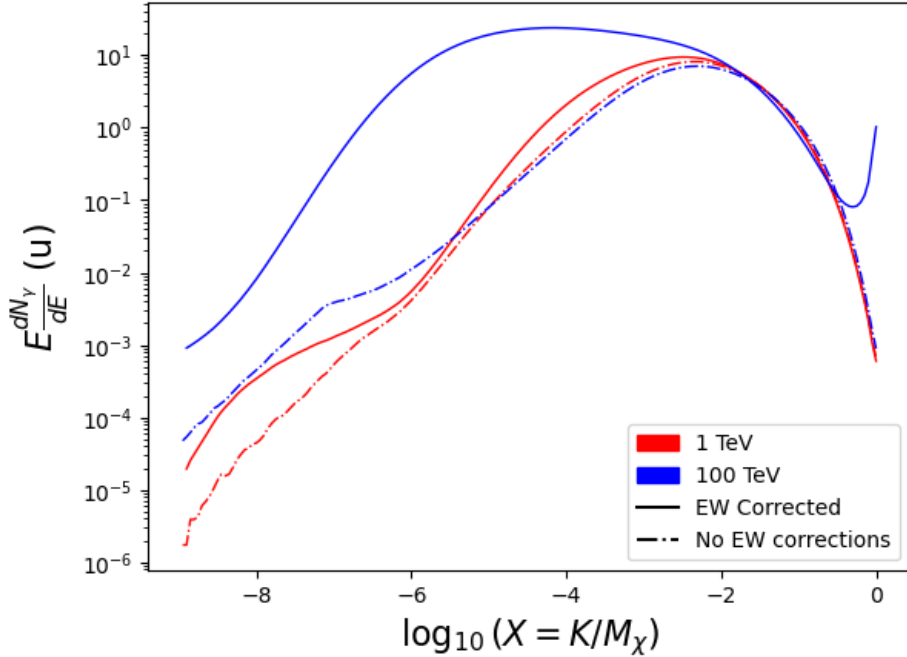


Figure 7.2 Effect of Electroweak (EW) corrections on expected DM annihilation spectrum for $\chi\chi \rightarrow W^-W^+$. Solid lines are spectral models that consider EW corrections. Dash-dot lines are spectral models without EW corrections. Red lines are models for $M_\chi = 1$ TeV. Blue lines represent models for $M_\chi = 100$ TeV. All models are sourced from the PPPC4DMID [44].

747 which reduces with a small angle approximation to $\pi\theta^2$. Next, the central difference for both the
 748 ΔJ and $\Delta\Omega$ value were calculated from the discretized $J(\theta)$ with the central difference stencil:

$$\Delta\phi_i = \phi_{i+1} - \phi_{i-1} \quad (7.4)$$

749 Where ϕ is either Ω or J . These were done separately in case the grid spacing in θ was not uniform.
 750 Finally, these lists are divided so that we are left with an approximation of the $dJ/d\Omega$ profile that
 751 is a function of θ . Admittedly, this is an approximation method for the map which introduces small
 752 errors compared to the true profile estimate. This was checked as a systematic against the author's
 753 profiling of the spatial distribution and is documented in Section 7.8.1.

754 With $\frac{dJ}{d\Omega}(\theta)$, a map is generated, first by filling in the north-east quadrant of the map. This
 755 quadrant is then reflected twice, vertically then horizontally, to fill the full map. Maps are then
 756 normalized by dividing the discrete 2D integral of the map. The 2D integral was a simple height

757 of bins, Newton's integral:

$$p^2 \cdot \sum_{i,j=0}^{N,M} \frac{dJ}{d\Omega}(\theta_{i,j}, \phi_{i,j}) \quad (7.5)$$

758 These maps are HEALpix maps with NSIDE 16384 and saved in the `.fits` format.

759 Another DM spatial distribution model from Bonnivard (\mathcal{B}) [47] was used for the Glory Duck
760 study. However, to save computational time, limits from \mathcal{GS} were scaled to \mathcal{B} instead of each
761 experiment performing a full study a second time. How these models compare is demonstrated
762 for each dSph in Figure 7.16 and Figure 7.17 Plots of these maps are provided for each source
763 in chapter A Examples of the two most impactful dSphs derived from \mathcal{GS} , Segue1 and Coma
764 Berenices are featured in Figure 7.3

765 7.3.3 Source Selection and Annihilation Channels

766 We use many of the dSphs presented in HAWC's previous dSph DM search [46]. HAWC's
767 sources for Glory Duck include Boötes I, Coma Berenices, Canes Venatici I + II, Draco, Hercules,
768 Leo I, II, + IV, Segue 1, Sextans, and Ursa Major I + II. A full description of all sources used
769 in Glory Duck is found in Table 7.1. Triangulum II was excluded from the Glory Duck analysis
770 because of large uncertainties in its J factor. Ursa Minor was excluded from HAWC's contribution
771 to the combination because the source extension model extended Ursa Minor beyond HAWC's field
772 of view. Ursa Minor was not expected to contribute significantly to the combined limit, so work
773 was not invested in a solution to include Ursa Minor.

774 This analysis improves on the previous HAWC dSph paper [46] in the following ways. Pre-
775 viously, the dSphs were treated and implemented as point sources. For this analysis, dSphs are
776 modeled and treated as extended source. The impact of this change with respect to the upper limit
777 is source dependent and is explored in Section 7.7.2. Previously, the particle physics model used for
778 gamma-ray spectra from DM annihilation did not have EW corrections where the PPPC includes
779 them. Finally, the gamma-ray ray dataset is much larger. The study performed here analyzes over
780 1000 days of data compared to 507.

781 The SM annihilation channels probed for the Glory Duck combination include $b\bar{b}$, $e\bar{e}$, $\mu\bar{\mu}$, $\tau\bar{\tau}$,
782 $t\bar{t}$, W^+W^- , and ZZ . A summary of all sources, with a description of each experiments' sensitivity

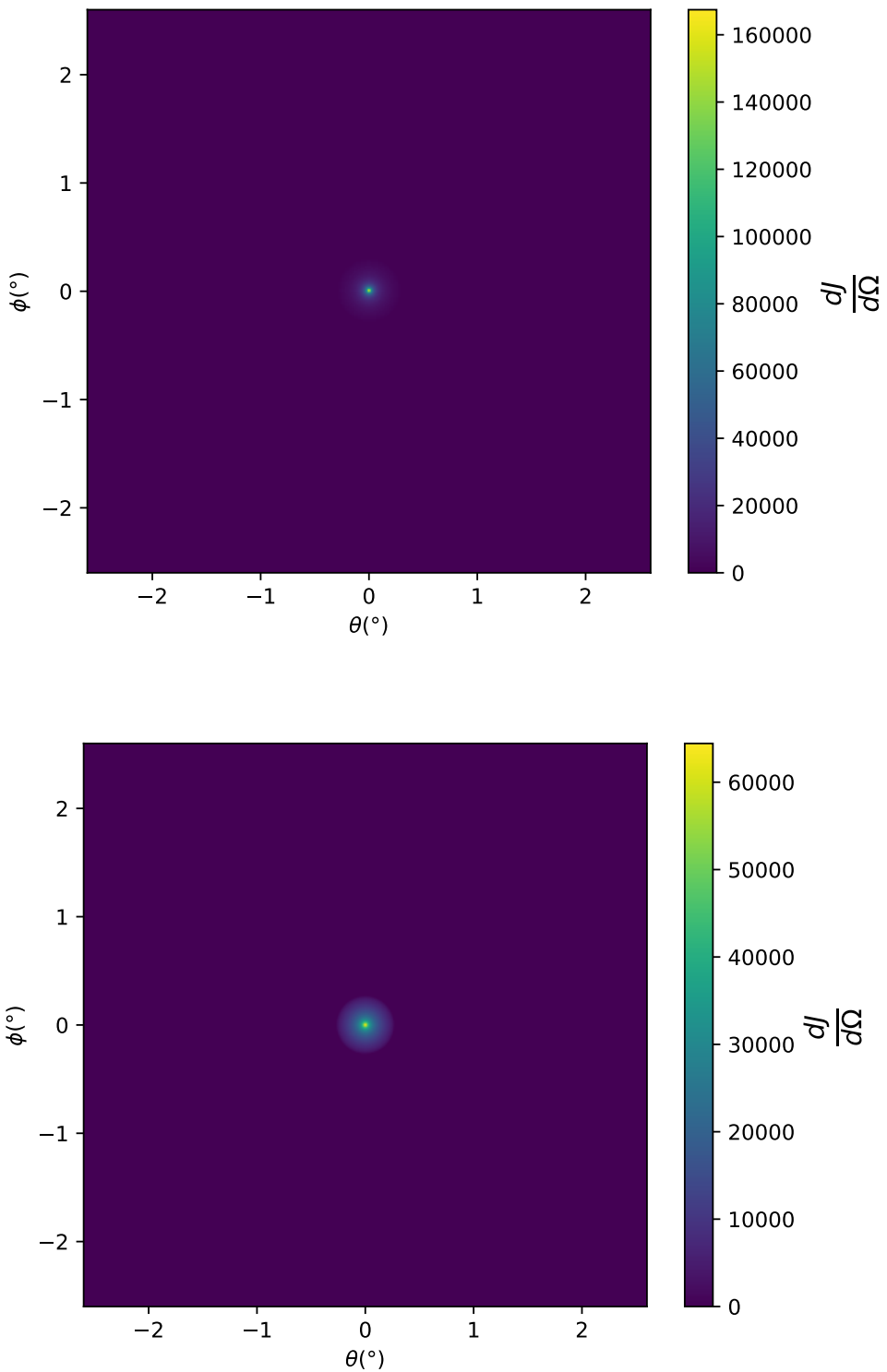


Figure 7.3 $\frac{dJ}{d\Omega}$ maps for Segue1 (top) and Coma Berenices (bottom). Origin is centered on the specific dwarf spheroidal galaxies (dSph). X and Y axes are the angular separation from the center of the dwarf. Plots of the remaining 11 dSph HAWC studied are linked in Fig. A.1.

Table 7.1 Summary of the relevant properties of the dSphs used in the present work. Column 1 lists the dSphs. Columns 2 and 3 present their heliocentric distance and galactic coordinates, respectively. Columns 4 and 5 report the J -factors of each source given from the \mathcal{GS} and \mathcal{B} independent studies and their estimated $\pm 1\sigma$ uncertainties. The values $\log_{10} J$ (\mathcal{GS} set) [45] correspond to the mean J -factor values for a source extension truncated at the outermost observed star. The values $\log_{10} J$ (\mathcal{B} set) [47] are provided for a source extension at the tidal radius of each dSph. **Bolded sources are within HAWC's field of view and provided to the Glory Duck analysis.**

Name	Distance (kpc)	l, b ($^{\circ}$)	$\log_{10} J$ (\mathcal{GS} set) $\log_{10}(\text{GeV}^2 \text{cm}^{-5} \text{sr})$	$\log_{10} J$ (\mathcal{B} set) $\log_{10}(\text{GeV}^2 \text{cm}^{-5} \text{sr})$
Boötes I	66	358.08, 69.62	$18.24^{+0.40}_{-0.37}$	$18.85^{+1.10}_{-0.61}$
Canes Venatici I	218	74.31, 79.82	$17.44^{+0.37}_{-0.28}$	$17.63^{+0.50}_{-0.20}$
Canes Venatici II	160	113.58, 82.70	$17.65^{+0.45}_{-0.43}$	$18.67^{+1.54}_{-0.97}$
Carina	105	260.11, -22.22	$17.92^{+0.19}_{-0.11}$	$18.02^{+0.36}_{-0.15}$
Coma Berenices	44	241.89, 83.61	$19.02^{+0.37}_{-0.41}$	$20.13^{+1.56}_{-1.08}$
Draco	76	86.37, 34.72	$19.05^{+0.22}_{-0.21}$	$19.42^{+0.92}_{-0.47}$
Fornax	147	237.10, -65.65	$17.84^{+0.11}_{-0.06}$	$17.85^{+0.11}_{-0.08}$
Hercules	132	28.73, 36.87	$16.86^{+0.74}_{-0.68}$	$17.70^{+1.08}_{-0.73}$
Leo I	254	225.99, 49.11	$17.84^{+0.20}_{-0.16}$	$17.93^{+0.65}_{-0.25}$
Leo II	233	220.17, 67.23	$17.97^{+0.20}_{-0.18}$	$18.11^{+0.71}_{-0.25}$
Leo IV	154	265.44, 56.51	$16.32^{+1.06}_{-1.70}$	$16.36^{+1.44}_{-1.65}$
Leo V	178	261.86, 58.54	$16.37^{+0.94}_{-0.87}$	$16.30^{+1.33}_{-1.16}$
Leo T	417	214.85, 43.66	$17.11^{+0.44}_{-0.39}$	$17.67^{+1.01}_{-0.56}$
Sculptor	86	287.53, -83.16	$18.57^{+0.07}_{-0.05}$	$18.63^{+0.14}_{-0.08}$
Segue I	23	220.48, 50.43	$19.36^{+0.32}_{-0.35}$	$17.52^{+2.54}_{-2.65}$
Segue II	35	149.43, -38.14	$16.21^{+1.06}_{-0.98}$	$19.50^{+1.82}_{-1.48}$
Sextans	86	243.50, 42.27	$17.92^{+0.35}_{-0.29}$	$18.04^{+0.50}_{-0.28}$
Ursa Major I	97	159.43, 54.41	$17.87^{+0.56}_{-0.33}$	$18.84^{+0.97}_{-0.43}$
Ursa Major II	32	152.46, 37.44	$19.42^{+0.44}_{-0.42}$	$20.60^{+1.46}_{-0.95}$
Ursa Minor	76	104.97, 44.80	$18.95^{+0.26}_{-0.18}$	$19.08^{+0.21}_{-0.13}$

783 to the source, is provided in Table 7.2.

784 7.4 Likelihood Methods

785 7.4.1 HAWC Likelihoods

786 For every analysis bin in energy, f_{hit} bins (1-9), and location, we can expect N signal events and
 787 B background events. The expected number of excess signal events from dark matter annihilation,

Table 7.2 Summary of dSph observations by each experiment used in this work. A ‘-’ indicates the experiment did not observe the dSph for this study. For Fermi-LAT, the exposure at 1 GeV is given. For HAWC, $|\Delta\theta|$ is the absolute difference between the source declination and HAWC latitude. HAWC is more sensitive to sources with smaller $|\Delta\theta|$. For IACTs, we show the zenith angle range, the total exposure, the energy range, the angular radius θ of the signal or ON region, the ratio of exposures between the background-control (OFF) and signal (ON) regions (τ), and the significance of gamma-ray excess in standard deviations, σ .

Source name	Fermi-LAT	HAWC	H.E.S.S, MAGIC, VERITAS						
	Exposure (10^{11} s m 2)	$ \Delta\theta $ (°)	IACT	Zenith (°)	Exposure (h)	Energy range (GeV)	θ (°)	τ	S (σ)
Boötes I	2.6	4.5	VERITAS	15 – 30	14.0	100–41000	0.10	8.6	-1.0
Canes Venatici I	2.9	14.6	–	–	–	–	–	–	–
Canes Venatici II	2.9	15.3	–	–	–	–	–	–	–
Carina	3.1	–	H.E.S.S.	27 – 46	23.7	310 – 70000	0.10	18.0	-0.3
Coma Berenices	2.7	4.9	H.E.S.S.	47 – 49	11.4	550 – 70000	0.10	14.4	-0.4
Draco	3.8	38.1	MAGIC	5 – 37	49.5	60 – 10000	0.17	1.0	–
			MAGIC	29 – 45	52.1	70 – 10000	0.22	1.0	–
			VERITAS	25 – 40	49.8	120 – 70000	0.10	9.0	-1.0
Fornax	2.7	–	H.E.S.S.	11 – 25	6.8	230 – 70000	0.10	45.5	-1.5
Hercules	2.8	6.3	–	–	–	–	–	–	–
Leo I	2.5	6.7	–	–	–	–	–	–	–
Leo II	2.6	3.1	–	–	–	–	–	–	–
Leo IV	2.4	19.5	–	–	–	–	–	–	–
Leo V	2.4	–	–	–	–	–	–	–	–
Leo T	2.6	–	–	–	–	–	–	–	–
Sculptor	2.7	–	H.E.S.S.	10 – 46	11.8	200 – 70000	0.10	19.8	-2.2
Segue I	2.5	2.9	MAGIC	13 – 37	158.0	60 – 10000	0.12	1.0	-0.5
			VERITAS	15 – 35	92.0	80 – 50000	0.10	7.6	0.7
Segue II	2.7	–	–	–	–	–	–	–	–
Sextans	2.4	20.6	–	–	–	–	–	–	–
Ursa Major I	3.4	32.9	–	–	–	–	–	–	–
Ursa Major II	4.0	44.1	MAGIC	35 – 45	94.8	120 – 10000	0.30	1.0	-2.1
Ursa Minor	4.1	–	VERITAS	35 – 45	60.4	160 – 93000	0.10	8.4	-0.1

788 S , is estimated by convolving Equation (7.1) with HAWC's energy response and pixel point spread
 790 functions. I then compute the test statistic (TS) with the log-likelihood ratio test,

$$\text{TS} = -2 \ln \left(\frac{\mathcal{L}_0}{\mathcal{L}^{\max}} \right) \quad (7.6)$$

791 where \mathcal{L}_0 is the null hypothesis, or no DM emission, likelihood. \mathcal{L}^{\max} is the best fit signal
 792 hypothesis where $\langle \sigma v \rangle$ maximizes the likelihood. We calculate the likelihood of each source and
 793 model, assuming events are Poisson distributed, with

$$\mathcal{L} = \prod_i \frac{(B_i + S_i)^{N_i} e^{-(B_i + S_i)}}{N_i!} \quad (7.7)$$

794 where S_i is the sum of expected number of signal counts. B_i is the number of background counts
 795 observed. N_i is the total number of counts.

796 I also calculate an upper limit on $\langle \sigma v \rangle$ by calculating the 95% confidence level (CL). For the
 797 CL, we define a parameter, TS_{95} , as

$$\text{TS}_{95} \equiv \sum_{\text{bins}} \left[2N \ln \left(1 + \frac{\epsilon S_{\text{ref}}}{B} \right) - 2\epsilon S_{\text{ref}} \right] \quad (7.8)$$

798 where the expected signal counts from a dSph is scaled by ϵ . S_{ref} is the expected number of excess
 799 counts in a bin from DM emission from a dSph with a corresponding annihilation cross-section,
 800 $\langle \sigma v \rangle$. We scan ϵ such that

$$2.71 = \text{TS}_{\max} - \text{TS}_{95} \quad (7.9)$$

801 7.4.2 Glory Duck Joint Likelihood

802 The joint likelihood for the 5-experiment combination was done similarly as Section 7.4.1. We
 803 calculate upper limits on $\langle \sigma v \rangle$ from the TS, Eq. (7.6), and define the likelihood ratio more generally

$$\lambda(\langle \sigma v \rangle | \mathcal{D}_{\text{dSphs}}) = \frac{\mathcal{L}(\langle \sigma v \rangle; \hat{\nu} | \mathcal{D}_{\text{dSphs}})}{\mathcal{L}(\widehat{\langle \sigma v \rangle}; \hat{\nu} | \mathcal{D}_{\text{dSphs}})} \quad (7.10)$$

804 $\mathcal{D}_{\text{dSphs}}$ is the totality of observations across experiments and dSphs. ν are the nuisance parameters
 805 which are the J factors in this study. $\widehat{\langle \sigma v \rangle}$ and $\hat{\nu}$ are the respective estimate that maximize \mathcal{L}
 806 globally. Finally, $\hat{\nu}$ is the set of nuisance parameters that maximize \mathcal{L} for a fixed value of $\langle \sigma v \rangle$.

807 The *complete* joint likelihood, \mathcal{L} that encompasses all observations from all instruments and
 808 dSphs can be factorized into *partial* functions for each dSph l (with $\mathcal{L}_{\text{dSph},l}$) and its J factor (\mathcal{J}_l):

$$\mathcal{L}(\langle\sigma v\rangle; \nu | \mathcal{D}_{\text{dSphs}}) = \prod_{l=1}^{N_{\text{dSphs}}} \mathcal{L}_{\text{dSph},l}(\langle\sigma v\rangle; J_l, \nu_l | \mathcal{D}_l) \times \mathcal{J}_l(J_l | J_{l,\text{obs}}, \sigma_{\log J_l}). \quad (7.11)$$

809 For this study, $N_{\text{dSphs}} = 20$ is the number of dSphs studied. \mathcal{D}_l are the gamma-ray observations
 810 of dSph, l . ν_l are the nuisance parameters modifying the gamma-ray observations of dSph, l ,
 811 but excludes \mathcal{J}_l . \mathcal{J}_l is the J factor for dSph, l , as defined in Equation (7.2), and it is a nuisance
 812 parameter whose value is unknown. $\log_{10} J_{l,\text{obs}}$ and $\sigma_{\log J_l}$ are obtained from fitting a log-normal
 813 function of $J_{l,\text{obs}}$ to the posterior distribution of J_l [48]. $\log_{10} J_{l,\text{obs}}$ and $\sigma_{\log J_l}$ values are provided
 814 in Table 7.1. The term \mathcal{J}_l constraining J_l is written as:

$$\mathcal{J}_l(J_l | J_{l,\text{obs}}, \sigma_{\log J_l}) = \frac{1}{\ln(10)J_{l,\text{obs}}\sqrt{2\pi}\sigma_{\log J_l}} \exp\left(-\frac{(\log_{10} J_l - \log_{10} J_{l,\text{obs}})^2}{2\sigma_{\log J_l}^2}\right). \quad (7.12)$$

815 Both the \mathcal{GS} and \mathcal{B} , displayed in Table 7.1, sets of J factors are used in this analysis. Equation (7.12)
 816 is also normalized, so it can also be interpreted as a probability density function (PDF) for $J_{l,\text{obs}}$.
 817 From Equation (7.1), we can also see that $\langle\sigma v\rangle$ and J_l are degenerate when computing $\mathcal{L}_{\text{dSph},l}$.
 818 Therefore, as noted in [49], it is sufficient to compute $\mathcal{L}_{\text{dSph},l}$ versus $\langle\sigma v\rangle$ for a fixed value of J_l .
 819 We used $J_{l,\text{obs}}(\mathcal{GS})$ reported in Tab. 7.1, in order to perform the profile of \mathcal{L} with respect to J_l .
 820 The degeneracy implies that for any $J'_l \neq J_{l,\text{obs}}$ (in practice in our case we used $J'_l = J_{l,\text{obs}}(\mathcal{B})$ to
 821 compute results from a different set of J factors):

$$\mathcal{L}_{\text{dSph},l}(\langle\sigma v\rangle; J'_l, \nu_l | \mathcal{D}_l) = \mathcal{L}_{\text{dSph},l}\left(\frac{J'_l}{J_{l,\text{obs}}}\langle\sigma v\rangle; J_{l,\text{obs}}, \nu_l | \mathcal{D}_l\right), \quad (7.13)$$

822 which is a straightforward rescaling operation that reduces the computational needs of the profiling
 823 operation since:

$$\mathcal{L}(\langle\sigma v\rangle; \hat{\nu} | \mathcal{D}_{\text{dSphs}}) = \prod_{l=1}^{N_{\text{dSphs}}} \max_{J_l} \left[\mathcal{L}_{\text{dSph},l}(\langle\sigma v\rangle; J_l, \hat{\nu}_l | \mathcal{D}_l) \times \mathcal{J}_l(J_l | J_{l,\text{obs}}, \sigma_{\log J_l}) \right]. \quad (7.14)$$

824 In addition, Eq. (7.13) enables the combination of data from different gamma-ray instruments and
 825 observed dSphs via tabulated values of $\mathcal{L}_{\text{dSph},l}$, or equivalently of λ from Eq. (7.10) as was done in

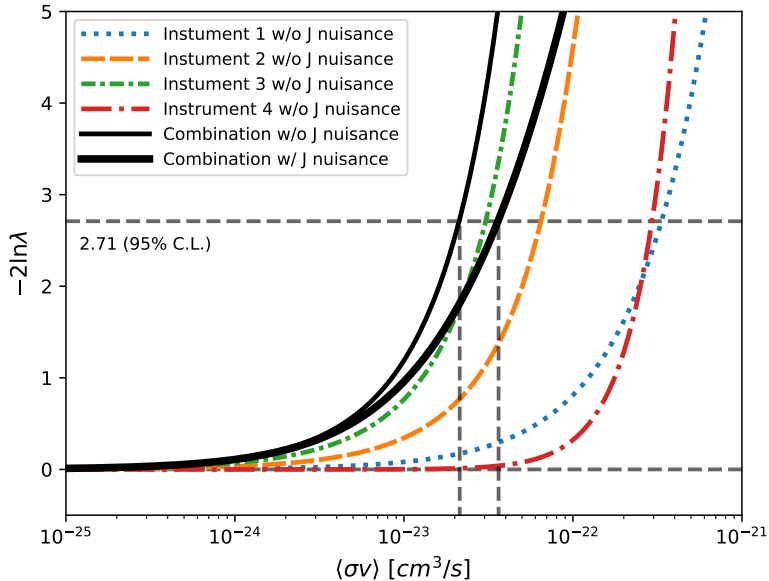


Figure 7.4 Illustration of the combination technique showing a comparison between $-2 \ln \lambda$ provided by four instruments (colored lines) from the observation of the same dSph without any J nuisance and their sum, *i.e.* the resulting combined likelihood (thin black line). According to the test statistics of Equation (7.6), the intersection of the likelihood profiles with the line $-2 \ln \lambda = 2.71$ indicates the 95% C.L. upper limit on $\langle\sigma v\rangle$. The combined likelihood (thin black line) shows a smaller value of upper limit on $\langle\sigma v\rangle$ than those derived by individual instruments. We also show how the uncertainties on the J factor effects the combined likelihood and degrade the upper limit on $\langle\sigma v\rangle$ (thick black line). All likelihood profiles are normalized so that the global minimum $\widehat{\langle\sigma v\rangle}$ is 0. We note that each profile depends on the observational conditions in which a target object was observed. The sensitivity of a given instrument can be degraded and the upper limits less constraining if the observations are performed in non-optimal conditions such as a high zenith angle or a short exposure time.

826 this work, versus $\langle\sigma v\rangle$. $\mathcal{L}_{dSph,l}$ is computed for a fixed value of J_l and profiled with respect to all
 827 instrumental nuisance parameters ν_l , these nuisance parameters are discussed in more detail below.
 828 These values are produced by each detector independently and therefore there is no need to share
 829 sensitive low-level information used to produce them, such as event lists. Figure 7.4 illustrates the
 830 multi-instrument combination technique used in this study with a comparison of the upper limit
 831 on $\langle\sigma v\rangle$ obtained from the combination of the observations of four experiments towards one dSph
 832 versus the upper limit from individual instruments. It also shows graphically the effect of the
 833 J -factor uncertainty on the combined observations.

834 The *partial* joint likelihood function for gamma-ray observations of each dSph ($\mathcal{L}_{dSph,l}$) is

written as the product of the likelihood terms describing the $N_{\text{exp},l}$ observations performed with any of our observatories:

$$\mathcal{L}_{\text{dSph},l} (\langle \sigma v \rangle; J_l, \nu_l | \mathcal{D}_l) = \prod_{k=1}^{N_{\text{exp},l}} \mathcal{L}_{lk} (\langle \sigma v \rangle; J_l, \nu_{lk} | \mathcal{D}_{lk}), \quad (7.15)$$

where each \mathcal{L}_{lk} term refers to an observation of the l -th dSph with associated k -th instrument responses. $N_{\text{exp},l}$ varies from dSph to dSph and can be inferred from Table 7.2.

Each collaboration separately analyzes their data for \mathcal{D}_{lk} corresponding to dSph l and gamma-ray detector k , using as many common assumptions as possible in the analysis. HAWC's treatment was described earlier in Section 7.4.1 whereas the specifics of the remaining experiments is left to the publication. We compute the values for the likelihood functions \mathcal{L}_{lk} (see Eq. (7.15)) for a fixed value of J_l and profile over the rest of the nuisance parameters ν_{lk} . Then, values of λ from Eq. (7.10) are computed as a function of $\langle \sigma v \rangle$, and shared using a common format. Results are computed for seven annihilation channels, W^+W^- , ZZ , $b\bar{b}$, $t\bar{t}$, e^+e^- , $\mu^+\mu^-$, and $\tau^+\tau^-$ over 62 m_χ values between 5 GeV and 100 TeV provided in [44]. The $\langle \sigma v \rangle$ range is defined between 10^{-28} and $10^{-18} \text{cm}^3 \cdot \text{s}^{-1}$, with 1001 logarithmically spaced values. The likelihood combination, i.e. Equation (7.11), and profile over the J -factor to compute the profile likelihood ratio λ , Equation (7.10), are carried out with two different public analysis software packages, namely `gLike` [50] and `LklCom` [51], that provide the same results [52].

As mentioned previously, each experiment computes the \mathcal{L}_{lk} from Equation (7.10) differently. The remainder of this section highlights the differences in this calculation across the experiments. Four experiments, namely *Fermi*-LAT, H.E.S.S., HAWC and MAGIC, use a binned likelihood to compute the \mathcal{L}_{lk} . For these experiments, for each observation \mathcal{D}_{lk} of a given dSph l carried out using a given gamma-ray detector k , the binned likelihood function is:

$$\mathcal{L}_{lk} (\langle \sigma v \rangle; J_l, \nu_{lk} | \mathcal{D}_{lk}) = \prod_{i=1}^{N_E} \prod_{j=1}^{N_P} \left[\mathcal{P}(s_{lk,ij}(\langle \sigma v \rangle, J_l, \nu_{lk}) + b_{lk,ij}(\nu_{lk}) | N_{lk,ij}) \right] \times \mathcal{L}_{lk,\nu} (\nu_{lk} | \mathcal{D}_{\nu_{lk}}) \quad (7.16)$$

where N_E and N_P are the number of considered bins in reconstructed energy and arrival direction, respectively; \mathcal{P} represents a Poisson PDF for the number of gamma-ray candidate events $N_{lk,ij}$

858 observed in the i -th bin in energy and j -th bin in arrival direction, when the expected number is
 859 the sum of the expected mean number of signal events s_{ij} (produced by DM annihilation) and of
 860 background events b_{ij} ; $\mathcal{L}_{lk,\nu}$ is the likelihood term for the extra ν_{lk} nuisance parameters that vary
 861 from one instrument k to another. The expected counts for signal events s_{ij} for a given dSph l and
 862 detector k is given by:

$$s_{ij}(\langle\sigma\nu\rangle, J) = \int_{E'_{\min,i}}^{E'_{\max,i}} dE' \int_{P'_{\min,j}}^{P'_{\max,j}} d\Omega' \int_0^\infty dE \int_{\Delta\Omega_{tot}} d\Omega \int_0^{T_{\text{obs}}} dt \frac{d^2\Phi(\langle\sigma\nu\rangle, J)}{dEd\Omega} \text{IRF}(E', P' | E, P, t) \quad (7.17)$$

863 where E' and E are the reconstructed and true energies, P' and P the reconstructed and true
 864 arrival directions; $E'_{\min,i}$, $P'_{\min,j}$, $E'_{\max,i}$, and $P'_{\max,j}$ are their lower and upper limits of the i -th
 865 energy bin and the j -th arrival direction bin; T_{obs} is the (dead-time corrected) total observation
 866 time; t is the time along the observations; $d^2\Phi/dEd\Omega$ is the DM flux in the source region (see
 867 Equation (7.1)); and $\text{IRF}(E', P' | E, P, t)$ is the IRF, which can be factorized as the product of the
 868 effective collection area of the detector $A_{\text{eff}}(E, P, t)$, the PDFs for the energy estimator $f_E(E' | E, t)$,
 869 and arrival direction $f_P(P' | E, P, t)$ estimators. Note that for Fermi-LAT, HAWC, MAGIC, and
 870 VERITAS the effect of the finite angular resolution is taken into account through the convolution
 871 of $d\Phi/dEd\Omega$ with f_P in Equation (7.17), whereas in the cases of H.E.S.S. f_P is approximated by a
 872 delta function. This approximation has been made in order to maintain compatibility of the result
 873 with what has been previously published. The difference introduced by this approximation is $< 5\%$
 874 for all considered dSphs. A more comprehensive review of the differences between the analyses of
 875 different instruments can be found in [25].

876 7.5 HAWC Results

877 13 of the 20 dSphs considered for the Glory Duck analysis are within HAWC's field of view.
 878 These dSph are analyzed for emission from DM annihilation according to the likelihood method
 879 described in Section 7.4. The 13 likelihood profiles are then stacked to synthesize a combined
 880 limit on the dark matter cross-section, $\langle\sigma\nu\rangle$. This combination is done for the 7 SM annihilation
 881 channels used in the Glory Duck analysis. Figure 7.5 shows the combined limit for all annihilation
 882 channels with HAWC only observations. We also perform 300 studies of Poisson trials on the

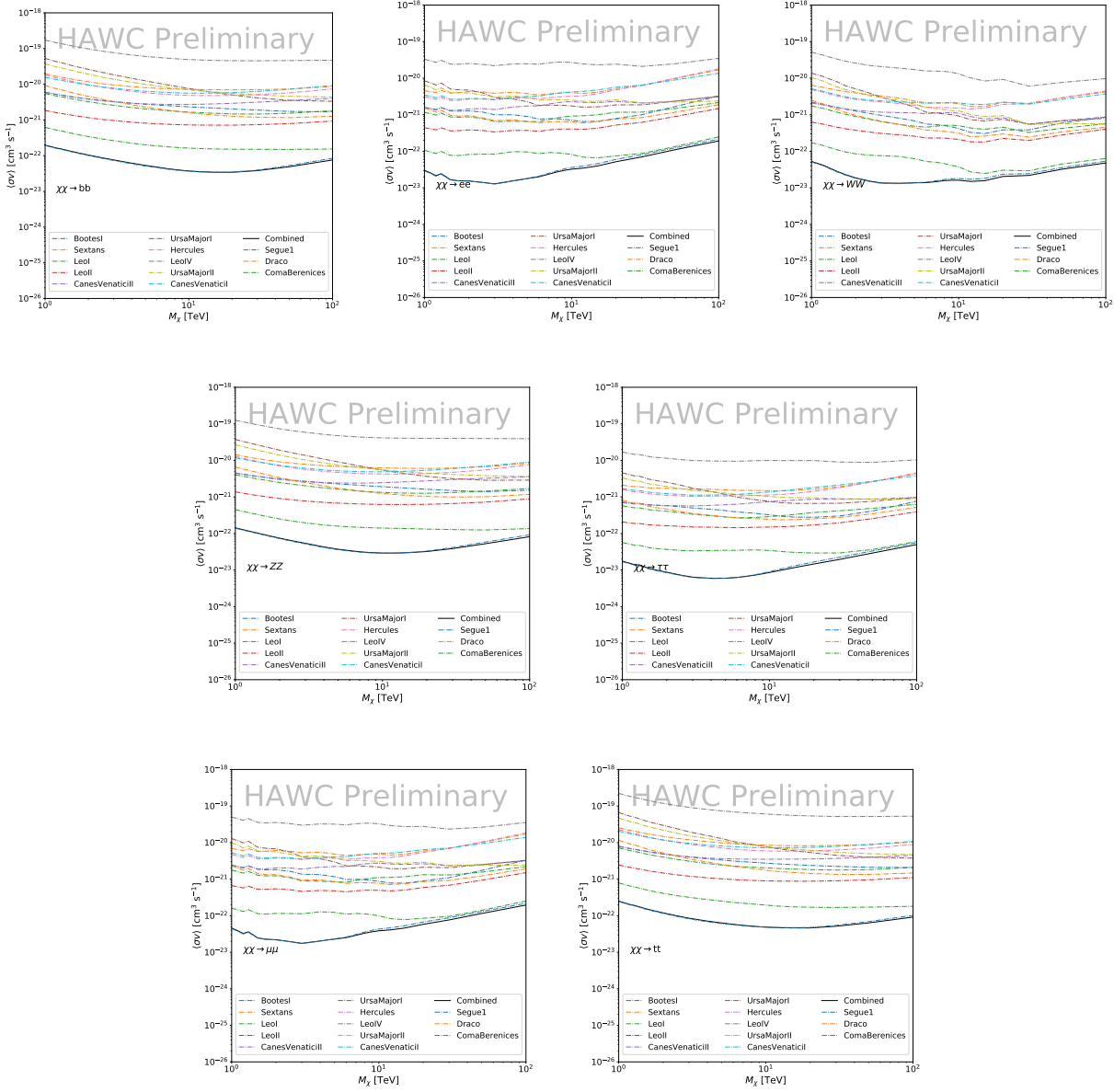


Figure 7.5 HAWC upper limits at 95% confidence level on $\langle\sigma v\rangle$ versus DM mass for seven annihilation channels, using the set of J -factors from Ref. [53]. The solid line represents the observed combined limit. Dashed lines represent limits from individual dSphs.

background. These trials are used to produce HAWC Brazil bands which were shared with the other collaborators for combined Brazil Bands. The results on fitting to HAWC's Poisson trials of the DM hypothesis is shown in Figure 7.7 for all the DM annihilation channels studied for Glory Duck.

No DM was found in HAWC observations. HAWC's limits are dominated by the dSphs Segue1

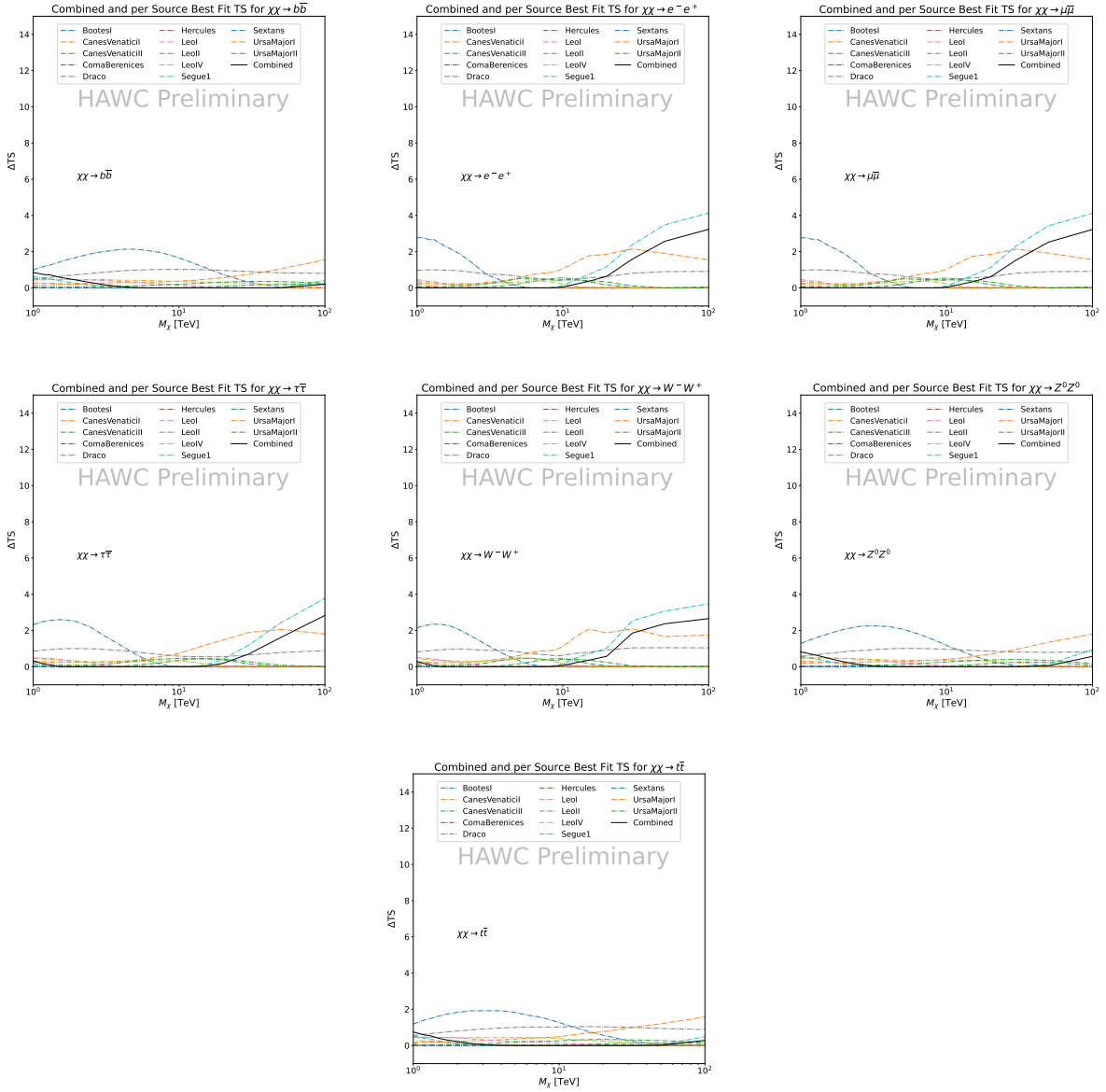


Figure 7.6 HAWC TS values for best fit $\langle \sigma v \rangle$ versus m_χ for seven SM annihilation channels with J factors from \mathcal{GS} . The solid black line shows the combined best fit TS values. The colored, dashed lines are the TS values for each of the 13 sources HAWC studied.

and Coma Berenices. The remaining 11 dSphs do not contribute significantly to the limit because they are at high zenith and/or have much smaller J factors. Even though some remaining dSphs have large J factors, they are towards the edge of HAWC's field of view where HAWC analysis is less sensitive.

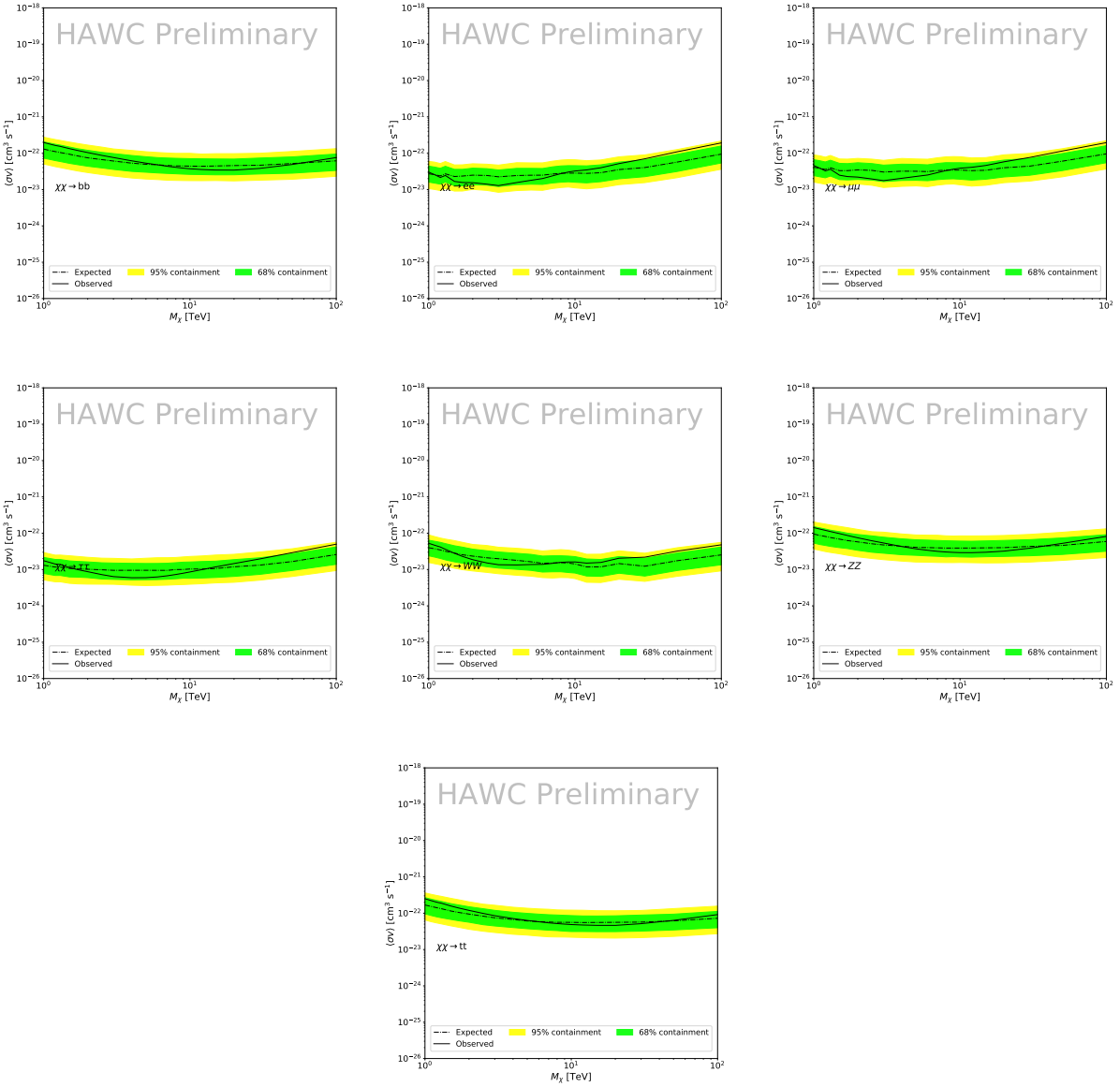


Figure 7.7 HAWC Brazil bands at 95% confidence level on $\langle\sigma v\rangle$ versus DM mass for seven annihilation channels with J -factors from \mathcal{GS} [53]. The solid line represents the combined limit from 13 dSphs. The dashed line is the expected limit. The green band is the 68% containment. The yellow band is the 95% containment.

892 7.6 Glory Duck Combined Results

893 The crux of this analysis is that HAWC's results are combined with 4 other gamma-ray observa-
 894 tories: Fermi-LAT, H.E.S.S., MAGIC, and VERITAS. No significant DM emission was observed
 895 by any of the five instruments. We present the upper limits on $\langle\sigma v\rangle$ assuming seven independent
 896 DM self annihilation channels, namely W^+W^- , Z^+Z^- , $b\bar{b}$, $t\bar{t}$, e^+e^- , $\mu^+\mu^-$, and $\tau^+\tau^-$. The 68%

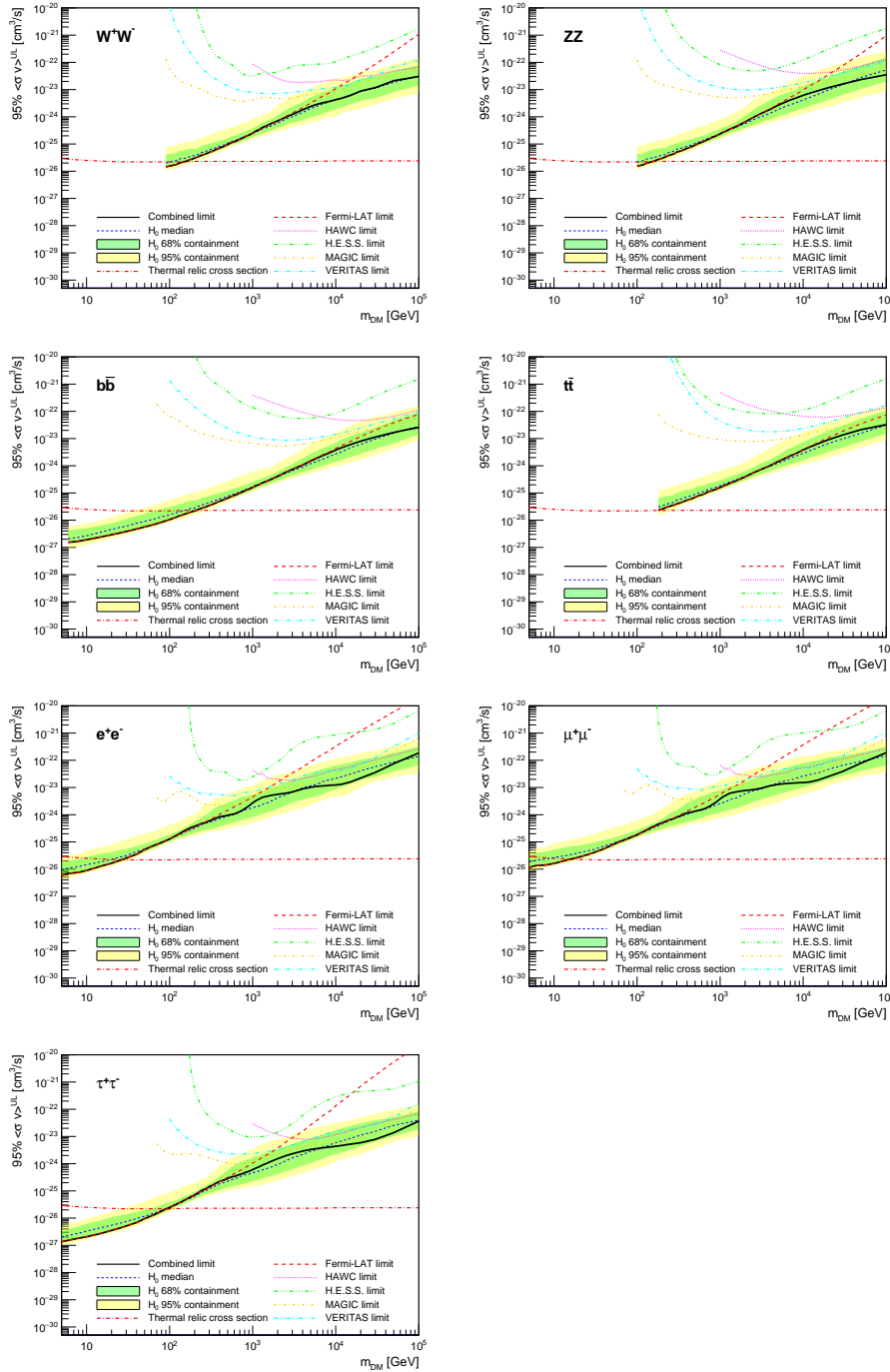


Figure 7.8 Upper limits at 95% confidence level on $\langle\sigma v\rangle$ in function of the DM mass for eight annihilation channels, using the set of J factors from Ref. [53] (\mathcal{GS} set in Table 7.1). The black solid line represents the observed combined limit, the black dashed line is the median of the null hypothesis corresponding to the expected limit, while the green and yellow bands show the 68% and 95% containment bands. Combined upper limits for each individual detector are also indicated as solid, colored lines. The value of the thermal relic cross-section in function of the DM mass is given as the red dotted-dashed line [54].

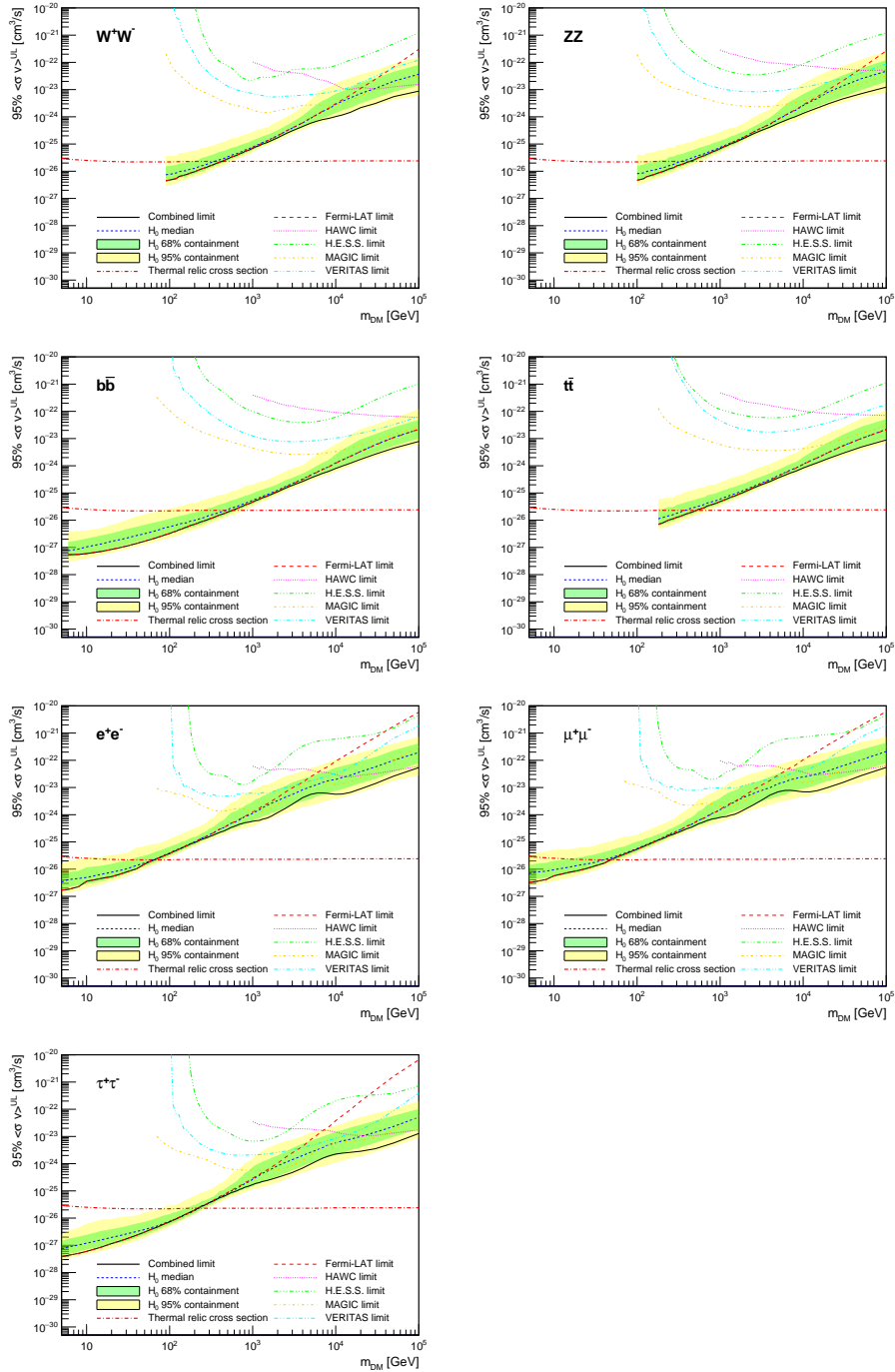


Figure 7.9 Same as Fig. 7.8, using the set of J factors from Ref. [47, 55] (\mathcal{B} set in Table 7.1).

and 95% containment bands are produced from 300 Poisson realizations of the null hypothesis corresponding to each of the combined datasets. These 300 realizations are combined identically to dSph observations. The containment bands and the median are extracted from the distribution of resulting limits on the null hypothesis. These 300 realizations are obtained either by fast simu-

901 lations of the OFF observations, for H.E.S.S., MAGIC, VERITAS, and HAWC, or taken from real
902 observations of empty fields of view in the case of Fermi-LAT [48, 56, 57].

903 The obtained limits are shown in Figure 7.8 for the $\mathcal{G}\mathcal{S}$ set of J -factors [53] and in Figure 7.9
904 for the \mathcal{B} set of J -factors [47, 55]. The combined limits are presented with their 68% and 95%
905 containment bands, and are expected to be close to the median limit when no signal is present.
906 We observe agreement with the null hypothesis for all channels, within 2σ standard deviations,
907 between the observed limits and the expectations given by the median limits. Limits obtained from
908 each detector are also indicated in the figures, where limits for all dSphs observed by the specific
909 instrument have been combined.

910 Below ~ 300 GeV, the *Fermi*-LAT dominates the DM limits for all annihilation channels. From
911 ~ 300 GeV to ~ 2 TeV, *Fermi*-LAT continues to dominate for the hadronic and bosonic DM channels,
912 yet the IACTs (H.E.S.S., MAGIC, and VERITAS) and *Fermi*-LAT all contribute to the limit for
913 leptonic DM channels. For DM masses between ~ 2 TeV to ~ 10 TeV, the IACTs dominate leptonic
914 DM annihilation channels, whereas both the *Fermi*-LAT and the IACTs dominate bosonic and
915 hadronic DM annihilation channels. From ~ 10 TeV to ~ 100 TeV, both the IACTs and HAWC
916 contribute significantly to the leptonic DM limit. For hadronic and bosonic DM, the IACTs and
917 *Fermi*-LAT both contribute strongly.

918 We notice that the limits computed using the \mathcal{B} set of J -factor are always better compared to the
919 ones calculated with the $\mathcal{G}\mathcal{S}$ set. For the W^+W^- , Z^+Z^- , $b\bar{b}$, and $t\bar{t}$ channels, the ratio between the
920 limits computed with the two sets of J -factor is varying between a factor of ~ 3 and ~ 5 depending
921 on the energy, with the largest ratio around 10 TeV. For the channels e^+e^- , $\mu^+\mu^-$, and $\tau^+\tau^-$, the
922 ratio lies between ~ 2 to ~ 6 , being maximum around 1 TeV. Examining Figure 7.16 and Figure 7.17
923 in Section 7.8, these differences are explained by the fact that the \mathcal{B} set provides higher J -factors
924 for the majority of the studied dSphs, with the notable exception of Segue I. The variation on the
925 ratio of the limits for the two sets is due to different dSph dominating the limits depending on the
926 energy. This pushes the range of thermal cross-section which can be excluded to higher mass. This
927 comparison demonstrates the magnitude of systematic uncertainties associated with the choice of

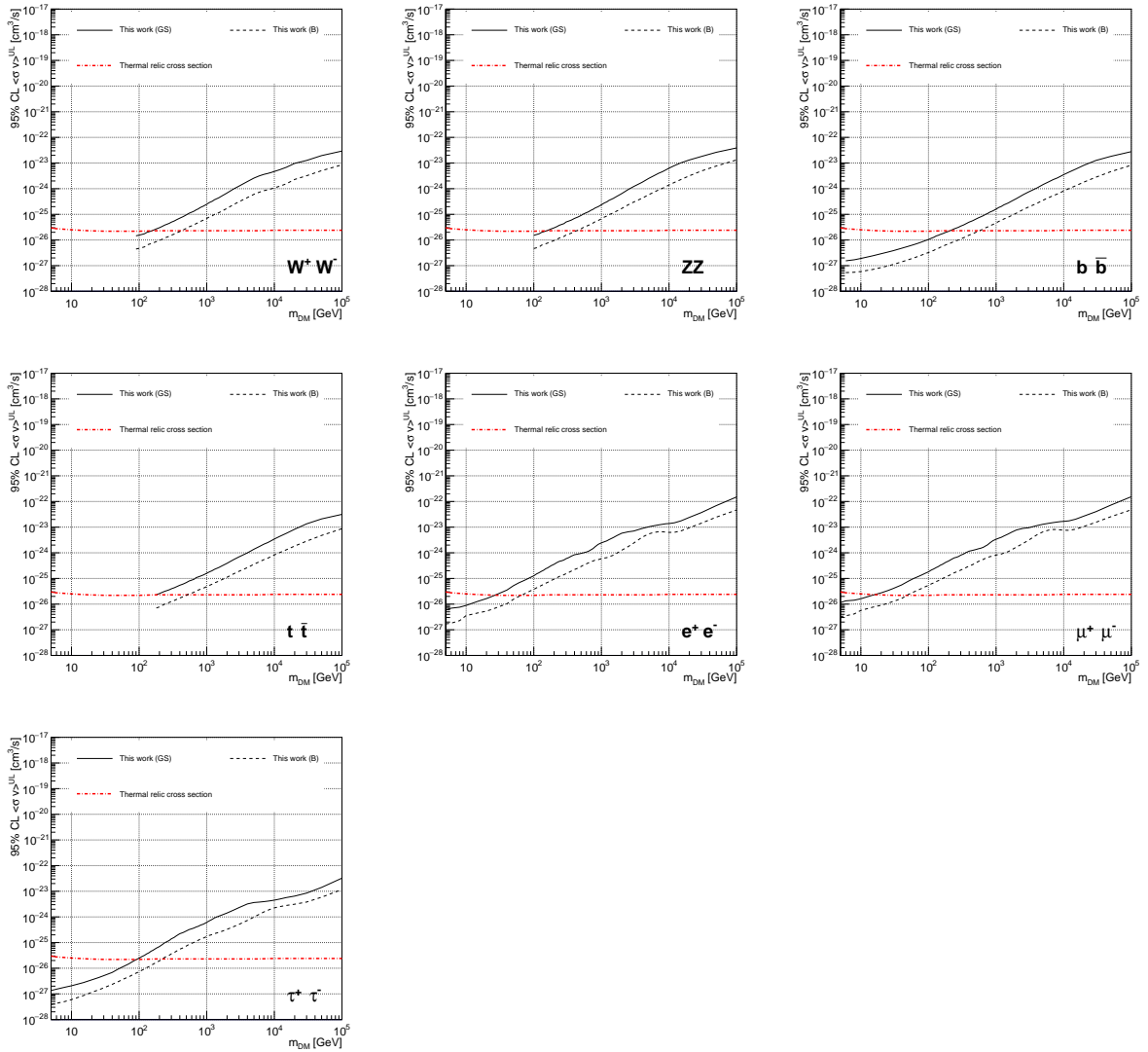


Figure 7.10 Comparisons of the combined limits at 95% confidence level for each of the eight annihilation channels when using the J factors from Ref. [53] (\mathcal{GS} set in Table 7.1), plain lines, and the J factor from Ref. [47, 55] (\mathcal{B} set in Table 7.1), dashed lines. The cross-section given by the thermal relic is also indicated [54].

928 the J -factor

929 This comparison demonstrates the magnitude of systematic uncertainties associated with the
930 choice of the J -factor calculation. The \mathcal{GS} and \mathcal{B} sets present a difference in the limits for all
931 channels of about This difference is explained, see Figure 7.16 and Figure 7.17 in Appendix, by the
932 fact that the \mathcal{B} set provides higher J factors for all dSph except for Segue I. This pushes the range
933 of thermal cross-section which can be excluded to higher mass.

934 **7.7 HAWC Systematics**

935 **7.7.1 Inverse Compton Scattering**

936 The DM-DM annihilation channels produce many high energy electrons regardless of the
937 primary annihilation channel. These high energy electrons can produce high energy gamma-rays
938 through Inverse Compton Scattering (ICS). If this effect is strong, it would change the morphology
939 of the source and increase the total expected gamma-ray counts from any source. The PPPC [44]
940 provides tools in Mathematica for calculating the impact of ICS for an arbitrary location in the
941 sky for a specified annihilation channel. We calculated the change in gamma-ray counts for DM
942 annihilation to primary $e\bar{e}$ for RA and Dec corresponding to Segue1 and Coma Berenices. These
943 dSphs were chosen because they are the strongest contributors to the limit. $e\bar{e}$ was selected because
944 it would have the largest number of high energy electrons. The effect was found to be on the order
945 of 10^{-7} on the gamma-ray spectrum. As a result, this systematic is not considered in our analysis.

946 **7.7.2 Point Source Versus Extended Source Limits**

947 The previous DM search toward dSph approximated the dSphs as point sources [46]. In
948 this analysis, the dSphs are implemented as extended with J-factor distributions following those
949 produced by [53]. The resolution of the cited map is much finer than HAWC's angular resolution.
950 The vast majority of the J-factor distribution is represented on the central HAWC pixel of the dSph
951 spatial map. However, the neighboring 8 pixels are not negligible and contribute to our limit.

952 Figure 7.11 shows a substantial improvement to the limit for Segue1. Fig. 7.12 however showed
953 identical limits. These disparities are best explained by the relative difference in their J-Factors.
954 Both dSphs pass almost overhead the HAWC detector, however Segue1 has the larger J-Factor
955 between the two. Adjacent pixels to the central pixel will therefore contribute to the limits. This is
956 the case for other dSph that are closer to overhead the HAWC detector.

957 Comparison plots for all sources and the combined limit can be found in the sandbox for the
958 Glory Duck project.

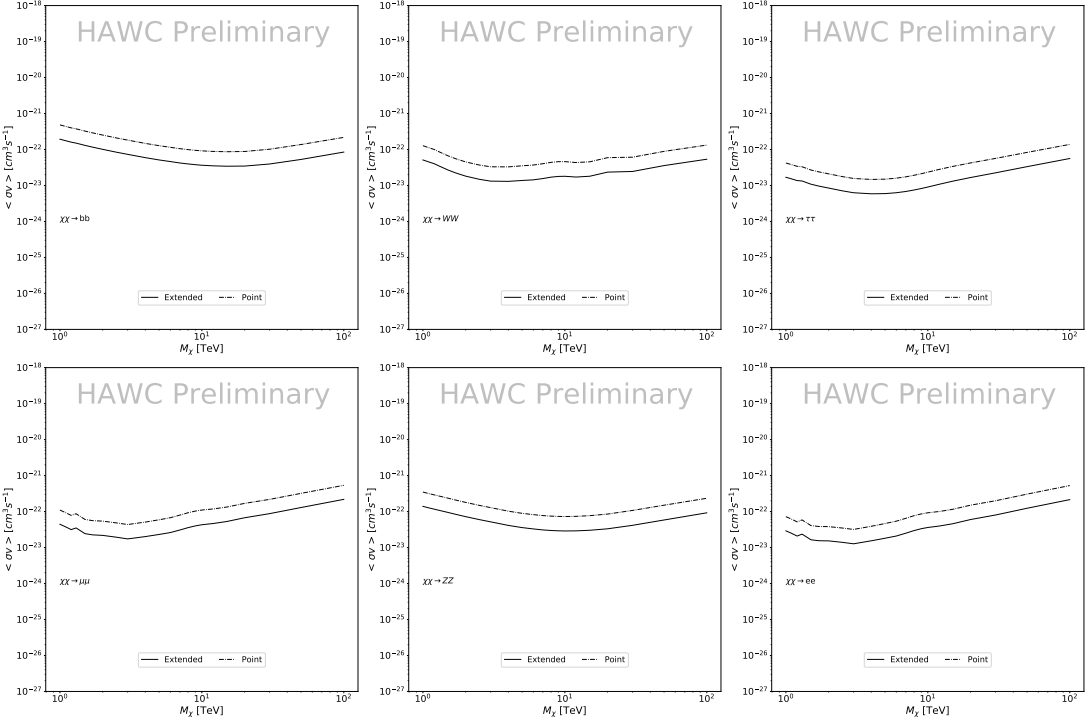


Figure 7.11 Comparisons of the combined limits at 95% confidence level for a point source analysis and extended source using [53] \mathcal{GS} J-factor distributions and PPPC [44] annihilation spectra. Shown are the limits for Segue1 which will have the most significant impact on the combined limit. 6 of the 7 DM annihilation channels are shown. Solid lines are extended source studies. Dashed lines are point source studies. Overall, the extended source analysis improves the limit by a factor of 2.

959 7.7.3 Impact of Pointing Systematic

960 During the analysis it was discovered that reconstruction of gamma-rays. Slides describing this
 961 systematic can be found [here](#). Shown on the presentation is dependence on the pointing systematic
 962 on declination. New spatial profiles were generated for every dSph and limits were computed for
 963 the adjusted declination.

964 Section 7.7.3 demonstrates the impact of this systematic for all DM annihilation channels
 965 studied by HAWC. The impact is a tiny improvement, yet mostly identical, to the combined limits.

966 7.8 J-factor distributions

967 7.8.1 Numerical integration of \mathcal{GS} maps

968 It was discovered well after the HAWC analysis was completed that the published tables from
 969 \mathcal{GS} [45] quoted median J-factors were computed in a non-trivial manner. The assumption myself

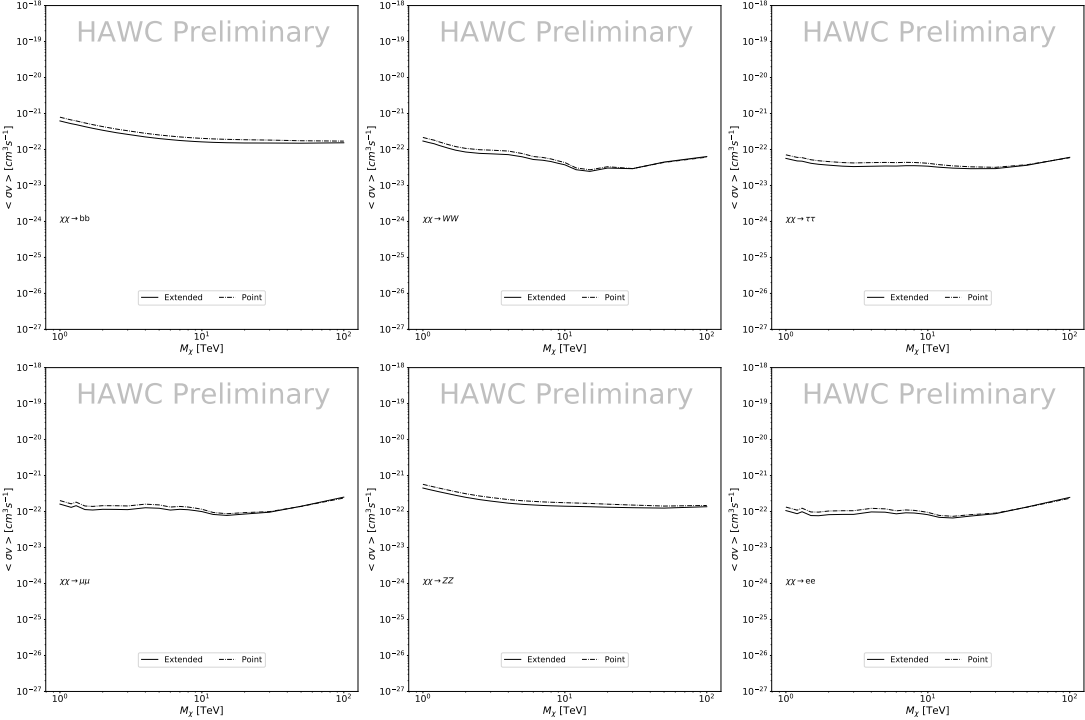


Figure 7.12 Same as Fig. 7.11 on Coma Berenices. This dSph also contributes significantly to the limit. The limits are identical in this case.

and collaborators had been that the published tables represented the J -factor as a function of θ for the best global fit model on a per-source basis. However, this is not the case. Instead, what is published are the best fit model for each dwarf that only considers stars up to the angular separation θ . Therefore, the model is changing for each value of θ for each dwarf. Yet, the introduced features from unique models at each θ are much smaller than the angular resolution of HAWC. It is not expected for these effects to impact the limits and TS greatly as a result.

Median J -factor model profiles were provided by the authors. New maps were generated and analyzed for Segue1 and Coma Berenices. Figure 7.14 shows the differential between maps generated with the method from Section 7.8.1 and from the authors of [45]. These maps were reanalyzed for all SM DM annihilation channels. Upper limits for these channels are shown in Figure 7.15

From Figure 7.15, we can see that the impact of these model difference was no substantial. The observed impact was a fractional effect which is much smaller than the impact from selecting another DM spatial distribution model as was shown in Figure 7.10.

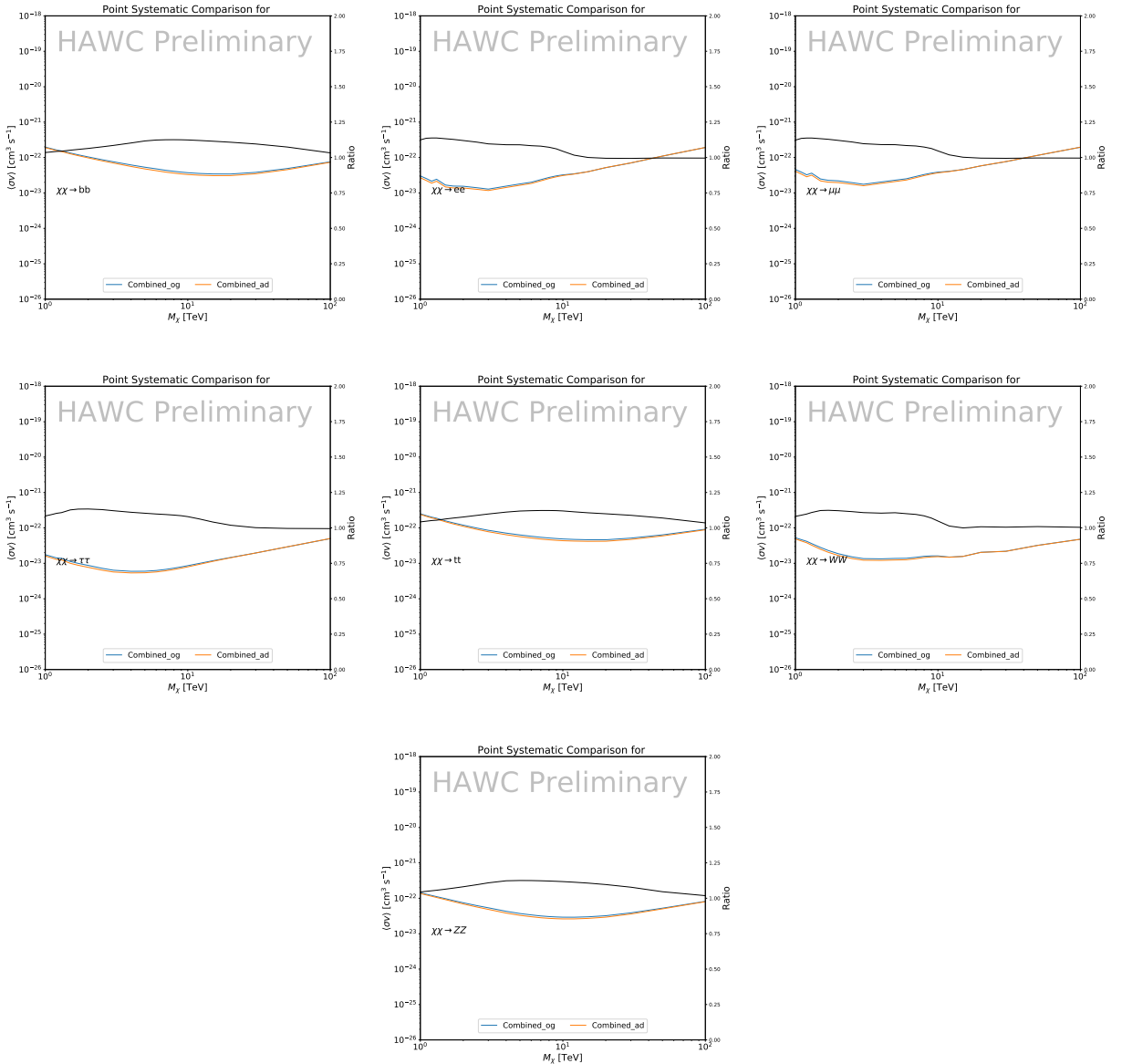


Figure 7.13 Comparison of combined limits when correcting for HAWC's pointing systematic. All DM annihilation channels are shown. The solid black line is the ratio between published limit to the declination corrected limit. The blue solid line or "Combined_og" represented the limits computed for Glory Duck. The solid orange line or "Combined_ad" represented the limits computed after correcting for the pointing systematic.

984 7.8.2 $\mathcal{G}\mathcal{S}$ Versus \mathcal{B} spatial models

985 We show in this appendix a comparison between the J -factors computed by Geringer-Sameth
 986 *et al.* [53] (the $\mathcal{G}\mathcal{S}$ set) and the ones computed by Bonnivard *et al.* [47, 55] (the \mathcal{B} set). The
 987 $\mathcal{G}\mathcal{S}$ J -factors are computed through a Jeans analysis of the kinematic stellar data of the selected

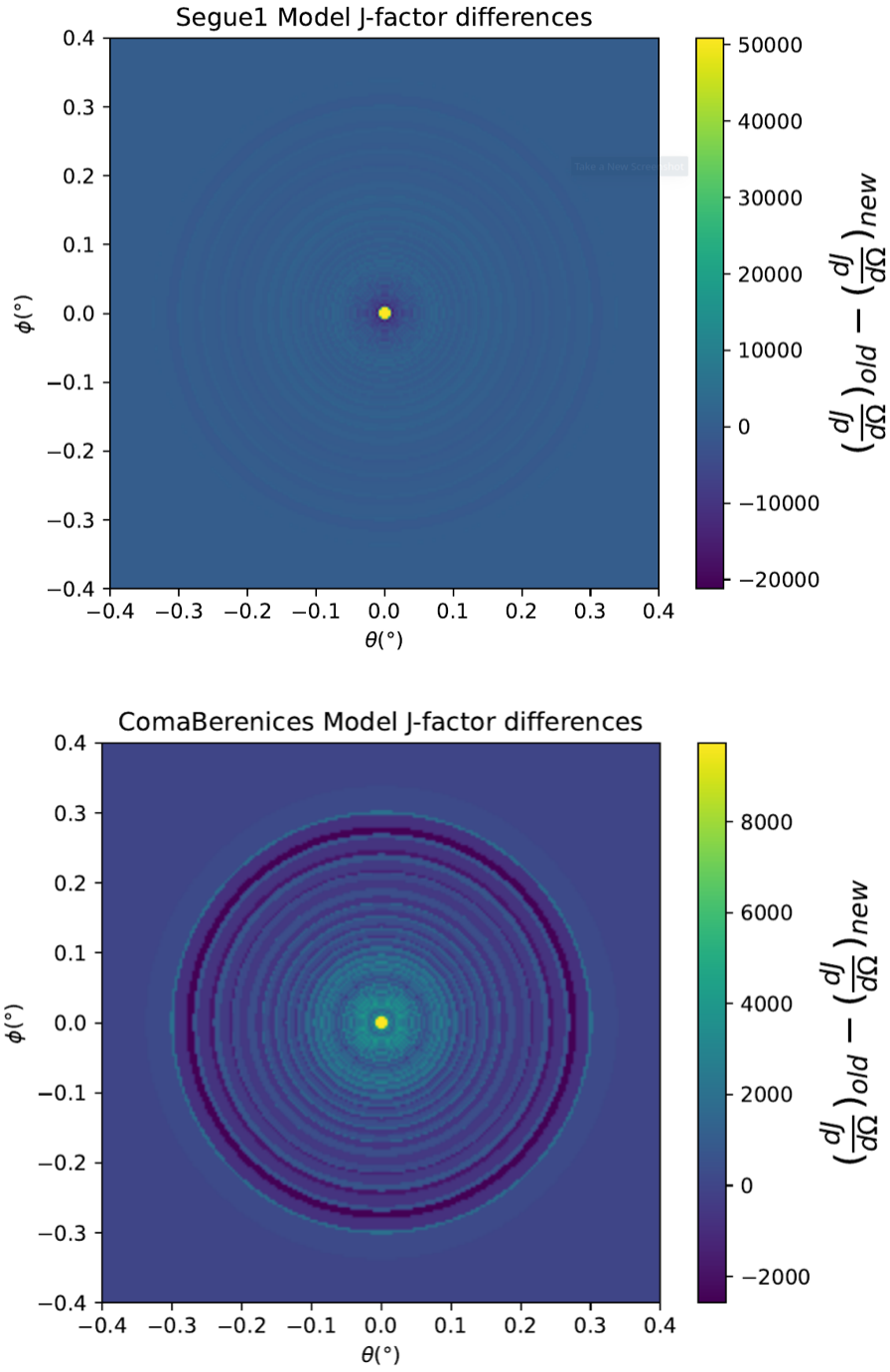


Figure 7.14 Differential map of dJ/Ω from model built in Section 7.8.1 and profiles provided directly from authors. (Top) Differential from Segue1. (bottom) Differential from Coma Berenices. Note that their scales are not the same. Segue1 shows the deepest discrepancies which is congruent with its large uncertainties. Both models show anuli where unique models become apparent.

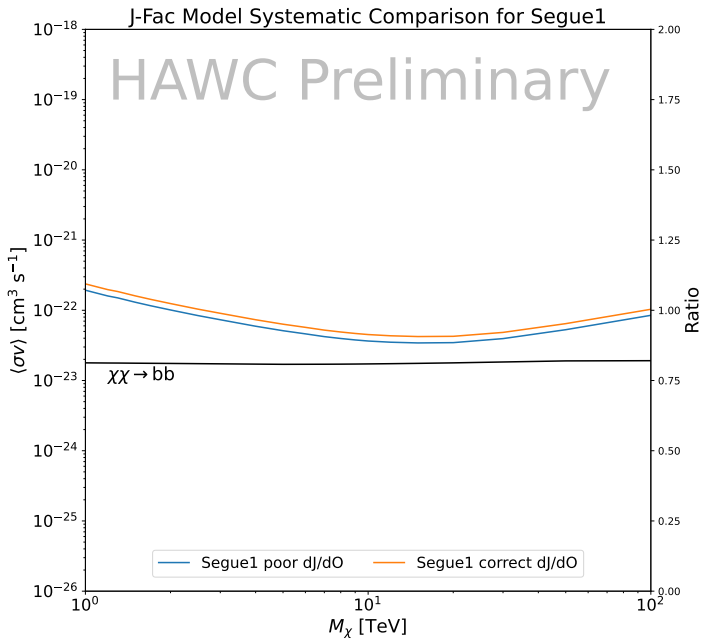
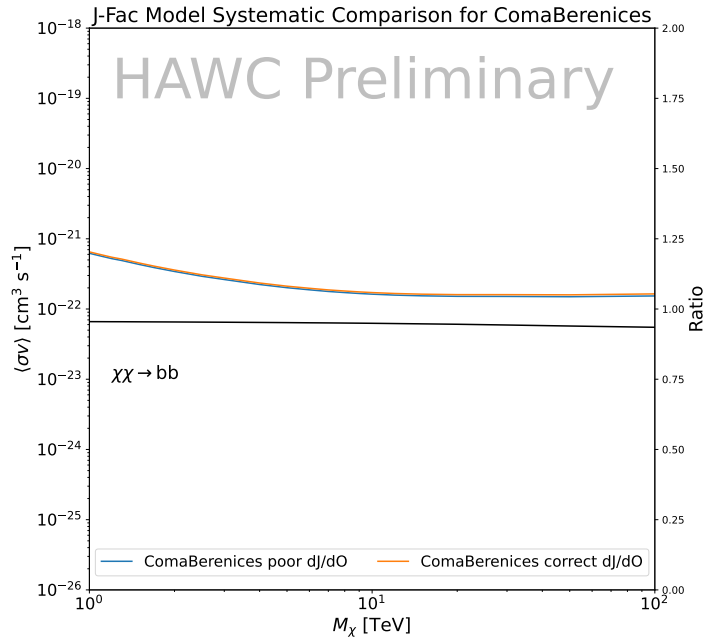


Figure 7.15 HAWC limits for Coma Berenices (top) and Segue1 (bottom) for two different map sets. Blue lines are limits calculated on maps with poor model representation. Orange lines are limits calculated on spatial profiles provided by the authors of [45]. Black line is the ratio of the poor spatial model limits to the corrected spatial models. The left y-axis measures $\langle \sigma v \rangle$ for the blue and orange lines. The right y-axis measures the ratio and is unitless.

988 dSphs, assuming a dynamic equilibrium and a spherical symmetry for the dSphs. They adopted
989 the generalized DM density distribution, known as Zhao-Hernquist, introduced by [58], carrying
990 three additional index parameters to describe the inner and outer slopes, and the break of the
991 density profile. Such a profile parametrization allows the reduction of the theoretical bias from
992 the choice of a specific radial dependency on the kinematic data. In other words, the increase of
993 free parameters with the use of the Zhao-Hernquist profile allows a better description of the mass
994 density distribution of dark matter.

995 In addition, a constant velocity anisotropy profile and a Plummer light profile [59] for the stellar
996 distribution were assumed. The velocity anisotropy profile depends on the radial and tangential
997 velocity dispersion. However, its determination remains challenging since only the line-of-sight
998 velocity dispersion can be derived from velocity measurements. Therefore, the parametrization of
999 the anisotropy profile is obtained from simulated halos (see [60] for more details). They provide the
1000 values of the J -factors of regions extending to various angular radius up to the outermost member
1001 star.

1002 The \mathcal{B} J -factors were computed through a Jeans analysis taking into account the systematic
1003 uncertainties induced by the DM profile parametrization, the radial velocity anisotropy profile, and
1004 the triaxiality of the halo of the dwarf galaxies. They performed a more complete study of the dSph
1005 kinematics and dynamics than \mathcal{GS} for the determination of the J -factor. Conservative values of the
1006 J -factors where obtained using an Einasto DM density profile [61], a realistic anisotropy profile
1007 known as the Baes & Van Hese profile [62] which takes into account that the inner regions can be
1008 significantly non-isotropic, and a Zhao-Hernquist light profile [58].

1009 For both sets, J -factor values are provided for all dSphs as a function of the radius of the
1010 integration region [53, 47, 55]. Table 7.1 shows the heliocentric distance and Galactic coordinates
1011 of the twenty dSphs, together with the two sets of J -factor values integrated up to the outermost
1012 observed star for \mathcal{GS} and the tidal radius for \mathcal{B} . Both J -factor sets were derived through a Jeans
1013 analysis based on the same kinematic data, except for Draco where the measurements of [63] have
1014 been adopted in the computation of the \mathcal{B} value. The computations for producing the \mathcal{GS} and \mathcal{B}

1015 samples differ in the choice of the DM density, velocity anisotropy, and light profiles, for which the
1016 set \mathcal{B} takes into account some sources of systematic uncertainties.

1017 Figure 7.16 and Figure 7.17 show the comparisons for the J -factor versus the angular radius
1018 for each of the 20 dSphs used in this study. The uncertainties provided by the authors are also
1019 indicated in the figures. For the \mathcal{GS} set, the computation stops at the angular radius corresponding
1020 to the outermost observed star, while for the \mathcal{B} set, the computation stops at the angular radius
1021 corresponding to the tidal radius.

1022 7.9 Discussion and Conclusions

1023 In this multi-instrument analysis, we have used observations of 20 dSphs from the gamma-ray
1024 telescopes Fermi-LAT, H.E.S.S., MAGIC, VERITAS, and HAWC to perform a collective DM
1025 search annihilation signals. The data were combined across sources and detectors to significantly
1026 increase the sensitivity of the search. We have observed no significant deviation from the null, no
1027 DM, hypothesis, and so present our results in terms of upper limits on the annihilation cross-section
1028 for seven potential DM annihilation channels.

1029 Fermi-LAT brings the most stringent constraints for continuum channels below approximately
1030 1 TeV. The remaining detectors dominate at higher energies. Overall, for multi-TeV DM mass,
1031 the combined DM constraints from all five telescopes are 2-3 times stronger than any individual
1032 telescope for multi-TeV DM.

1033 Derived from observations of many dSphs, our results produce robust limits given the DM
1034 content of the dSphs is relatively well constrained. The obtained limits span the largest mass
1035 range of any WIMP DM search. Our combined analysis improves the sensitivity over previously
1036 published results from each detector which produces the most stringent limits on DM annihilation
1037 from dSphs. These results are based on deep exposures of the most promising known dSphs with
1038 the currently most sensitive gamma-ray instruments. Therefore, our results constitute a legacy of
1039 a generation of gamma-ray instruments on WIMP DM searches towards dSphs. Our results will
1040 remain the reference in the field until a new generation of more sensitive gamma-ray instruments
1041 begin operations, or until new dSphs with higher J -factors are discovered.

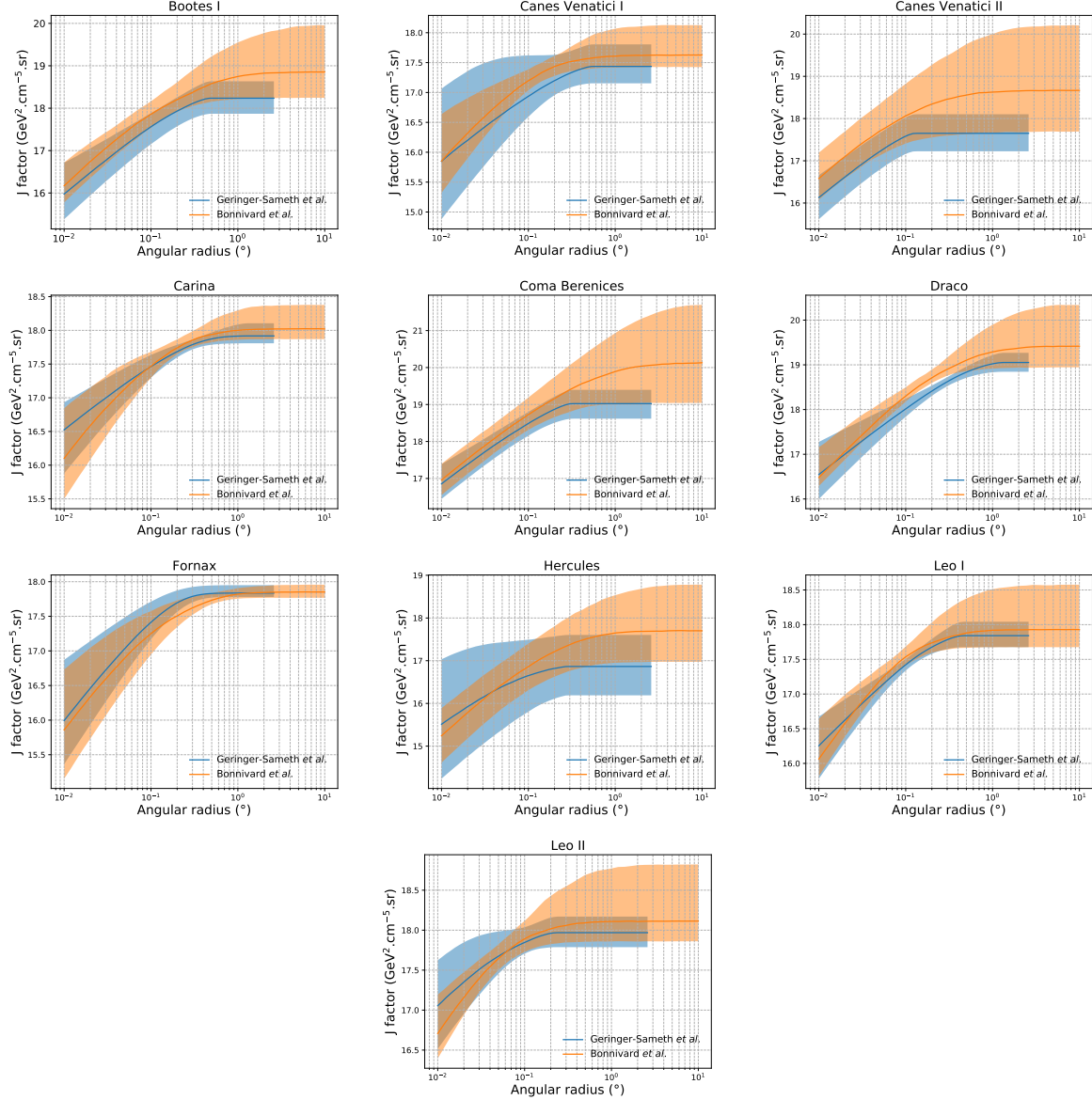


Figure 7.16 Comparisons between the J -factors versus the angular radius for the computation of J factors from Ref. [53] (\mathcal{GS} set in Table 7.1) in blue and for the computation from Ref. [47, 55] (\mathcal{B} set in Tab. 7.1) in orange. The solid lines represent the central value of the J -factors while the shaded regions correspond to the 1σ standard deviation.

This analysis serves as a proof of concept for future multi-instrument and multi-messenger combination analyses. With this collaborative effort, we have managed to sample over four orders in magnitude in gamma-ray energies with distinct observational techniques. Determining the nature of DM continues to be an elusive and difficult problem. Larger datasets with diverse measurement techniques could be essential to tackling the DM problem. A future collaboration using similar

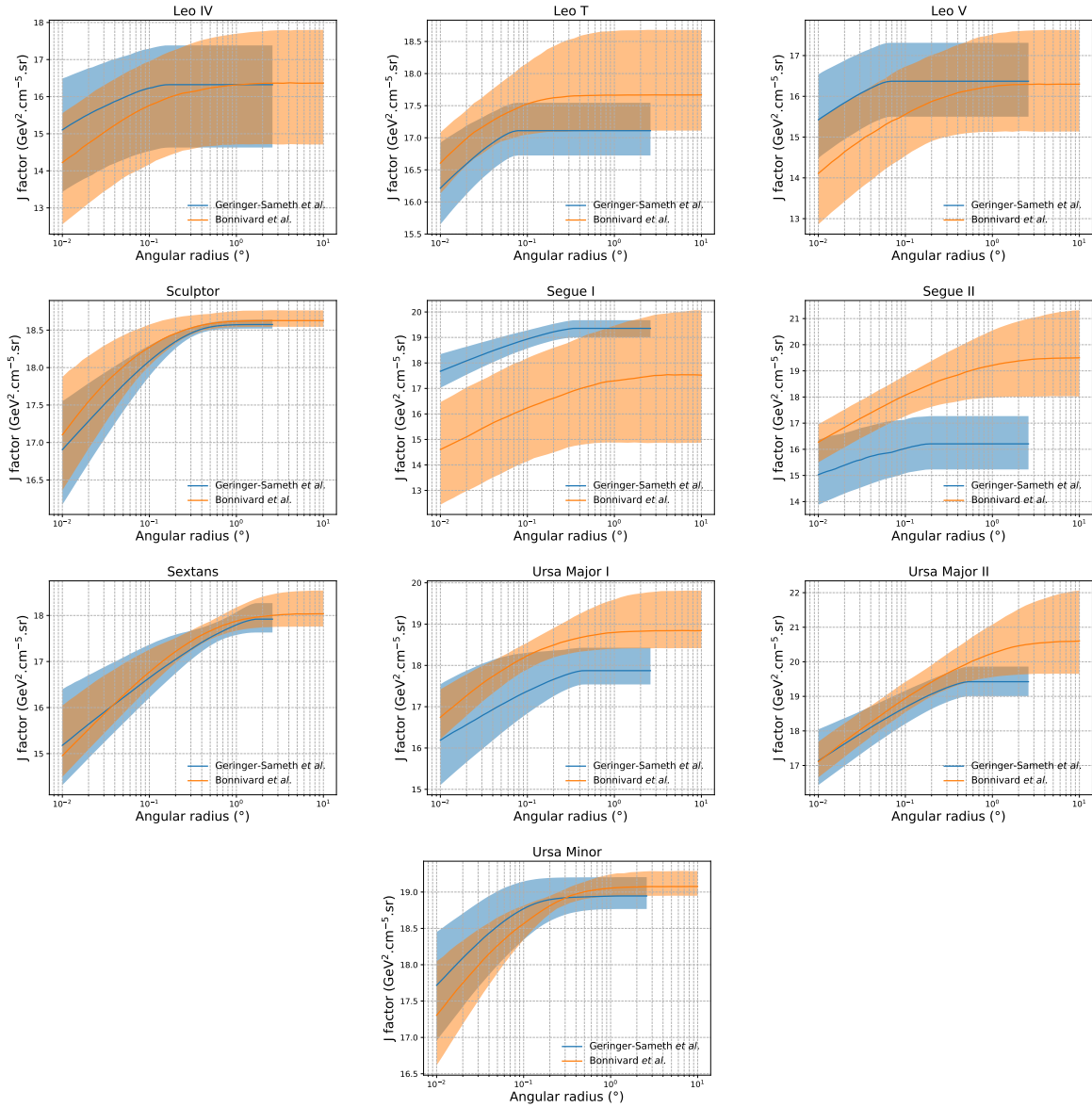


Figure 7.17 Comparisons between the J -factors versus the angular radius for the computation of J factors from Ref. [53] (\mathcal{GS} set in Tab. 7.1) in blue and for the computation from Ref. [47, 55] (\mathcal{B} set in Tab. 7.1) in orange. The solid lines represent the central value of the J -factors while the shaded regions correspond to the 1σ standard deviation.

1047 techniques as the ones described in this paper could grow even beyond gamma rays. The models we
 1048 used for this study include annihilation channels with neutrinos in the final state. Advanced studies
 1049 could aim to merge our results with those from neutrino observatories with large data sets. Efforts
 1050 are already underway to add data from the IceCube, ANTARES, and KM3NeT observatories to
 1051 these gamma-ray results.

1052 From this work, a selection of the best candidates for observations, according to the latest
1053 knowledge on stellar dynamics and modelling techniques for the derivation of the J -factors on
1054 the potential dSphs targets, is highly desirable at the time that new experiments are starting their
1055 dark matter programs using dSphs. Given the systematic uncertainty inherent to the derivation of
1056 the J -factors, an informed observational strategy would be to select both objects with the highest
1057 J -factors that could lead to DM signal detection, and objects with robust J -factor predictions, i.e.
1058 with kinematic measurements on many bright stars, which would strengthen the DM interpretation
1059 reliability of the observation outcome.

1060 This analysis combines data from multiple telescopes to produce strong constraints on astro-
1061 physical objects. From this perspective, these methods can be applied beyond just DM searches.
1062 Almost every astrophysical study can benefit from multi-telescope, multi-wavelength gamma-ray
1063 studies. We have enabled these telescopes to study the cosmos with greater precision and detail.
1064 Many astrophysical searches can benefit from multi-instrument gamma-ray studies, for which our
1065 analysis lays the foundation.

CHAPTER 8

1066 MULTITHREADING HAWC ANALYSES FOR DARK MATTER SEARCHES

1067 **8.1 Introduction**

1068 HAWC’s current software suite, plugins to 3ML, does not fully utilize computational advancements of recent decades. Said advancements include the proliferation of Graphical Processing
1069 Units (GPUs), and multithreading on multi-core processors. The analysis described in chapter 7
1070 took up to 3 months of human time waiting for the full gambit of data analysis and simulation
1071 of background to run. Additionally, with the addition of a 2D binning scheme, f_{hit} and NN, the
1072 expected compute time is expected to grow further. Although excessive computing time was, in
1073 part, from an intense use of a shared computing cluster, it was evident that there was room for
1074 improvement. In HAWC’s next generation dSph DM search, I decided to develop codes that would
1075 utilize the multi-core processors on modern high performance computing clusters. The results of
1076 this work are featured in this chapter and brought a human timing improvement to computation that
1077 scales as $1/N$ where N is the number of threads.

1079 **8.2 Dataset and Background**

1080 This section enumerates the data and background methods used for HAWC’s multi-threaded
1081 study of dSphs. Section 8.2.1 and Section 8.2.2 are most useful for fellow HAWC collaborators
1082 looking to replicate a multithreaded dSph DM search.

1083 **8.2.1 Itemized HAWC files**

- 1084 • Detector Resolution: `refit-Pass5-Final-NN-detRes-zenith-dependent.root`
- 1085 • Data Map: `Pass5-Final-NN-maptree-ch103-ch1349-zenith-dependent.root`
- 1086 • Spectral Dictionary: `HDMspectra_dict_gamma.npy`

1087 **8.2.2 Software Tools and Development**

1088 This analysis was performed using HAL and 3ML [42, 43] in Python version 3. I built software
1089 in collaboration with Michael Martin and Letrell Harris to implement the *Dark Matter Spectra from*

1090 *the Electroweak to the Planck Scale* (HDM) [64] and dSphs spatial model from [65] for HAWC
1091 analysis. A NumPy dictionary of HDM was made for Py3. The corresponding Python3 file is
1092 `HDMspectra_dict_gamma.npy`. These files can also be used for decay channels and tools are
1093 provided in HDM’s [git repository](#) [64]. The analysis was performed using the Neural Network
1094 energy estimator for Pass 5.F. A description of this estimator was provided in chapter 4. **TODO:**
1095 **define a subsection when it’s written** All other software used for data analysis, DM profile generation,
1096 and job submission to SLURM are also kept in my sandbox in the [Dark Matter HAWC](#) project.
1097 The above repository also incorporates the model inputs used previously in Glory Duck, described
1098 in chapter 7

1099 **8.2.3 Data Set and Background Description**

1100 The HAWC data maps used for this analysis contain 2565 days of data between runs 2104 (1101 **TODO: Day start**) and 7476 (**TODO: day end**). They were generated from pass 4.0 reconstruction.
1102 The analysis is performed using the NN energy estimator with bin list:

1103 B1C0Ea, B1C0Eb, B1C0Ec, B1C0Ed, B1C0Ee, B2C0Ea, B2C0Eb, B2C0Ec, B2C0Ed, B2C0Ee,
1104 B3C0Ea, B3C0Eb, B3C0Ec, B3C0Ed, B3C0Ee, B3C0Ef, B4C0Eb, B4C0Ec, B4C0Ed, B4C0Ee,
1105 B4C0Ef, B5C0Ec, B5C0Ed, B5C0Ee, B5C0Ef, B5C0Eg, B6C0Ed, B6C0Ee, B6C0Ef, B6C0Eg,
1106 B6C0Eh, B7C0Ee, B7C0Ef, B7C0Eg, B7C0Eh, B7C0Ei, B8C0Ee, B8C0Ef, B8C0Eg, B8C0Eh,
1107 B8C0Ei, B8C0Ej, B9C0Ef, B9C0Eg, B9C0Eh, B9C0Ei, B9C0Ej, B10C0Eg, B10C0Eh,
1108 B10C0Ei, B10C0Ej, B10C0Ek, B10C0El

1109 Bin 0 was excluded as it has substantial hadronic contamination and poor angular resolution.

1110 Background considerations and source selection was identical to Section 7.2, and no additional
1111 arguments are provided here. Many of the HAWC systematics explored in Section 7.7 also apply
1112 for this DM search and are not added upon here.

1113 **8.3 Analysis**

1114 The analysis and its systematics are almost identical to Section 7.3. Importantly, we use the
1115 same Equation (7.1) and Equation (7.2) for estimating the gamma-ray flux at HAWC from our

sources. We add on to the previous study with a search for DM decay. The flux equations for DM decay are

$$\frac{d\Phi_\gamma}{dE_\gamma} = \frac{1}{4\pi\tau m_\chi} \frac{dN_\gamma}{dE_\gamma} \times \int_{\text{source}} d\Omega \int_{l.o.s} dl \rho_\chi dl(r, \theta') \quad (8.1)$$

with a new quantity, the D factor, defined as

$$D = \int d\Omega \int_{l.o.s} dl \rho_\chi(r, \theta') \quad (8.2)$$

Software was written to accomodate DM decay from dSphs, however decay profiles were not received from $\mathcal{L}\mathcal{S}$ by the time of writing this tehsis.

8.3.1 $\frac{dN_\gamma}{dE_\gamma}$ - Particle Physics Component

For these spectra, we import HDM with Electroweak (EW) corrections and additional corrections for neutrinos above the EW scale [64]. The spectrum is implemented as a model script in astromodels for 3ML. A comprehensive description of EW corrections and neutrino considerations are provided later in [TODO: refeance MM nu duck](#).

Figure 8.1 demonstrates the impact of changes from HDM on DM annihilation to W bosons. A class in astromodels was developed to include HDM and is aptly named `HDMspectra` within `DM_models.py`. The SM DM annihilation channels studied here are $\chi\chi \rightarrow:$

$$e^+e^-, \mu^+\mu^-, \tau^+\tau^-, b\bar{b}, t\bar{t}, gg, W^+W^-, ZZ, c\bar{c}, u\bar{u}, d\bar{d}, s\bar{s}, \nu_e\bar{\nu}_e, \nu_\mu\bar{\nu}_\mu, \nu_\tau\bar{\nu}_\tau, \gamma\gamma, hh.$$

For $\gamma\gamma$ and ZZ , a substantial fraction of the signal photons are expected to have total energy equal m_χ [64]. This introduces a δ -function that is much narrower than the energy resolution of the HAWC detector. To ensure that this feature is not lost in the likelihood fits, the 'line' feature is convolved with a gaussian kernel with a 1σ width of $0.05 \cdot m_\chi$ and total kernel window of $\pm 4\sigma$. This differs from HAWC's previous line study where 30% of HAWC's energy resolution was used for the kernel [66]. The NN energy estimator's strength compared to f_{hit} at low gamma-ray energy enables smaller resolutions in addition to low energy tails in the spectral models [64]. $\chi\chi \rightarrow \gamma\gamma$ and ZZ spectral hypotheses are shown in Figure 8.2. Spectral models for the remaining annihilation channels are plotted for each m_χ in Figure B.1.

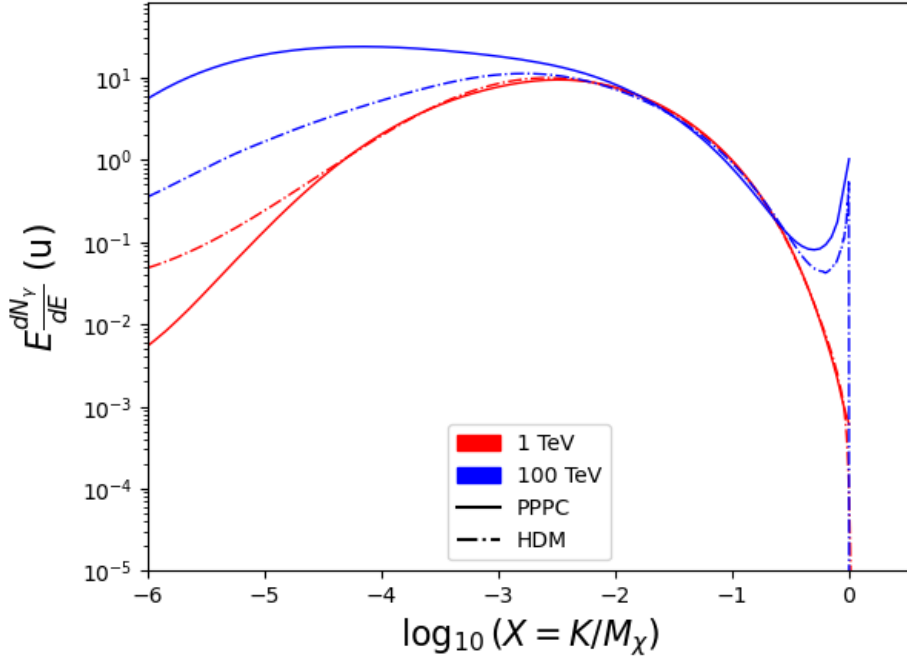


Figure 8.1 Difference between spectral hypotheses from PPPC [44] and HDM [64]. Shown is the expected DM annihilation spectrum for $\chi\chi \rightarrow W^-W^+$. Solid lines are spectral models with EW corrections from the PPPC. Dash-dot lines are spectral models from HDM. Red lines are models for $M_\chi = 1$ TeV. Blue lines represent models for $M_\chi = 100$ TeV.

8.3.2 J and D- Astrophysical Components

The J-factor profiles for each source are imported from Louis Strigari et al. (referred to with

$\mathcal{L}S$) [65]. Profiles in $\frac{dJ}{d\Omega}(\theta)$ and $\frac{dD}{d\Omega}(\theta)$ up to $\theta = 0.5^\circ$ were provided directly from the authors.

Map generation from these profiles were almost identical to Section 7.3.2 except that a higher order

trapezoidal integral was used for the normalization of the square, uniformly-spaced map:

$$p^2 \cdot \sum_{i=0}^N \sum_{j=0}^M w_{i,j} \frac{d\mathcal{K}}{d\Omega}(\theta_{i,j}, \phi_{i,j}) \quad (8.3)$$

\mathcal{K} is either J or D for the spatial distributions of annihilation or decay respectively. p is the angular

side of one pixel in the map. $w_{i,j}$ is a weight assigned the following ways:

$w_{i,j} = 1$ if $(\theta_{i,j}, \phi_{i,j})$ is fully within the region of integration

$w_{i,j} = 1/2$ if $(\theta_{i,j}, \phi_{i,j})$ is on an edge of the region of integration

$w_{i,j} = 1/4$ if $(\theta_{i,j}, \phi_{i,j})$ is on a corner of the region of integration

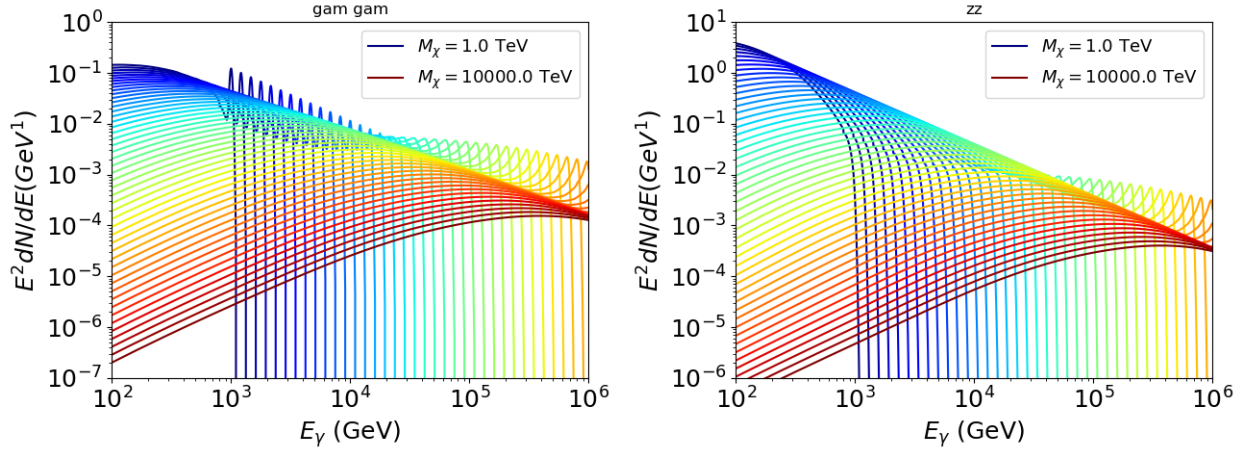


Figure 8.2 Photon spectra for $\chi\chi \rightarrow \gamma\gamma$ (left) and $\chi\chi \rightarrow ZZ$ (right) after gaussian convolution of line features. Both spectra have δ -features at photon energies equal to the DM mass. Bluer lines are annihilation spectra with lower DM mass. Redder lines are spectra from larger DM mass. All Spectral models are sourced from the Heavy Dark Matter models [64].

1149 Figure 8.3 shows the median and $\pm 1\sigma$ maps used as input for DM annihilation studied by \mathcal{LS} .

1150 **8.3.3 Source Selection and Annihilation Channels**

1151 We use many of the dSphs presented in HAWC's previous dSph DM search [46]. HAWC's
 1152 sources for Glory Duck include Boötes I, Coma Berenices, Canes Venatici I + II, Draco, Hercules,
 1153 Leo I, II, + IV, Segue 1, Sextans, and Ursa Major I + II. A full description of all sources used
 1154 in Glory Duck is found in Table 7.1. Triangulum II was excluded from the Glory Duck analysis
 1155 because of large uncertainties in its J factor. Ursa Minor was excluded from HAWC's contribution
 1156 to the combination because the source extension model extended Ursa Minor beyond HAWC's field
 1157 of view. Ursa Minor was not expected to contribute significantly to the combined limit, so work
 1158 was not invested in a solution to include Ursa Minor.

1159 This analysis improves on the previous HAWC dSph paper [46] in the following ways. Pre-
 1160 viously, the dSphs were treated and implemented as point sources. For this analysis, dSphs are
 1161 modeled and treated as extended source. The impact of this change with respect to the upper limit
 1162 is source dependent and is explored in Section 7.7.2. Previously, the particle physics model used for
 1163 gamma-ray spectra from DM annihilation did not have EW corrections where the PPPC includes
 1164 them. Finally, the gamma-ray ray dataset is much larger. The study performed here analyzes over

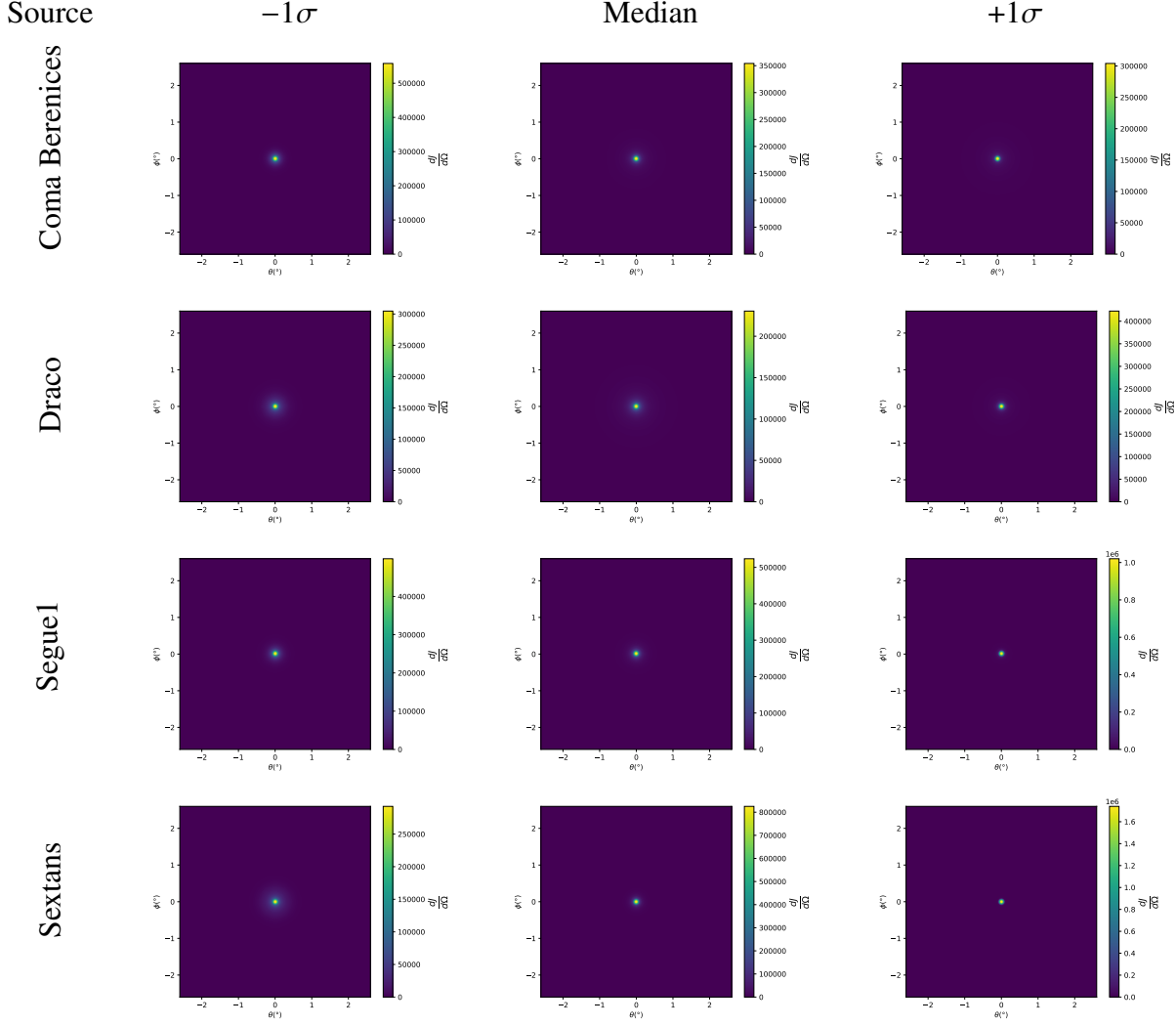


Figure 8.3 $\frac{dJ}{d\Omega}$ maps for Coma Berenices, Draco, Segue1, and Sextans. Columns are divided for the $\pm 1\sigma$ uncertainties in $dJ/d\Omega$ around the median value from LS [65]. Origin is centered on the specific dwarf spheroidal galaxies (dSph). θ and ϕ axes are the angular separation from the center of the dwarf. Axes are drawn roughly according to the energy sensitivity of HAWC.

1165 1000 days of data compared to 507.

1166 The SM annihilation channels probed for the Glory Duck combination include $b\bar{b}$, $e\bar{e}$, $\mu\bar{\mu}$, $\tau\bar{\tau}$,
 1167 $t\bar{t}$, W^+W^- , and ZZ . A summary of all sources, with a description of each experiments' sensitivity
 1168 to the source, is provided in Table 7.2.

Name	Distance (kpc)	l, b ($^{\circ}$)	$\log_{10} J$ ($\mathcal{G}\mathcal{S}$ set) $\log_{10}(\text{GeV}^2\text{cm}^{-5}\text{sr})$	$\log_{10} J$ (\mathcal{B} set) $\log_{10}(\text{GeV}^2\text{cm}^{-5}\text{sr})$
Coma Berenices	44	241.89, 83.61	$19.02^{+0.37}_{-0.41}$	$20.13^{+1.56}_{-1.08}$
Draco	76	86.37, 34.72	$19.05^{+0.22}_{-0.21}$	$19.42^{+0.92}_{-0.47}$
Segue I	23	220.48, 50.43	$19.36^{+0.32}_{-0.35}$	$17.52^{+2.54}_{-2.65}$
Sextans	86	243.50, 42.27	$17.92^{+0.35}_{-0.29}$	$18.04^{+0.50}_{-0.28}$

Table 8.1 Summary of the relevant properties of the dSphs used in the present work. Column 1 lists the dSphs. Columns 2 and 3 present their heliocentric distance and galactic coordinates, respectively. Columns 4 and 5 report the J -factors of each source given from the $\mathcal{G}\mathcal{S}$ and \mathcal{B} independent studies and their estimated $\pm 1\sigma$ uncertainties. The values $\log_{10} J$ ($\mathcal{G}\mathcal{S}$ set) [45] correspond to the mean J -factor values for a source extension truncated at the outermost observed star. The values $\log_{10} J$ (\mathcal{B} set) [47] are provided for a source extension at the tidal radius of each dSph.

CHAPTER 9

1169 **HEAVY DARK MATTER ANNIHILATION SEARCH WITH ICECUBE'S NORTH SKY**
1170 **TRACK DATA**

CHAPTER 10

NU DUCK

APPENDIX A

MULTI-EXPERIMENT SUPPLEMENTARY FIGURES

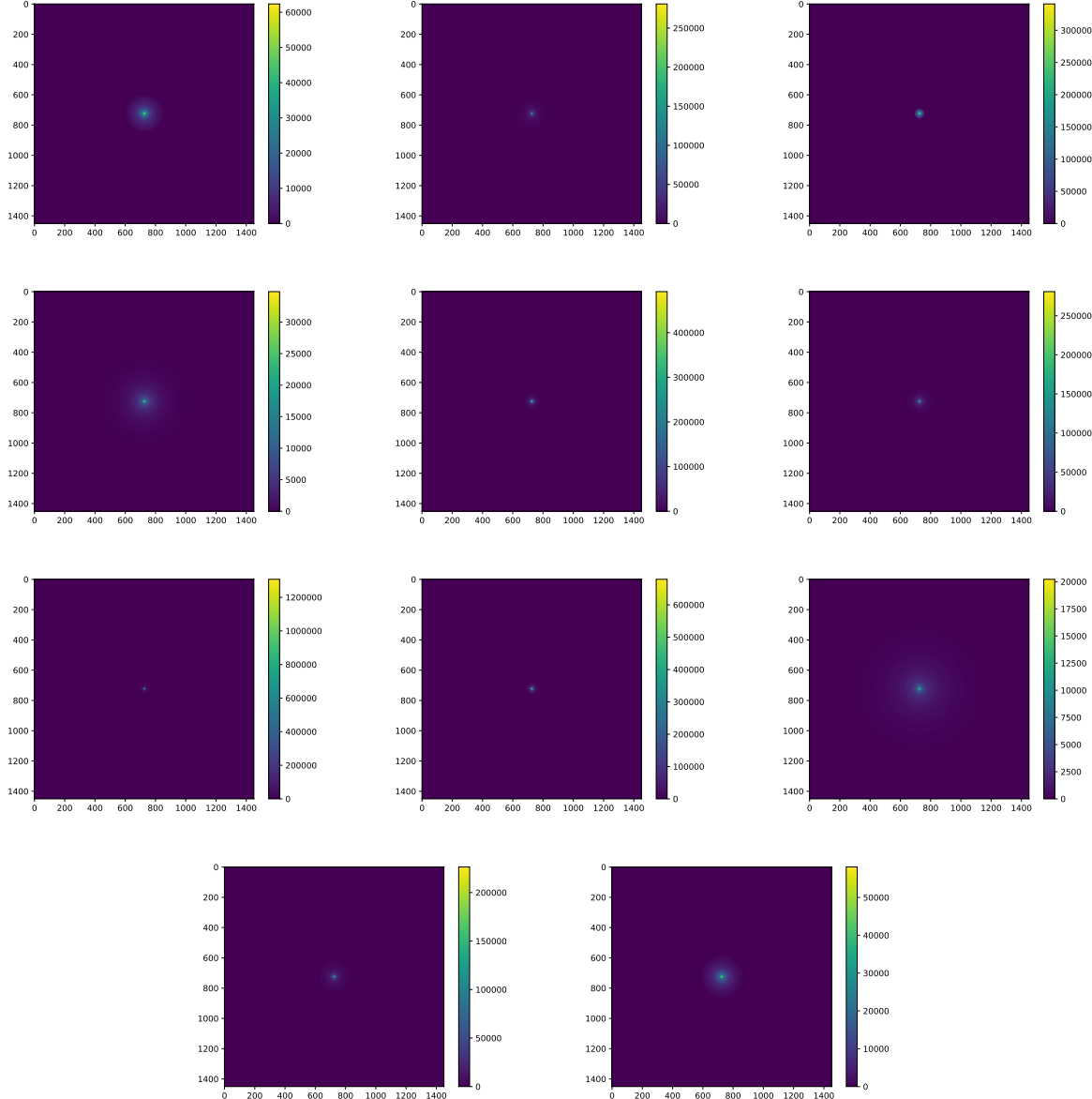


Figure A.1 Sister figure to Figure 7.3. Sources in the first row from left to right: Bootes I, Canes Venatici I, II. In second row: Draco, Hercules, Leo I. In the first row: Leo II, Leo IV, Sextans. In the final row: Ursa Major I, Ursa Major II.

APPENDIX B

MULTITHREADING SUPPLEMENTARY FIGURES

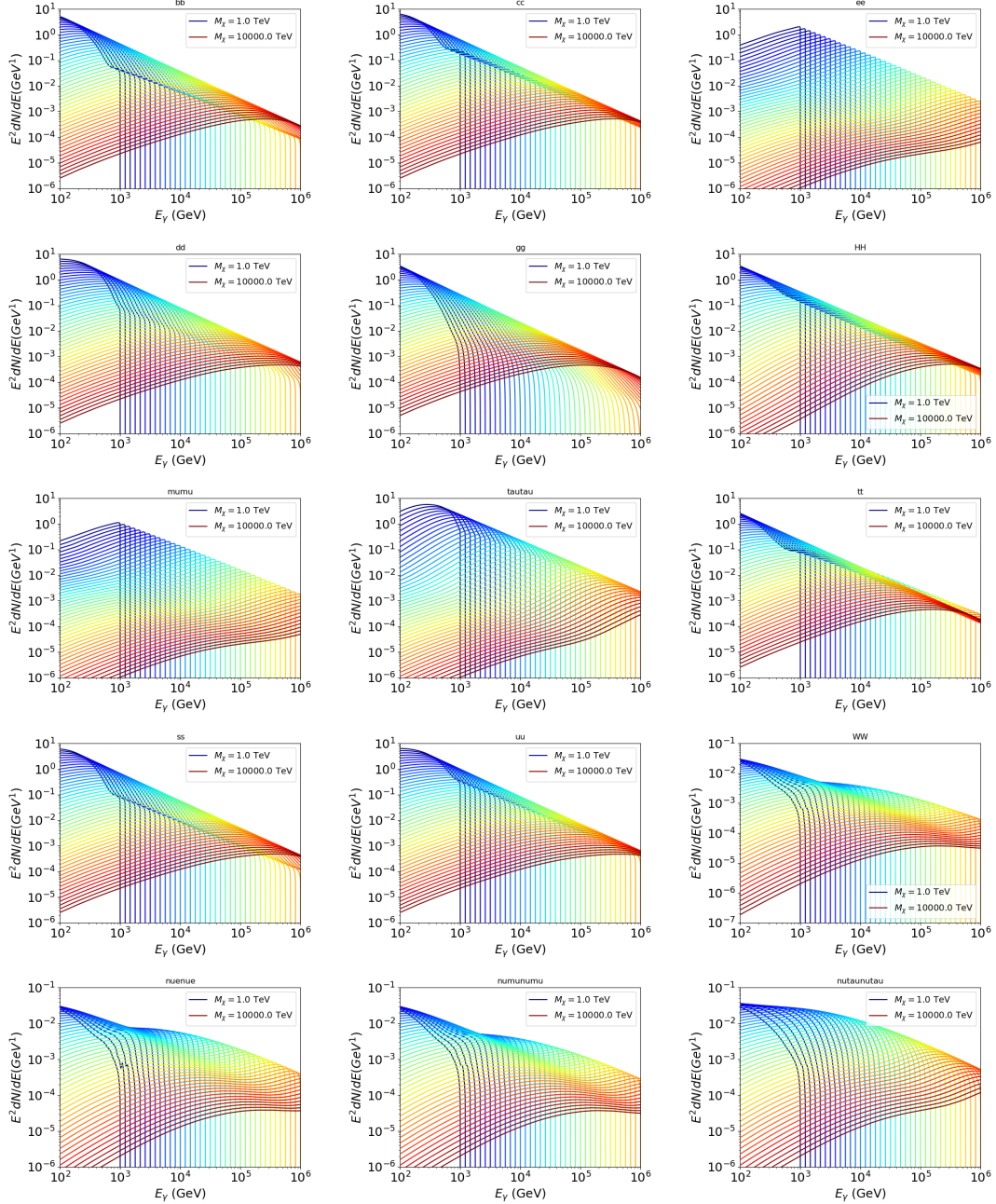


Figure B.1 Sister figure to Figure 8.2 for remaining SM primary annihilation channels studied for this thesis. These did not require any post generation smoothing and so are directly pulled from [64] with a binning scheme most helpful for a HAWC analysis.

BIBLIOGRAPHY

- 1175 [1] Anne M. Green. “Dark matter in astrophysics/cosmology”. In: *SciPost Phys. Lect.*
 1176 *Notes* (2022), p. 37. doi: [10.21468/SciPostPhysLectNotes.37](https://doi.org/10.21468/SciPostPhysLectNotes.37). URL: <https://scipost.org/10.21468/SciPostPhysLectNotes.37>.
- 1178 [2] Bing-Lin Young. “A survey of dark matter and related topics in cosmology”. In: *Frontiers*
 1179 *of Physics* 12 (Oct. 2016). doi: <https://doi.org/10.1007/s11467-016-0583-4>.
 1180 URL: <https://doi.org/10.1007/s11467-016-0583-4>.
- 1181 [3] Gianfranco Bertone, Dan Hooper, and Joseph Silk. “Particle dark matter: evidence,
 1182 candidates and constraints”. In: *Physics Reports* 405.5 (2005), pp. 279–390. ISSN:
 1183 0370-1573. doi: <https://doi.org/10.1016/j.physrep.2004.08.031>. URL:
 1184 <https://www.sciencedirect.com/science/article/pii/S0370157304003515>.
- 1185 [4] Gianfranco Bertone and Dan Hooper. “History of dark matter”. In: *Rev. Mod. Phys.*
 1186 90 (4 Aug. 2018), p. 045002. doi: [10.1103/RevModPhys.90.045002](https://doi.org/10.1103/RevModPhys.90.045002). URL: <https://link.aps.org/doi/10.1103/RevModPhys.90.045002>.
- 1188 [5] Fritz Zwicky. “The Redshift of Extragalactic Nebulae”. In: *Helvetica Physica Acta* 6.
 1189 (1933), pp. 110–127. doi: [10.5169/seals-110267](https://doi.org/10.5169/seals-110267).
- 1190 [6] Vera C. Rubin and Jr. Ford W. Kent. “Rotation of the Andromeda Nebula from a
 1191 Spectroscopic Survey of Emission Regions”. In: *ApJ* 159 (Feb. 1970), p. 379. doi:
 1192 [10.1086/150317](https://doi.org/10.1086/150317).
- 1193 [7] K. G. Begeman, A. H. Broeils, and R. H. Sanders. “Extended rotation curves of spiral galax-
 1194 ies: dark haloes and modified dynamics”. In: *Monthly Notices of the Royal Astronomical So-*
 1195 *ciety* 249.3 (Apr. 1991), pp. 523–537. ISSN: 0035-8711. doi: [10.1093/mnras/249.3.523](https://doi.org/10.1093/mnras/249.3.523).
 1196 eprint: <https://academic.oup.com/mnras/article-pdf/249/3/523/18160929/mnras249-0523.pdf>. URL: <https://doi.org/10.1093/mnras/249.3.523>.
- 1198 [8] *Different types of gravitational lenses*. website. Feb. 2004. URL: <https://esahubble.org/images/heic0404b/>.
- 1200 [9] Douglas Clowe et al. “A Direct Empirical Proof of the Existence of Dark Matter”. In: *apjl*
 1201 648.2 (Sept. 2006), pp. L109–L113. doi: [10.1086/508162](https://doi.org/10.1086/508162). arXiv: [astro-ph/0608407](https://arxiv.org/abs/astro-ph/0608407)
 1202 [[astro-ph](https://arxiv.org/abs/astro-ph/0608407)].
- 1203 [10] Planck Collaboration and N. et. al. Aghanim. “Planck 2018 results I. Overview and the
 1204 cosmological legacy of Planck”. In: *A&A* 641 (2020). doi: [10.1051/0004-6361/201833880](https://doi.org/10.1051/0004-6361/201833880). URL: <https://doi.org/10.1051/0004-6361/201833880>.
- 1206 [11] Wayne Hu. *Matter Density Animation*. web. 2024. URL: <http://background.uchicago.edu/~whu/animbut/anim2.html>.

- 1208 [12] Wenlong Yuan et al. “A First Look at Cepheids in a Type Ia Supernova Host with JWST”. in:
1209 *The Astrophysical Journal Letters* 940.1 (Nov. 2022). doi: [10.3847/2041-8213/ac9b27](https://doi.org/10.3847/2041-8213/ac9b27).
1210 URL: <https://dx.doi.org/10.3847/2041-8213/ac9b27>.
- 1211 [13] Wendy L. Freedman. “Measurements of the Hubble Constant: Tensions in Perspective”. In:
1212 *The Astrophysical Journal* 919.1 (Sept. 2021), p. 16. doi: [10.3847/1538-4357/ac0e95](https://doi.org/10.3847/1538-4357/ac0e95).
1213 URL: <https://dx.doi.org/10.3847/1538-4357/ac0e95>.
- 1214 [14] Jodi Cooley. “Dark Matter direct detection of classical WIMPs”. In: *SciPost Phys. Lect.*
1215 *Notes* (2022), p. 55. doi: [10.21468/SciPostPhysLectNotes.55](https://doi.org/10.21468/SciPostPhysLectNotes.55). URL: <https://scipost.org/10.21468/SciPostPhysLectNotes.55>.
- 1217 [15] “Search for new phenomena in events with an energetic jet and missing transverse momentum
1218 in pp collisions at $\sqrt{s} = 13$ TeV with the ATLAS detector”. In: *Phys. Rev. D* 103
1219 (11 July 2021), p. 112006. doi: [10.1103/PhysRevD.103.112006](https://doi.org/10.1103/PhysRevD.103.112006). URL: <https://link.aps.org/doi/10.1103/PhysRevD.103.112006>.
- 1221 [16] *Jetting into the dark side: a precision search for dark matter*. website. July 2020. URL:
1222 <https://atlas.cern/updates/briefing/precision-search-dark-matter>.
- 1223 [17] Celine Armand et. al. “Combined dark matter searches towards dwarf spheroidal galaxies
1224 with Fermi-LAT, HAWC, H.E.S.S., MAGIC, and VERITAS”. in: *Proceedings of Science*.
1225 Vol. 395. Mar. 2022. doi: <https://doi.org/10.22323/1.395.0528>.
- 1226 [18] Tracy R. Slatyer. “Les Houches Lectures on Indirect Detection of Dark Matter”. In: *SciPost*
1227 *Phys. Lect. Notes* (2022), p. 53. doi: [10.21468/SciPostPhysLectNotes.53](https://doi.org/10.21468/SciPostPhysLectNotes.53). URL:
1228 <https://scipost.org/10.21468/SciPostPhysLectNotes.53>.
- 1229 [19] Christian W Bauer, Nicholas L. Rodd, and Bryan R. Webber. “Dark matter spectra from
1230 the electroweak to the Planck scale”. In: *Journal of High Energy Physics* 2021.1029-8479
1231 (June 2021). doi: [https://doi.org/10.1007/JHEP06\(2021\)121](https://doi.org/10.1007/JHEP06(2021)121).
- 1232 [20] Riccardo Catena and Piero Ullio. “A novel determination of the local dark matter density”.
1233 In: *Journal of Cosmology and Astroparticle Physics* 2010.08 (Aug. 2010), p. 004. doi:
1234 [10.1088/1475-7516/2010/08/004](https://doi.org/10.1088/1475-7516/2010/08/004). URL: <https://dx.doi.org/10.1088/1475-7516/2010/08/004>.
- 1236 [21] B. P. Abbott et al. “Observation of Gravitational Waves from a Binary Black Hole Merger”.
1237 In: *Phys. Rev. Lett.* 116 (6 Feb. 2016), p. 061102. doi: [10.1103/PhysRevLett.116.061102](https://doi.org/10.1103/PhysRevLett.116.061102). URL: <https://link.aps.org/doi/10.1103/PhysRevLett.116.061102>.
- 1239 [22] R. Abbasi et. al. “Observation of high-energy neutrinos from the Galactic plane”. In: *Science*
1240 380.6652 (June 2023), pp. 1338–1343.
- 1241 [23] NASA Goddard Space Flight Center. *Fermi’s 12-year view of the gamma-ray sky*. website.

- 1242 2022. URL: <https://svs.gsfc.nasa.gov/14090>.
- 1243 [24] Marco Cirelli et al. “PPPC 4 DM ID: a poor particle physicist cookbook for dark matter
1244 indirect detection”. In: *Journal of Cosmology and Astroparticle Physics* 2011.03 (Mar.
1245 2011), p. 051. doi: [10.1088/1475-7516/2011/03/051](https://doi.org/10.1088/1475-7516/2011/03/051). URL: <https://dx.doi.org/10.1088/1475-7516/2011/03/051>.
- 1247 [25] Javier Rico. “Gamma-Ray Dark Matter Searches in Milky Way Satellites—A Comparative
1248 Review of Data Analysis Methods and Current Results”. In: *Galaxies* 8.1 (Mar. 2020), p. 25.
1249 doi: [10.3390/galaxies8010025](https://doi.org/10.3390/galaxies8010025). arXiv: [2003.13482](https://arxiv.org/abs/2003.13482) [astro-ph.HE].
- 1250 [26] W. B. Atwood et al. “The Large Area Telescope on the Fermi Gamma-Ray Space Telescope
1251 Mission”. In: *apj* 697.2 (June 2009), pp. 1071–1102. doi: [10.1088/0004-637X/697/2/1071](https://doi.org/10.1088/0004-637X/697/2/1071). arXiv: [0902.1089](https://arxiv.org/abs/0902.1089) [astro-ph.IM].
- 1253 [27] M. Ackermann et al. “Searching for Dark Matter Annihilation from Milky Way Dwarf
1254 Spheroidal Galaxies with Six Years of Fermi Large Area Telescope Data”. In: *prl* 115.23,
1255 231301 (Dec. 2015), p. 231301. doi: [10.1103/PhysRevLett.115.231301](https://doi.org/10.1103/PhysRevLett.115.231301). arXiv:
1256 [1503.02641](https://arxiv.org/abs/1503.02641) [astro-ph.HE].
- 1257 [28] Mattia Di Mauro, Martin Stref, and Francesca Calore. “Investigating the effect of Milky
1258 Way dwarf spheroidal galaxies extension on dark matter searches with Fermi-LAT data”.
1259 In: *Phys. Rev. D* 106 (12 Dec. 2022), p. 123032. doi: [10.1103/PhysRevD.106.123032](https://doi.org/10.1103/PhysRevD.106.123032).
1260 URL: <https://link.aps.org/doi/10.1103/PhysRevD.106.123032>.
- 1261 [29] F. et al. Aharonian. “Observations of the Crab Nebula with H.E.S.S.”. In: *Astron. Astrophys.*
1262 457 (2006), pp. 899–915. doi: [10.1051/0004-6361:20065351](https://doi.org/10.1051/0004-6361:20065351). arXiv: [astro-ph/0607333](https://arxiv.org/abs/astro-ph/0607333).
- 1264 [30] J. Albert et al. “VHE γ -Ray Observation of the Crab Nebula and its Pulsar with the MAGIC
1265 Telescope”. In: *The Astrophysical Journal* 674.2 (Feb. 2008), p. 1037. doi: [10.1086/525270](https://doi.org/10.1086/525270). URL: <https://dx.doi.org/10.1086/525270>.
- 1267 [31] N. Park. “Performance of the VERITAS experiment”. In: *Proceedings, 34th International
1268 Cosmic Ray Conference (ICRC2015): The Hague, The Netherlands, July, 30th July - 6th
1269 August*. Vol. 34. 2015, p. 771. arXiv: [1508.07070](https://arxiv.org/abs/1508.07070) [astro-ph.IM].
- 1270 [32] A. Abramowski et al. “H.E.S.S. constraints on Dark Matter annihilations towards the Sculptor
1271 and Carina Dwarf Galaxies”. In: *Astropart. Phys.* 34 (2011), pp. 608–616. doi: [10.1016/j.astropartphys.2010.12.006](https://doi.org/10.1016/j.astropartphys.2010.12.006). arXiv: [1012.5602](https://arxiv.org/abs/1012.5602) [astro-ph.HE].
- 1273 [33] A. Abramowski et al. “Search for dark matter annihilation signatures in H.E.S.S. observations
1274 of Dwarf Spheroidal Galaxies”. In: *Phys. Rev. D* 90 (2014), p. 112012. doi: [10.1103/PhysRevD.90.112012](https://doi.org/10.1103/PhysRevD.90.112012). arXiv: [1410.2589](https://arxiv.org/abs/1410.2589) [astro-ph.HE].

- 1276 [34] H. Abdalla et al. “Searches for gamma-ray lines and ‘pure WIMP’ spectra from Dark
1277 Matter annihilations in dwarf galaxies with H.E.S.S”. in: *JCAP* 11 (2018), p. 037. doi:
1278 [10.1088/1475-7516/2018/11/037](https://doi.org/10.1088/1475-7516/2018/11/037). arXiv: [1810.00995 \[astro-ph.HE\]](https://arxiv.org/abs/1810.00995).
- 1279 [35] J. Aleksić et al. “Optimized dark matter searches in deep observations of Segue 1 with
1280 MAGIC”. in: *JCAP* 1402 (2014), p. 008. doi: [10.1088/1475-7516/2014/02/008](https://doi.org/10.1088/1475-7516/2014/02/008).
1281 arXiv: [1312.1535 \[hep-ph\]](https://arxiv.org/abs/1312.1535).
- 1282 [36] V.A. Acciari et al. “Combined searches for dark matter in dwarf spheroidal galaxies observed
1283 with the MAGIC telescopes, including new data from Coma Berenices and Draco”. In: *Physics of the Dark Universe* (2021), p. 100912. issn: 2212-6864. doi: <https://doi.org/10.1016/j.dark.2021.100912>. URL: <https://www.sciencedirect.com/science/article/pii/S2212686421001370>.
- 1287 [37] M. L. Ahnen et al. “Indirect dark matter searches in the dwarf satellite galaxy Ursa Major II
1288 with the MAGIC Telescopes”. In: *JCAP* 1803.03 (2018), p. 009. doi: [10.1088/1475-7516/2018/03/009](https://doi.org/10.1088/1475-7516/2018/03/009). arXiv: [1712.03095 \[astro-ph.HE\]](https://arxiv.org/abs/1712.03095).
- 1290 [38] S. et al. Archambault. “Dark matter constraints from a joint analysis of dwarf Spheroidal
1291 galaxy observations with VERITAS”. in: *prd* 95.8 (Apr. 2017). doi: [10.1103/PhysRevD.95.082001](https://doi.org/10.1103/PhysRevD.95.082001). arXiv: [1703.04937 \[astro-ph.HE\]](https://arxiv.org/abs/1703.04937).
- 1293 [39] Louise Oakes et al. “Combined Dark Matter searches towards dwarf spheroidal galaxies with
1294 Fermi-LAT, HAWC, HESS, MAGIC and VERITAS”. in: *Proceedings of Science*. 2019.
- 1295 [40] Celine Armand et al. on behalf of the Fermi-LAT, HAWC, HESS, MAGIC, VERITAS.
1296 “Combined Dark Matter searches towards dwarf spheroidal galaxies with Fermi-LAT,
1297 HAWC, HESS, MAGIC and VERITAS”. in: *Proceedings of Science*. 2021.
- 1298 [41] Daniel Kerszberg et al. on behalf of the Fermi-LAT, HAWC, HESS, MAGIC, and VER-
1299 TIAS collaborations. “Search for dark matter annihilation with a combined analysis of
1300 dwarf spheroidal galaxies from Fermi-LAT, HAWC, H.E.S.S., MAGIC and VERITAS”. in:
1301 *Proceedings of Science*. 2023.
- 1302 [42] A. U. Abeysekara et al. “Observation of the Crab Nebula with the HAWC Gamma-Ray
1303 Observatory”. In: *The Astrophysical Journal* 843.1 (June 2017), p. 39. doi: [10.3847/1538-4357/aa7555](https://doi.org/10.3847/1538-4357/aa7555). URL: <https://doi.org/10.3847/1538-4357/aa7555>.
- 1305 [43] Giacomo Vianello et al. *The Multi-Mission Maximum Likelihood framework (3ML)*. 2015.
1306 arXiv: [1507.08343 \[astro-ph.HE\]](https://arxiv.org/abs/1507.08343).
- 1307 [44] Marco Cirelli et al. “PPPC 4 DM ID: a poor particle physicist cookbook for dark matter
1308 indirect detection”. In: *Journal of Cosmology and Astroparticle Physics* 2011.03 (Mar.
1309 2011). issn: 1475-7516. doi: [10.1088/1475-7516/2011/03/051](https://doi.org/10.1088/1475-7516/2011/03/051). URL: <http://dx.doi.org/10.1088/1475-7516/2011/03/051>.

- 1311 [45] Alex Geringer-Sameth, Savvas M. Koushiappas, and Matthew Walker. “DWARF GALAXY
1312 ANNIHILATION AND DECAY EMISSION PROFILES FOR DARK MATTER EXPERI-
1313 MENTS”. in: *The Astrophysical Journal* 801.2 (Mar. 2015), p. 74. ISSN: 1538-4357. doi:
1314 [10.1088/0004-637X/801/2/74](https://doi.org/10.1088/0004-637X/801/2/74). URL: <http://dx.doi.org/10.1088/0004-637X/801/2/74>.
- 1316 [46] A. Albert et al. “Dark Matter Limits from Dwarf Spheroidal Galaxies with the HAWC
1317 Gamma-Ray Observatory”. In: *The Astrophysical Journal* 853.2 (Feb. 2018), p. 154. ISSN:
1318 1538-4357. doi: [10.3847/1538-4357/aaa6d8](https://doi.org/10.3847/1538-4357/aaa6d8). URL: <http://dx.doi.org/10.3847/1538-4357/aaa6d8>.
- 1320 [47] V. Bonnivard et al. “Spherical Jeans analysis for dark matter indirect detection in dwarf
1321 spheroidal galaxies - Impact of physical parameters and triaxiality”. In: *Mon. Not. Roy.
1322 Astron. Soc.* 446 (2015), pp. 3002–3021. doi: [10.1093/mnras/stu2296](https://doi.org/10.1093/mnras/stu2296). arXiv:
1323 [1407.7822 \[astro-ph.HE\]](https://arxiv.org/abs/1407.7822).
- 1324 [48] M. Ackermann et al. “Searching for Dark Matter Annihilation from Milky Way Dwarf
1325 Spheroidal Galaxies with Six Years of Fermi Large Area Telescope Data”. In: *prl* 115.23,
1326 231301 (Dec. 2015), p. 231301. doi: [10.1103/PhysRevLett.115.231301](https://doi.org/10.1103/PhysRevLett.115.231301). arXiv:
1327 [1503.02641 \[astro-ph.HE\]](https://arxiv.org/abs/1503.02641).
- 1328 [49] M. L. Ahnen et al. “Limits to Dark Matter Annihilation Cross-Section from a Combined
1329 Analysis of MAGIC and Fermi-LAT Observations of Dwarf Satellite Galaxies”. In: *JCAP*
1330 1602.02 (2016), p. 039. doi: [10.1088/1475-7516/2016/02/039](https://doi.org/10.1088/1475-7516/2016/02/039). arXiv: [1601.06590](https://arxiv.org/abs/1601.06590)
1331 [astro-ph.HE].
- 1332 [50] Javier Rico et al. *gLike: numerical maximization of heterogeneous joint
1333 likelihood functions of a common free parameter plus nuisance parameters*.
1334 <https://doi.org/10.5281/zenodo.4601451>. Version v0.09.03. Mar. 2021. doi: [10.5281/zenodo.4601451](https://doi.org/10.5281/zenodo.4601451). URL: <https://doi.org/10.5281/zenodo.4601451>.
- 1336 [51] Tjark Miener and Daniel Nieto. *LklCom: Combining likelihoods from different experiments*.
1337 <https://doi.org/10.5281/zenodo.4597500>. Version v0.5.3. Mar. 2021. doi: [10.5281/zenodo.4597500](https://doi.org/10.5281/zenodo.4597500). URL: <https://doi.org/10.5281/zenodo.4597500>.
- 1339 [52] T. Miener et al. “Open-source Analysis Tools for Multi-instrument Dark Matter Searches”.
1340 In: *arXiv e-prints*, arXiv:2112.01818 (Dec. 2021), arXiv:2112.01818. arXiv: [2112.01818](https://arxiv.org/abs/2112.01818)
1341 [astro-ph.IM].
- 1342 [53] Alex Geringer-Sameth and Matthew Koushiappas Savvas M. and Walker. “Dwarf galaxy
1343 annihilation and decay emission profiles for dark matter experiments”. In: *Astrophys.
1344 J.* 801.2 (2015), p. 74. doi: [10.1088/0004-637X/801/2/74](https://doi.org/10.1088/0004-637X/801/2/74). arXiv: [1408.0002](https://arxiv.org/abs/1408.0002)
1345 [astro-ph.CO].
- 1346 [54] Gianfranco Bertone, Dan Hooper, and Joseph Silk. “Particle dark matter: evidence, can-

- 1347 didates and constraints”. In: *Physics Reports* 405.5-6 (Jan. 2005), pp. 279–390. ISSN:
1348 0370-1573. doi: [10.1016/j.physrep.2004.08.031](https://doi.org/10.1016/j.physrep.2004.08.031). URL: <http://dx.doi.org/10.1016/j.physrep.2004.08.031>.
- 1350 [55] V. Bonnivard et al. “Dark matter annihilation and decay in dwarf spheroidal galaxies: The
1351 classical and ultrafaint dSphs”. In: *Mon. Not. Roy. Astron. Soc.* 453.1 (2015), pp. 849–867.
1352 doi: [10.1093/mnras/stv1601](https://doi.org/10.1093/mnras/stv1601). arXiv: [1504.02048 \[astro-ph.HE\]](https://arxiv.org/abs/1504.02048).
- 1353 [56] A. et al. Albert. “Searching for Dark Matter Annihilation in Recently Discovered Milky Way
1354 Satellites with Fermi-LAT”. in: *Astrophys. J.* 834.2 (2017), p. 110. doi: [10.3847/1538-4357/834/2/110](https://doi.org/10.3847/1538-4357/834/2/110). arXiv: [1611.03184 \[astro-ph.HE\]](https://arxiv.org/abs/1611.03184).
- 1356 [57] Mattia Di Mauro and Martin Wolfgang Winkler. “Multimessenger constraints on the dark
1357 matter interpretation of the Fermi-LAT Galactic Center excess”. In: *prd* 103.12, 123005
1358 (June 2021), p. 123005. doi: [10.1103/PhysRevD.103.123005](https://doi.org/10.1103/PhysRevD.103.123005). arXiv: [2101.11027 \[astro-ph.HE\]](https://arxiv.org/abs/2101.11027).
- 1360 [58] HongSheng Zhao. “Analytical models for galactic nuclei”. In: *Mon. Not. Roy. Astron. Soc.*
1361 278 (1996), pp. 488–496. doi: [10.1093/mnras/278.2.488](https://doi.org/10.1093/mnras/278.2.488). arXiv: [astro-ph/9509122 \[astro-ph\]](https://arxiv.org/abs/astro-ph/9509122).
- 1363 [59] H. C. Plummer. “On the Problem of Distribution in Globular Star Clusters: (Plate 8.)”
1364 In: *Monthly Notices of the Royal Astronomical Society* 71.5 (Mar. 1911), pp. 460–470.
1365 ISSN: 0035-8711. doi: [10.1093/mnras/71.5.460](https://doi.org/10.1093/mnras/71.5.460). eprint: <https://academic.oup.com/mnras/article-pdf/71/5/460/2937497/mnras71-0460.pdf>. URL:
1367 <https://doi.org/10.1093/mnras/71.5.460>.
- 1368 [60] Daniel R. Hunter. “Derivation of the anisotropy profile, constraints on the local velocity
1369 dispersion, and implications for direct detection”. In: *JCAP* 02 (2014), p. 023. doi:
1370 [10.1088/1475-7516/2014/02/023](https://doi.org/10.1088/1475-7516/2014/02/023). arXiv: [1311.0256 \[astro-ph.CO\]](https://arxiv.org/abs/1311.0256).
- 1371 [61] Barun Kumar Dhar and Liliya L. R. Williams. “Surface mass density of the Einasto family
1372 of dark matter haloes: are they Sersic-like?” In: *Mon. Not. Roy. Astron. Soc.* (2010). doi:
1373 [10.1111/j.1365-2966.2010.16446.x](https://doi.org/10.1111/j.1365-2966.2010.16446.x).
- 1374 [62] M. Baes and E. Van Hese. “Dynamical models with a general anisotropy profile”. In:
1375 *Astron. Astrophys.* 471 (2007), p. 419. doi: [10.1051/0004-6361:20077672](https://doi.org/10.1051/0004-6361:20077672). arXiv:
1376 [0705.4109 \[astro-ph\]](https://arxiv.org/abs/0705.4109).
- 1377 [63] Matthew G. Walker, Edward W. Olszewski, and Mario Mateo. “Bayesian analysis of re-
1378 solved stellar spectra: application to MMT/Hectochelle observations of the Draco dwarf
1379 spheroidal”. In: *mnras* 448.3 (Apr. 2015), pp. 2717–2732. doi: [10.1093/mnras/stv099](https://doi.org/10.1093/mnras/stv099).
1380 arXiv: [1503.02589 \[astro-ph.GA\]](https://arxiv.org/abs/1503.02589).
- 1381 [64] Nicholas L. Rodd et al. “Dark matter spectra from the electroweak to the Planck scale”. In:

- 1382 *J. High Energy Physics* 121.10.1007 (June 2021).
- 1383 [65] Pace, Andrew B and Strigari, Louis E. “Scaling relations for dark matter annihilation and
1384 decay profiles in dwarf spheroidal galaxies”. In: *Monthly Notices of the Royal Astronomical
1385 Society* 482.3 (Oct. 2018), pp. 3480–3496. ISSN: 0035-8711. doi: [10.1093/mnras/sty2839](https://doi.org/10.1093/mnras/sty2839).
- 1387 [66] Albert, A. et al. “Search for gamma-ray spectral lines from dark matter annihilation in
1388 dwarf galaxies with the High-Altitude Water Cherenkov observatory”. In: *Phys. Rev. D* 101 (10 May 2020), p. 103001. doi: [10.1103/PhysRevD.101.103001](https://doi.org/10.1103/PhysRevD.101.103001). URL:
1389 <https://link.aps.org/doi/10.1103/PhysRevD.101.103001>.
1390